Title	Design of Metal Nanoparticle Catalysts for Highly Efficient Hydrogenation and Dehydrogenation Reactions
Author(s)	浦山, 鉄平
Citation	大阪大学, 2017, 博士論文
Version Type	VoR
URL	https://doi.org/10.18910/61830
rights	
Note	

Design of Metal Nanoparticle Catalysts

for Highly Efficient Hydrogenation and Dehydrogenation Reactions

Teppei Urayama

March 2017

Design of Metal Nanoparticle Catalysts

for Highly Efficient Hydrogenation and Dehydrogenation Reactions

A dissertation submitted to

THE GRADUATE SCHOOL OF ENGINEERING SCIENCE

OSAKA UNIVERSITY

in partial fulfillment of the requirements for the degree of

DOCTOR OF PHILOSOPHY IN ENGINEERING

BY

Teppei Urayama

March 2017

Abstract

This thesis deals with the studies on the design of metal nanoparticle catalysts for highly efficient hydrogenation and dehydrogenation. The present thesis consists of six chapters.

In chapter I, the author reviews the current state of the art in design of metal nanoparticle catalysts for the selective molecular transformations under liquid-phase conditions. Methodologies for the design of metal nanoparticles are categorizes into four types, that is, 1) electronic interaction with their support materials, 2) concerted effect with their support materials, 3) control of their morphology, 4) addition of other metals to form bimetal catalysts and the related works are highlighted.

Chapter II describes the novel design concept and precise fabrication of Pd-core/Ag-shell nanocomposite catalyst for selective semihydrogenation of alkynes to alkenes under ambient conditions. The unique catalysis of the core-shell catalyst derives from the cooperative action between core-Pd and shell-Ag. The inner Pd nanoparticles can act as the hydrogen supplier to the outer Ag layer, assisting the selective semihydrogenation of alkynes on the Ag surface.

The author demonstrates in Chapter III the first success of a green one-step synthesis of small core-shell nanoparticles under organic-free and pH-neutral condition. This newly developed method provides CeO_2-covered Au and Ag nanoparticles through the simple and clean procedure. Moreover, the synthesized CeO_2-covered Au catalyst promoted chemoselective hydrogenation of unsaturated aldehydes, epoxides and alkynes while retaining C=C bonds.

Chapter IV represents unique catalysis of hydroxyapatite-supported Au nanoparticles for dehydrogenative coupling of hydrosilanes and amines or amides. A wide range of silylamines and silylamides can be obtained in good to excellent yields, demonstrating the first example of an efficient heterogeneous catalyst for the synthesis of silylamides. Furthermore, Au/HAP shows the

highest activity for this coupling reaction among the reported catalysts.

Chapters V and VI are described the development of the Au/HAP-O_2 catalytic system for the highly efficient dehydrogenative coupling of hydrosilanes with water. Various silanes including less reactive bulky hydrosilanes could be converted to the corresponding silanols with low catalyst loading. In the Au/HAP-O_2 catalytic system, O_2 acts as a highly effective gas-ligand for Au nanoparticles, achieving excellent turnover number and turnover frequency, both of which are much greater than those of previously reported catalysts. The author attains further improvement of catalytic activity for this reaction by the synthesis of uniformly small size of Au nanoparticles. The resulting highly active catalytic system is applicable to an environmental-friendly H_2-production from the aqueous oxidation of inexpensive hydroilanes as hydrogen storage materials.

Preface

This dissertation is a collection of the author's studies which were carried out from 2012 to 2017 under the supervision of Professor Koichiro Jitsukawa and Specially-appointed Professor Kiyotomi Kaneda at the Division of Chemical Engineering Department of Materials Engineering Science, Graduate School of Engineering Science, Osaka University.

In this thesis, the rational synthesis of metal nanoparticle catalysts enables the efficient hydrogenation and dehydrogenation reactions. The precisely morphology-controlled metal nanoparticles play a key role to exhibit unprecedentedly unique catalysis in these reactions.

Development of highly efficient heterogeneous catalytic systems is of great importance in the modern society, which can reduce environmental impacts of chemical industry. Even today, many organic reactions are still carried out using stoichiometric reagents and it is highly required to replace the conventional hazardous processes with environmental-friendly ones. Therefore, the author aimed for the design and the precise synthesis of high-performance metal nanoparticle catalysts for efficient and environmental-friendly fine chemical synthesis.

The author hopes that the present study on metal nanoparticle catalysts for fine chemical synthesis contributes to the development of clean and novel catalytic process on the basis of Green Sustainable Chemistry.

Contents

Chapter I.

General Introduction

1. Preliminary

Chemistry plays a key role to maintain and improve our quality of life in almost all aspects of modern society. It offers us a variety of benefits and provides us necessaries and conveniences such as synthetic fibers, medicines, electronics and many other products, while it could be cause of environmental problems. In fact, several tonnes of hazardous waste have been released to the air, water and land by chemical industry every day [1]. The pollution of soil, water and atmosphere can be caused by them and these environmental problems possess the risk for human health hazards.

In order to prevent and solve the above mentioned environmental problems, environmental conservation had become more important factors in the various industrial fields in the early 1960s. Furthermore, to clarify the guidance for the construction of environmental-friendly chemical industry, Anastas and Williamson articulated the twelve principles of Green Chemistry in 1998 [2]. In these principles, the following sentences are denoted: "Catalytic reagents (as selective as possible) are superior to stoichiometric reagents.", "Synthetic methods should be designed to maximize the incorporation of all materials used in the process into the final products." and "Energy requirements should be recognized for their environmental and economic impacts and should be minimized. Synthetic method should be conducted at ambient temperature and pressure." In other words, the development of environmental-friendly catalytic systems which promote selective transformation efficiently under mild reaction conditions is highly required in the modern chemical industry.

For the purpose of the construction of chemical processes adapted to the concept of Green Chemistry, various heterogeneous and homogeneous catalytic systems have been developed. Generally, homogeneous catalysts show high chemo-, region- and enantioselectivity as compared to conventional heterogeneous catalysts. Furthermore, their catalysis is easily optimized by the modification of ligands and metal centers. However, due to the difficulty in catalyst separation from the resulting mixture, complicated preparation methods and low cost-efficiency, many homogeneous

catalysts have not been commercialized [3]. In fact, heterogeneous catalysts are used in the 90% of all chemical processes [4], mainly for bulk chemical synthesis. For the industrial uses, heterogeneous catalysts have many advantages such as easy handling, high reusability and thermal stability, and applicability to the flow reactors.

To apply heterogeneous catalysts to the fine chemical synthesis which require high chemo-, region- and enantioselectivity, supported metal nanoparticle catalysts offer great potential. In addition to the advantages of conventional heterogeneous catalysts, metal nanoparticle catalysts could show tailor-made catalysis through the modification of their chemical and physical properties such as diameters, shapes, composition, morphology and selection of suitable supports. Therefore, precise syntheses and novel design of metal nanoparticle catalysts are critical theme and make a great contribution to build up green chemical industry and sustainable society.

2. Background

2-1. Metal Nanoparticle Catalysts for Effective Syntheses of Fine Chemicals

In the field of organic transformations, metal nanoparticles have appeared since the early 19th century [5]. They were adventitiously generated in ostensibly homogeneous catalytic reactions and overlooked due to the lack of analytical techniques although they were actually active species. Along with the advance of heterogeneity test techniques [6-7], it was clear that the truly active species were metal nanoparticles in the various organic transformations such as hydrosilylation [7], C-C coupling [8] and hydrogenation [9]. Since these facts were disclosed, metal nanoparticles attracted enormous attention as the promising catalytic materials. However, these conventional metal nanoparticles prepared without the rational designs suffer from structural polydispersity, causing low activity and selectivity for the desired products.

Recent advance of nanotechnology and characterization techniques allow for more precise and rational synthesis of metal nanoparticles [10] and have expanded catalytic possibilities of them. Optimization of catalytic properties through modification of their size, shape, chemical composition, electronic state and interaction with support materials realized tailor-made catalysis for the selective synthesis of various fine chemicals. From the standpoint of Green Chemistry, high selective catalysts have great advantages such as usage of lower amount of raw materials, avoidance of subsequent separation steps and minimizing of the potentially polluting byproducts. In the following, the studies on metal nanoparticle catalysts for efficient fine chemical syntheses are reviewed. Modification strategies for supported metal nanoparticle catalysts are categorized into the following 4 types: 1) electronic interaction with their support materials, 2) concerted effect with their support materials, 3) control of their morphology, 4) addition of other metals to form bimetal catalysts.

2-2. Electronic Interaction between Metal Nanoparticles and Support Materials

Conventionally, catalytic supports had been regarded as inert materials and the role of

them had been thought only to stabilize and disperse active metal nanoparticles. Now that the

sophisticated characterization methods to detect charge transfer between nanoparticles and supports

were developed, support materials attract great attention as electron modulators [11-14]. Chemical

bonding and the associated charge transfer at the interface between metal nanoparticles and their

supports play a key role to optimize the electronic and chemical properties of metal active species

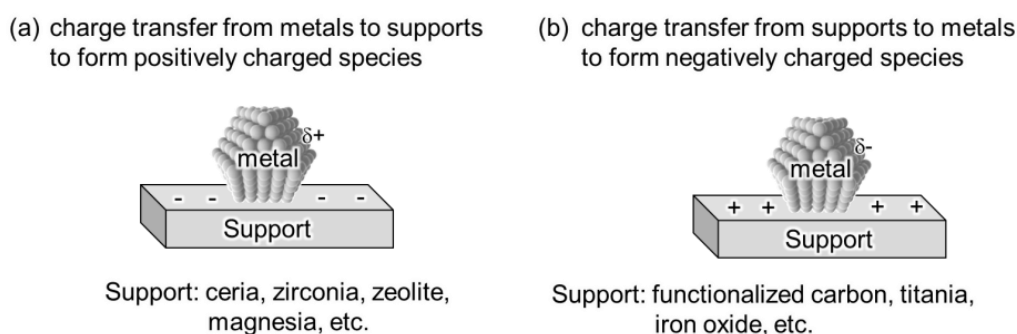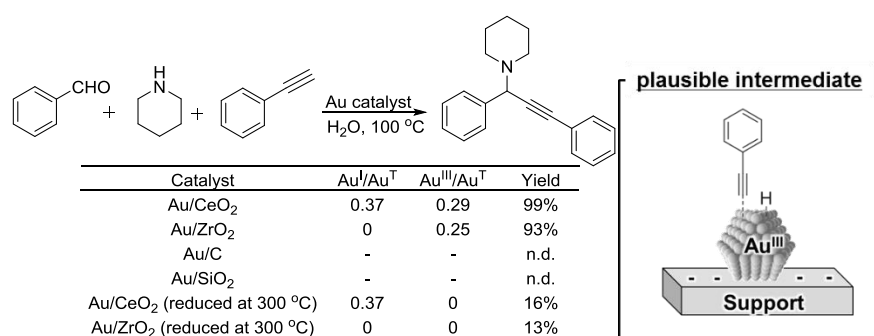for fine chemical synthesis (Figure 1-1).

Figure 1-1. Electronic interaction between metal nanoparticles

Corma *et al*. developed zirconium oxide- or cerium oxide-supported cationic Au

nanoparticle catalysts (Au/ZrO$_2$ or Au/CeO$_2$) for various organic transformations [15-20]. In the

developed catalysts, Au-O (lattice oxygen of metal oxides) bonds were formed and the charge

transfer from Au nanoparticles to lattice oxygen atoms occurred at the interface of them. This charge

transfer from Au nanoparticles to lattice oxygen atoms provided positively charged Au active species

(as depicted in Figure 1-1, a) [21]. The presence of positively charged Au species was confirmed by

using X-ray Photoelectron Spectroscopy (XPS) of Au 4f$_{7/2}$ and Fourier Transformation Infrared

Spectroscopy (FT-IR) study using CO as probe molecules [16, 17], which revealed that three-type

Au species, that is, Au^I, Au^{III} and Au^0 existed in the developed catalysts. Interestingly, Au/ZrO$_2$ and

Au/CeO$_2$ showed high activity for three-component coupling of aldehydes, amines and alkynes to

form propargylamines as is the case for homogeneous cationic Au^{III} complexes, whereas zero-valent

Au species formed in Au/C and Au/SiO$_2$ did not show any activity (Scheme 1-1). To clarify the

active Au species, they investigated the correlation between the ratio of Au^I and Au^{III} (Au^X/Au^T, Au^T: total amount of Au) and activity by changing Au^X/Au^T through reduction of the catalysts with H_2 (Scheme 1-1). These results showed the direct correlation between Au^{III}/Au^T and catalytic activity and no correlation for the concentration of Au^I or Au^0, indicating that main active species for the coupling reactions are Au^{III} existed on Au nanoparticle surface. It is considered that this coupling reaction proceeded *via* the formation of Au-acetylide intermediates. They mentioned that only Au^{III} could efficiently form the Au-acetylide intermediate and Au^0 and Au^I could hardly activate alkynes to form the intermediates.

Catalyst	Au^I/Au^T	Au^{III}/Au^T	Yield
Au/CeO$_2$	0.37	0.29	99%
Au/ZrO$_2$	0	0.25	93%
Au/C	-	-	n.d.
Au/SiO$_2$	-	-	n.d.
Au/CeO$_2$ (reduced at 300 ºC)	0.37	0	16%
Au/ZrO$_2$ (reduced at 300 ºC)	0	0	13%

Scheme 1-1. Three-component coupling catalyzed by Au catalysts

Somorjai *et al*. regarded metal oxide supports as electronic modulators and demonstrated that metal oxides could change the electronic and catalytic properties of metal nanoparticle catalysts [22-24]. They reported that $CeO_2/Pt/SiO_2$ bifunctional catalysts for ethylene hydroformylation to propanal using methanol and ethylene as reactants. In this reaction, initially, decomposition of methanol to CO and H_2 proceeded at the interface between Pt and CeO_2. Subsequently, hydroformylation reaction from the resulting CO, H_2 and ethylene to propanal occurred at Pt-SiO$_2$ interface of $CeO_2/Pt/SiO_2$ (Scheme 1-2, a), whereas unmodified Pt/SiO$_2$ did not promote hydroformylation of ethylene but hydrogenated CO to methanol (Scheme 1-2, b). These sharply
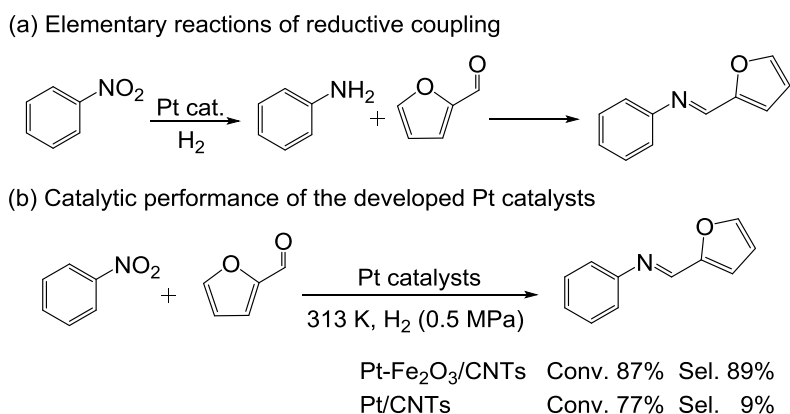
contrasting results of $CeO_2/Pt/SiO_2$ with Pt/SiO_2 were owing to the difference in the electron states of Pt nanoparticles. Modification of Pt/SiO_2 with CeO_2 generated positively charged Pt nanoparticles through Pt-O-Ce bond formation and related charge transfer from Pt to lattice oxygen atoms (as depicted in Figure 1-1, a). This positively charged Pt atoms inhibit both strong CO adsorption on Pt surface and hydrogenation of CO to methanol. In other words, the addition of CeO_2 to Pt/SiO_2 promoted neither over-activation nor hydrogenation of CO on Pt surface, thus achieving selective hydroformylation to aldehydes.
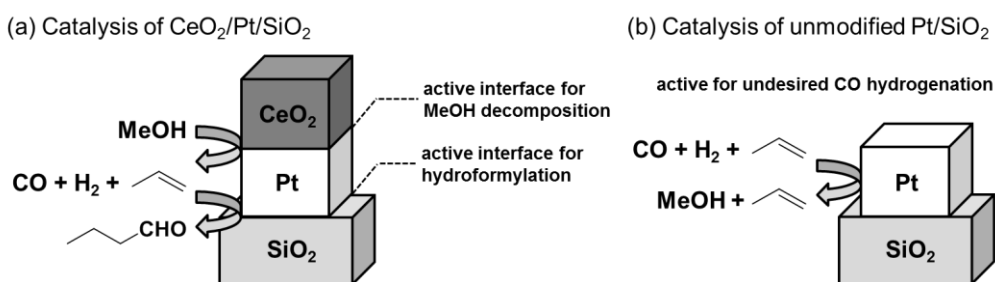
Scheme 1-2. Pt-catalyzed tandem reaction for aldehyde synthesis

In order to maximize the beneficial electronic interaction between active species and metal oxides, Qin *et al*. designed core-Fe_2O_3/shell-Pt nanoparticle catalyst for selective reductive coupling of nitro compounds and furfural to imine derivatives [25]. This reductive coupling is two step reaction; hydrogenation of nitro group to amine and sequential coupling of the resulting amines and aldehyde group of furfural to yield the corresponding imine (Scheme 1-3, a). In this catalytic system, highly selective synthesis with suppression of overhydrogenation of the desired imines was attained through efficient creation of interface sites between Pt and Fe^{3+}-OH. XPS study revealed that Fe^{3+}-OH species showed high electron-donating properties and induced charge transfer from Fe oxides to Pt nanoparticles (as depicted in Figure 1-1, b), yielding negatively charged Pt surfaces. It is reported that negatively charged Pt surface favors the adsorption of the electron-deficient functional

group than that of electron-rich group [26]. Analogously, during the this coupling reaction, negatively charged Pt surface selectively adsorbed the electron-deficient functional group (nitro group) and preferentially hydrogenated them, whereas this Pt sites disfavored the adsorption of electron-rich group (imine group) and suppressed undesired hydrogenation of imines to amines (Scheme 1-3, b). Namely, electron donating properties of Fe^{3+}-OH species improved activity and selectivity of Pt nanoparticles through the modification of adsorption behavior of Pt surface.

(a) Elementary reactions of reductive coupling

(b) Catalytic performance of the developed Pt catalysts

|		
Pt-Fe$_2$O$_3$/CNTs	Conv. 87%	Sel. 89%
Pt/CNTs	Conv. 77%	Sel. 9%

Scheme 1-3. Reductive coupling of nitrobenzene and furfural to imine

In addition to inorganic materials such as metal oxides, heteroatom-doped carbon supports are effective as electron modulators for metal nanoparticle catalysts [27-30]. Su *et al.* synthesized small Pt nanoparticles supported on pristine, oxygen functionalized, and nitrogen-doped carbon nanotubes which were denoted by Pt/CNTs, Pt/oCNTs and Pt/NCNTs respectively, and investigated their catalytic activity for nitroarene-hydrogenation and electronic interaction between Pt and heteroatoms [27]. In these catalysts, Pt nanoparticles were anchored to CNT surface through the formation of Pt-heteroatom bonds. This bond-formation induced the charge transfer from heteroatoms to Pt nanoparticles (as depicted in Figure 1-1-b), generating negatively charged Pt species. As aforementioned in Qin's work, negatively charged Pt nanoparticles showed high activity

for hydrogenation of electron-deficient nitro groups. Consequently, Pt/NCNTs showed superior activity than those of Pt/CNTs and Pt/oCNTs due to the strong electron-donating properties of nitrogen atoms (Scheme 1-4). Furthermore, Pt/NCNTs exhibited high chemoselectivity toward nitro groups in the hydrogenation of various halonitroarenes to haloanilines without dehalgenation (Scheme 1-5). The electron-rich Pt nanoparticles selectively adsorbed the electron-deficient nitro groups and chemoselectively hydrogenated them whereas electron-rich halogen groups were intact.

Catalyst	Yield
Pt/NCNTs	98%
Pt/oCNTs	76%
Pt/CNTs	37%
commercial Pt/C	28%
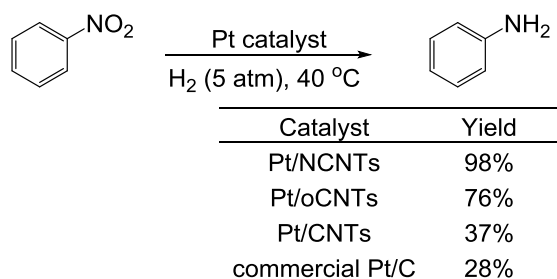
Scheme 1-4. Nitrobenzene hydrogenation over Pt-based catalysts
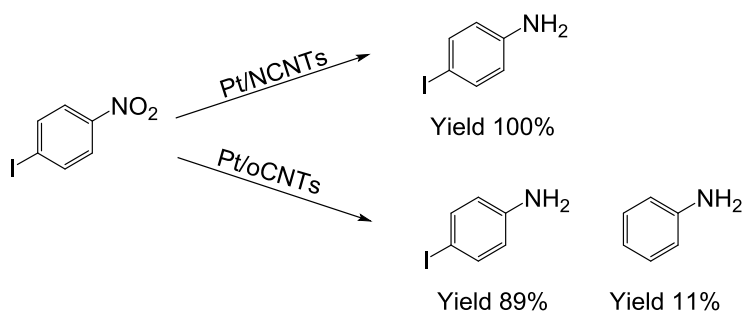
Scheme 1-5. Selective hydrogenation of Halonitrobenzene over Pt-based catalysts

As shown in above mentioned works, the electronic interaction between metal nanoparticles and their supports affect the adsorption properties of metal nanoparticles and their catalysis dramatically.

2-3. Concerted Effect of Metal Nanoparticles and Catalytic Supports

Toward design more efficient catalytic systems, support materials are expected to act not only as stabilizers for metal nanoparticles but also as co-catalysts in the catalytic cycles. Namely, metal nanoparticles and its supports individually activate different substrates (Figure 1-2, a) or they cooperatively activate one substrate at their interface (Figure 1-2, b). These concerted actions of metal nanoparticles with supports would realize the unique catalysis, effectively promoting chemical transformations under mild conditions. Thus, suitable choice of functional materials such as metal oxides, metal-organic frameworks and zeolites for catalytic supports can expand the catalytic potential of metal nanoparticles for various fine chemical syntheses.
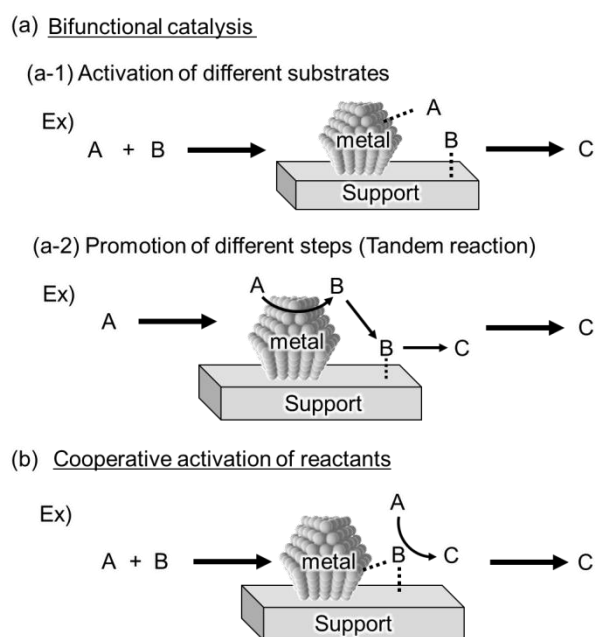

Figure 1-2. Concerted Effect of Metal Nanoparticles and Supports

Reducible oxides such as titania, ceria and zirconia are widely used as catalytic supports due to their thermal stability and redox properties [31-34]. Especially, in the hydrogenation reaction for electron-rich functional groups, *in-situ* generated oxygen vacancy sites act as the effective Lewis acid catalysts and realize selective hydrogenation under mild conditions [35-40]. Hardacre *et al.* reported the selective hydrogenation of various carboxylic acids to the corresponding alcohols using

titania-supported Pt catalysts (Scheme 1-6) [35]. During the reaction, oxygen vacancy of titania was created by the reduction with hydrogen spillover from Pt nanoparticles. The resulting oxygen vacancy showed Lewis acidity and activated carbonyl oxygen of carboxylic acids. This interaction weakened C=O bonds of carboxylic acids and assisted Pt-promoted hydrogenation and cleavage of carbon-oxygen bonds. Thus, the cooperative actions of C=O bond activation by oxygen vacancy of titania and H_2 activation by Pt nanoparticles realized efficient hydrogenation of carboxylic acids under relative mild conditions.
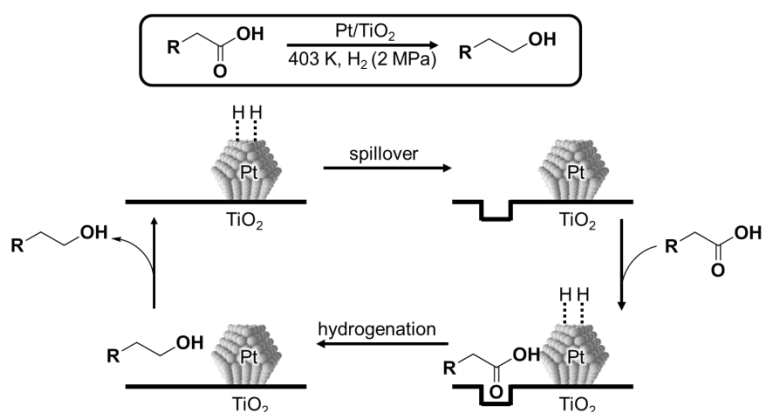

Scheme 1-6. Hydrogenation of carboxylic acid using Pt/TiO$_2$

Kaneda *et al*. demonstrated a series of the concerted catalysis of Au and Ag nanoparticles with solid base materials [41-46]. Hydrotalcite (HT, $Mg_6Al_2(OH)_{16}CO_3 \cdot nH_2O$)-supported Au and Ag nanoparticle catalysts exhibited highly selective catalysis for alcohol oxidation [41-43] and chemoselective hydrogenation of various functional groups [44-46]. The reason for high activity of the developed Au and Ag catalysts for alcohol oxidation is explained by the cooperative activation of alcohols at the interface between metal nanoparticles and HT (Scheme 1-7). Initially, abstraction of proton from alcohols occurred at the basic sites of HT and the resulting metal-alcoholate species underwent β-hydride elimination to effectively yield the corresponding carbonyl products. Furthermore, they revealed that the cooperative work between Au nanoparticles and the basic sites of

HT could be applied to the activation of H_2, realizing highly chemoselective hydrogenation reactions. Namely, H_2 molecule was activated at the interface between Au nanoparticle and basic site of HT, resulting in the formation of polar hydrogen species $H^{\delta+}$ and $H^{\delta-}$ through heterolytic cleavage of H_2 (Scheme 1-8). These generated polar hydrogen species promoted deoxygenation of epoxides to alkenes and hydrogenolysis of allylic carbonates to terminal alkenes without undesired hydrogenation of non-polar C=C bonds. The generation of polar hydrogen species was confirmed by IR studies and control experiments using 2-propanol or CO/H_2O instead of H_2 which are well-known to generate polar hydrogen species.
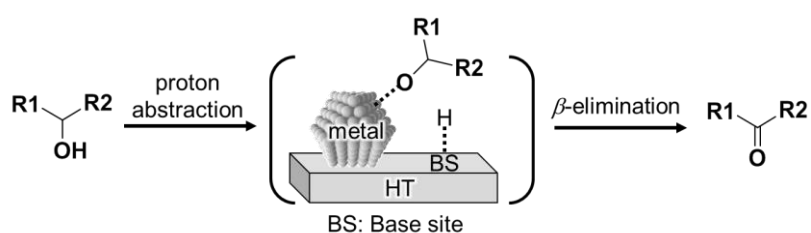

Scheme 1-7. Alcohol oxidation using HT-supported Au or Ag nanoparticles
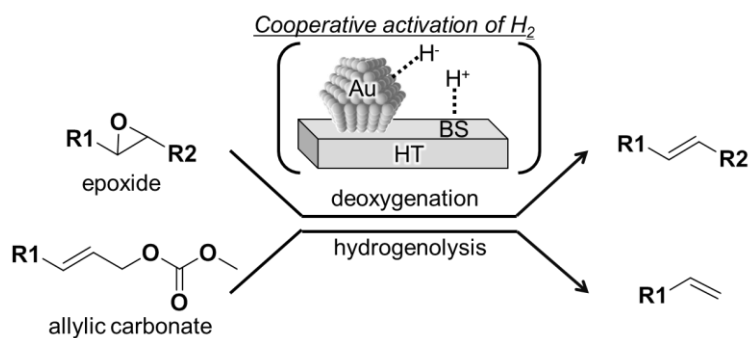
Scheme 1-8. Selective reduction via heterolytic cleavage of H_2 at the interface of Au nanoparticles and HT

To expand chemoselective catalysis of HT-supported metal nanoparticles for hydrogenations, they next tried hydrogenation of 3-nitrostyrene using Ag/HT. However, Ag/HT

caused reductions of both polar nitro group and non-polar C=C bond and they claimed that this non-selective reduction was due to the formation of non-polar hydrogen species through the homolytic cleavage of H_2 on the Ag bare surface (Scheme 1-9, a-(1)). To inhibit the creation of non-polar hydrogen species, they designed CeO_2-covered Ag nanoparticle catalyst, where Ag nanoparticles were covered with CeO_2 (solid base). In this core-shell nanoparticles, the interface area between Ag and CeO_2, which efficiently produces polar hydrogen, was maximized, whereas bare Ag surface area, which caused unselective hydrogenations, was minimized (Scheme-1-9, a-(2)) [47]. The Ag@CeO_2 core-shell catalyst exhibited the perfect chemoselectivity for hydrogenations of unsaturated nitro compounds to the corresponding unsaturated amines (Scheme 1-9, b) and also showed high chemoselectivity for deoxygenation of epoxides to alkenes using H_2. Interestingly, when the reaction time was prolonged after the full conversion of substrates, the resulting products were not over-hydrogenated to saturated compounds. Kaneda *et al*. also synthesized CeO_2-covered Au nanoparticle catalyst (Au@CeO_2) and demonstrated chemoselective semihydrogenation of alkynes to the corresponding alkenes with excellent selectivity (> 99%) (Scheme 1-9, c).
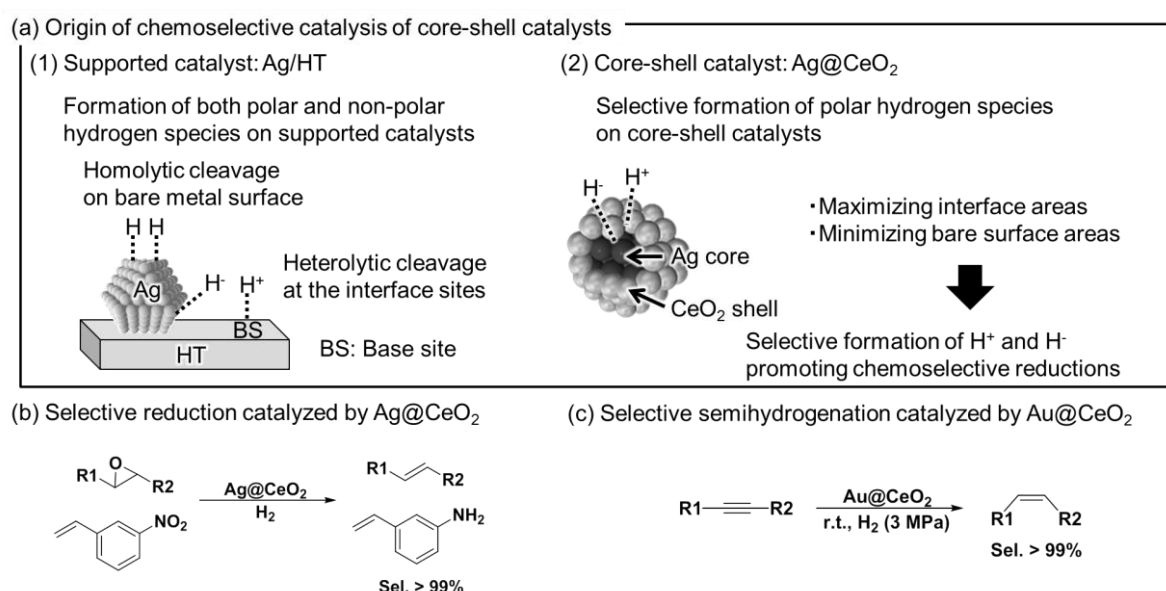
Scheme 1-9. Selective reduction catalyzed by CeO_2-covered core-shell nanoparticles

One-pot reactions offer many practical advantages such as avoidance of isolation procedures of each reaction steps and the related by-production of chemical wastes. Supported nanoparticles could act as multifunctional catalysts for various cascade reactions in a one-pot process [51-57]. Tang *et al*. designed core-shell Pd nanoparticle within metal organic frameworks (MOFs) as multifunctional catalysts for one-pot synthesis of 2-(4-aminobenzylidene)malonitrate [55], known as a key intermediate in the synthesis of dyes and antihypertensive drugs. In the first step of this reaction, Knoevenagel condensation of 4-nitrobenzaldehyde and malonitrate into 2-(4-nitrobenzylidene)malonitrile was promoted by the amino-functionalized isoreticular MOF-3 (IRMOF-3). Sequentially, hydrogenation of nitro groups of the resulting intermediate underwent with Pd nanoparticles, yielding 2-(4-aminobenzylidene)malonitrate (Scheme 1-10, a). In this core-shell catalyst, substrates entered into the pores of IRMOF-3 and then Knoevenagel condensation was completed before unreacted substrates reached the Pd cores, thus inhibiting undesired hydrogenation of aldehyde groups (Scheme 1-10, b). In sharp contrast to the core-shell catalyst, the supported catalyst whose Pd nanoparticles were exposed to catalyst surface promoted hydrogenation of aldehydes to alcohols, causing low selectivity for 2-(4-aminobenzylidene)malonitrate (Scheme 1-10-c).

Scheme 1-10. Selective synthesis of 2-(4-aminobenzylidene)malonitrile (C) using Pd@IRMOF-3 catalyst
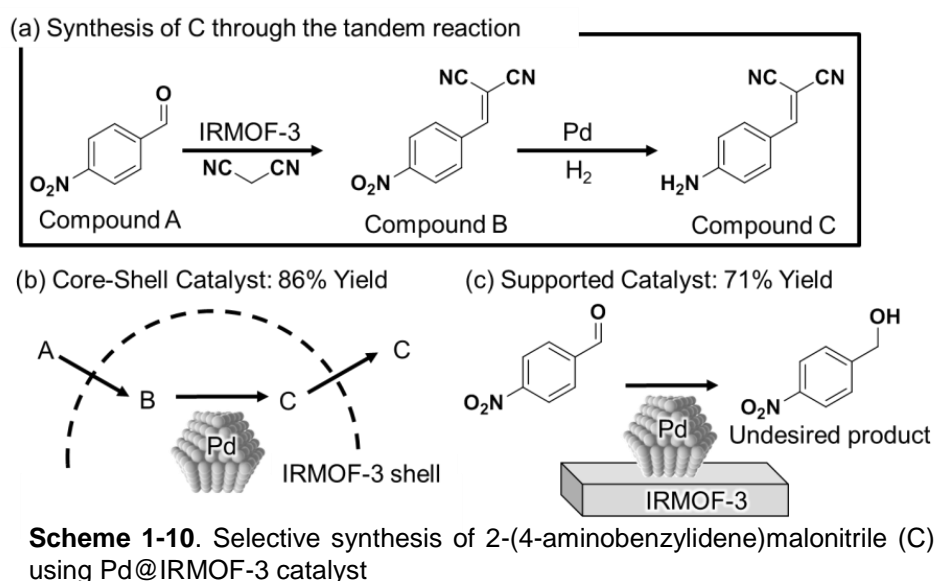
As these reports indicate, the catalytic supports provide metal nanoparticles with bifunctional catalysis for the effective chemical transformations.

2-4. Control of Metal Nanoparticle Morphology

It is well known that smaller nanoparticles exhibit higher activity than that of bigger ones owing to their high surface area and surface roughness [58, 59]. As well as their sizes, shapes and exposed facets of metal nanoparticles have attracted enormous attention as one of the important factors affecting their activity and selectivity for target reactions. Recent progress of characterization techniques and colloidal synthetic approaches using versatile surfactants, reducing agents and metal precursors allows us to synthesize size-controlled nanoparticles with a variety of shapes such as sphere, cube, tetrahedron, octahedron, rod, plate and so on (Figure 1-3) [60-64]. Along with the advances in the synthetic field, morphology-dependent unique catalysts have been developed [65-73]. The fine tunings of their morphology would offer great applicability to fine chemical synthesis.
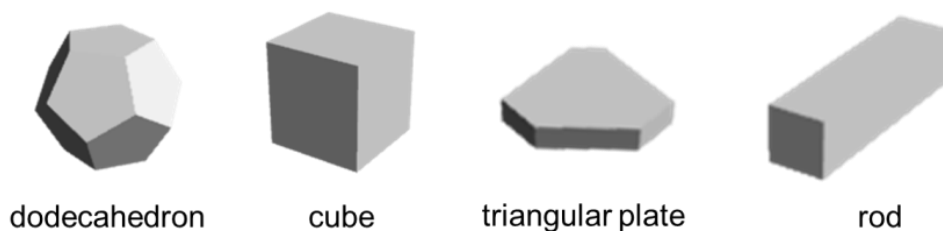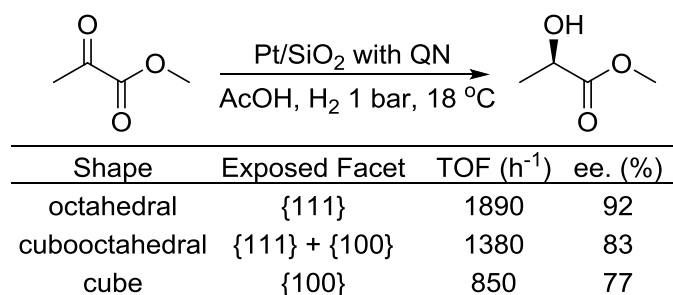

dodecahedron   cube   triangular plate   rod

Figure 1-3. Various shapes of nanoparticles

Baiker *et al*. prepared several shapes of Pt nanoparticles with similar sizes and investigated their catalysis for enantioselective hydrogenation of ethyl pyruvate using quinine (QN) as chiral modifier molecules [67]. Silica-supported cubic, cubooctahedral and octahedral Pt nanoparticles whose exposed facets are {100}, {100} + {111} and {111}, respectively, exhibited shape-dependent activity and enantioselectivity related to their exposed facets (Scheme 1-11). From their results, it was clear that Pt {111} exhibited higher activity and enantioselectivity than that of Pt {100} in
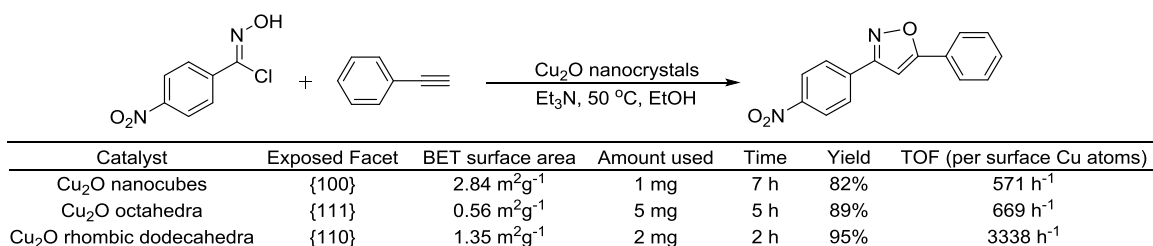
15

hydrogenation of ethyl pyruvate. They claimed that this facet dependency was due to the difference of adsorption energies of QN on the Pt facets. From the DFT study, QN was more strongly adsorbed on Pt {100} than on Pt {111}. This strong adsorption reduced durability of QN against hydrogenation by Pt nanoparticles and UV studies revealed that anchoring moieties of QN, quinolone ring, were hydrogenated rapidly on Pt {100}, while QN was hardly hydrogenated on Pt {111}. In other words, the chiral modifier QN deteriorated more rapidly on Pt {100}, causing low enentioselectivity. Additionally, strong adsorption of QN on Pt surface blocked Pt {100} active sites and also caused low activity for hydrogenation of ethyl pyruvate.

Shape	Exposed Facet	TOF (h^{-1})	ee. (%)
octahedral	{111}	1890	92
cubooctahedral	{111} + {100}	1380	83
cube	{100}	850	77

Scheme 1-11. Enantioselective hydrogenation of ethyl pyruvate

Huang *et al*. investigated facet-dependent catalytic activity of Cu_2O nanocrystals for efficient regioselective synthesis of 3,5-substituted isoxazoles [70]. They prepared Cu_2O nanocubes, octahedral and rhombic dodecahedra which are bound by the {100}, {111} and {110} facets, respectively. The results indicated that Cu_2O rhombic dodecahedara clearly showed higher activity compared with nanocubes and octahedral (Scheme 1-12), demonstrating the selection of suitable facets is important to develop efficient catalysts. This facet-dependency of catalytic activity was due to the degree of exposure of surface Cu atoms. On the {100} and {111} planes, Cu atoms are located below the plane of surface oxygen atoms. On the other hand, the {110} plane is terminated with copper and oxygen atoms lying on the same planes, so that all the surface Cu atoms are fully exposed. In other words, the {110} planes dominantly possess coordinatively unsaturated Cu atoms

on its surface, whereas Cu sites of the {111} and {100} planes are partially blocked by the oxygen

planes. These exposed Cu sites are active for the formation of Cu-acetylide intermediates and the

effectively promote this coupling reaction.

Catalyst	Exposed Facet	BET surface area	Amount used	Time	Yield	TOF (per surface Cu atoms)
Cu_2O nanocubes	{100}	2.84 m^2g^{-1}	1 mg	7 h	82%	571 h^{-1}
Cu_2O octahedra	{111}	0.56 m^2g^{-1}	5 mg	5 h	89%	669 h^{-1}
Cu_2O rhombic dodecahedra	{110}	1.35 m^2g^{-1}	2 mg	2 h	95%	3338 h^{-1}

Scheme 1-12. Comparison of catalytic potential of different Cu2O nanocrystal for the synthesis of 3-(4-nitrophenyl)-5-phenylisoxazoles

As above mentioned reports indicate, metal nanoparticles shows different coordination

states dependently on their exposed facets. Thus, precise control of the exposed facet can realize

catalytic activity and selectivity of metal nanoparticles.

2-5. Addition of Other Metals to Form Bimetal Catalysts

Bimetal nanoparticle catalysts can be divided into two types of heterostructured catalysts

and alloy-structured catalysts (Figure 1-4). In the heterostructured catalysts, different metal species

exist individually (not mixedly), and the interface between two metals are formed (Figure 1-4-a).

This interface sites play a key role to exhibit their unique cooperative catalysis. On the other hand,

the alloy catalysts have two metals, which are mixed homogeneously on the atomic level and

covalently banded together (Figure 1-4-b). Alloying with the second metal is a promising approach

for fine tunings of electronic properties of single nanoparticle through the electronic interaction *via*

the covalent bonds. Furthermore, the second metals can isolate the active metal atoms, generating

geometrically controlled active sites. Based on the above-mentioned advantages, bimetal

nanoparticle catalysts have been developed for various fine chemical syntheses [74-79].
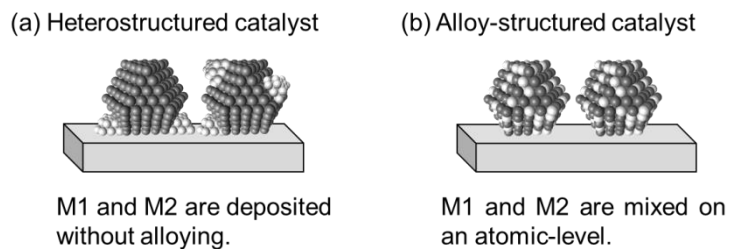
17

(a) Heterostructured catalyst
M1 and M2 are deposited
without alloying.

(b) Alloy-structured catalyst
M1 and M2 are mixed on
an atomic-level.

Figure 1-4. Two types of bimetal catalysts

Tsang *et al*. demonstrated chemoselective hydrogenation of cinnamaldehyde to cinnamyl alcohol using Co-decorated Pt bimetal catalysts prepared by the polyol process [80]. They claimed that Co cluster were deposited on Pt nanoparticle surface without alloying. The Co-decorated Pt catalyst hydrogenated cinnamaldehyde to cinnamyl alcohol selectively, whereas unmodified Pt catalysts hydrogenated C=C bonds of cinnamaldehyde and cinnamyl alcohol, causing low selectivity for cinnamyl alcohol (Scheme 1-13). The origin of high chemoselectivity was due to the geometric and electronic changes of Pt active sites triggered by Co modification. First, they investigated Pt surface geometric conditions by FT-IR study using CO as a probe molecule. The unmodified Pt showed three types of CO adsorption peaks of linearly adsorbed CO on a Pt atom (linear-type), bridging CO on two or more Pt atoms (bridge-type) and multi-CO, in which more than one CO molecules are bound to a coordinatively unsaturated Pt atom (multi-type). These bridge-type and multi-type sites indicated the presence of coordinatively unsaturated Pt atoms and this coordinatively unsaturated site favors π interactions with C=C bonds, promoting undesired hydrogenation of C=C bonds. On the other hand, Co-modified Pt catalyst showed only linear-type adsorption peak. Namely, Co-modification effectively blocked low coordination Pt sites and suppressed the undesired hydrogenation of C=C bonds. Secondly, they focused on the position of linear-type CO adsorption peaks. The red shift of linear-type CO adsorption peaks was observed along with Co-decoration (Scheme 1-13), indicating that a charge transfer from Co to Pt occurred. Positively charged Co clusters would attract the carbonyl groups of substrates while the negatively charged Pt surface

destabilized adsorption of C=C bonds and inhibited undesired hydrogenation of C=C bonds. The combination of geometric and electronic modification through the Co decoration realized highly selective hydrogenation of cinnamaldehyde.


Catalyst	Selectivity (%)	Linear peak position of CO (cm^{-1})
4.8 nm Pt	49.1	2060
4.8 nm Pt/Co	99.6	2047
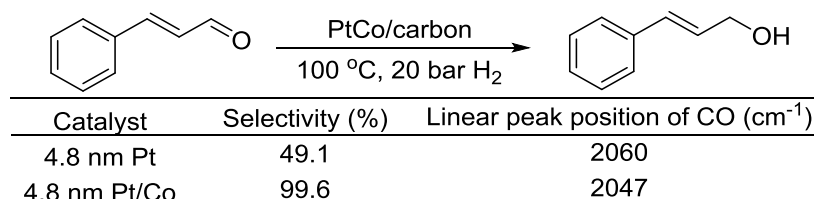
Scheme 1-13. Cinnamylaldehyde hydrogenation using PtCo/carbon catalysts

Selection of suitable two metal components enables alloy nanoparticles to exhibit unprecedented catalysis. For example, Al_2O_3-supported Au-Pd alloy nanoparticles catalyzed tandem oxidation reactions to synthesis *N*-substituted anilines from non-aromatic compounds, whereas their mono-metal counterparts hardly promoted these reactions (Scheme 1-14) [81]. To elucidate active species for this tandem reaction, they performed several control experiments and revealed that mono-metal counterparts could promote elementary reactions of the tandem oxidation. Namely, Au/Al_2O_3 oxidized amines to *N*-alkylimine intermediates and successive aromatization was promoted by Pd nanoparticles. However, the physical mixture of Au/Al_2O_3 and Pd/Al_2O_3 showed much inferior activity to that of $Au-Pd/Al_2O_3$ alloy catalyst (Scheme 1-14-b). The dramatic improvement of activity of mono-metal counterparts in the $Au-Pd/Al_2O_3$ catalyst was due to the charge transfer from Pd to Au. This charge transfer created negatively charged Au and positively charged Pd sites, which is frequently observed in the Au-Pd alloy catalysts [82-85]. During the tandem reaction, negatively charged Au nanoparticles strongly activated molecular oxygen compared to neutral Au nanoparticles and the resulting peroxo species ($Au-O-O^{\delta-}$) promoted a series of oxygenation reactions efficiently.

(a) Tandem oxidation route to *N*-substituted anilines
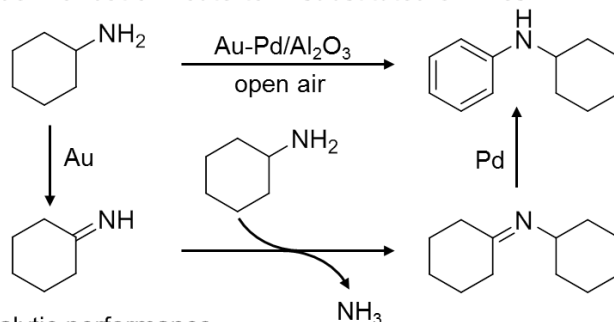
(b) Catalytic performance
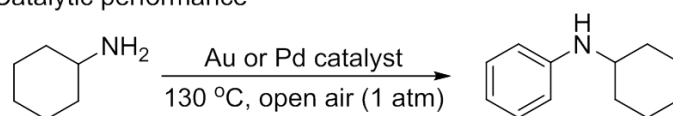
Catalyst	Conversion (%)	Yield of Product (%)
Au-Pd/Al$_2$O$_3$	>99	95
Au/Al$_2$O$_3$	42	<1
Pd/Al$_2$O$_3$	34	<1
Au/Al$_2$O$_3$ + Pd/Al$_2$O$_3$	76	3

Scheme 1-14. Tandem oxidation of cyclohexylamine to *N*-cyclohexylaniline

As stated above, the addition of other metals to form bimetal catalysts can dramatically improve intrinsic catalysis of metal nanoparticles.

3. Purpose of this thesis

Today, the action for environmental conservation has brisked up and attracted enormous attentions all over the world. Especially, in the chemical industry, it is highly required to replace the conventional hazardous processes with environmental-friendly ones. Based on the concept of Green Chemistry, chemical processes in the modern society must attain saving energies and costs, disuse of hazardous reagents and avoidance of large production of chemical wastes. In this context, the development of efficient catalytic systems enabling simple and clean organic transformations is highly required.

Among the catalytic materials, the author focused on supported metal nanoparticles. In addition to the industrial advantages of conventional heterogeneous catalysts such as easy handling, high reusability and thermal stability, supported metal nanoparticle catalysts could show the tailor-made activity for fine chemical syntheses through precise control of their morphologies, chemical compositions, electronic states and suitable selection of their supports as reviewed in previous section. Therefore, the author believes that supported metal nanoparticles are highly promising candidates for the ideal catalysts required in the modern chemical industry.

The main purpose of this thesis is to design and synthesis metal nanoparticle catalysts for effective hydrogenation and dehydrogenation reactions. The precise design of metal nanoparticle catalysts with elaborate nanostructures brings unprecedented and efficient catalysis. Furthermore, the novel design strategy and synthetic techniques expand the catalytic potential of metal nanoparticles. These achievement will allow supported metal nanoparticles to be accepted for selective organic transformations and contribute to the construction of environmental-benign and sustainable chemical industry.

4. Outline of this thesis

The present thesis deals with the studies on the design of supported metal nanoparticle catalysts for chemoselective hydrogenation of functional groups with retaining C=C bonds and efficient dehydrogenative coupling reactions of hydrosilanes.

The Chapter II are described that the design of core-Pd/shell-Ag nanocomposite catalysts (Pd@Ag) for selective semihydrogenation of alkynes. The construction of core-shell nanostructure realized selective semihydrogenation of a wide range of alkynes to the corresponding alkenes under mild reaction conditions with high Z-selectivity (Scheme 1-15).
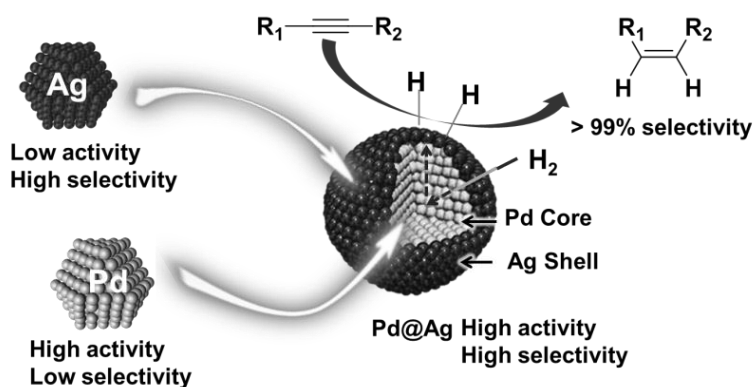

Scheme 1-15. Selective semihydrogenation of alkynes catalyzed by Pd@Ag

The author mentions the green one-step synthesis of CeO_2-covered Au and Ag core-shell nanoparticle catalysts in Chapter III. Simply mixing core and shell metal precursors in the presence of solid base materials in water allowed for the facile fabrication of small CeO_2-covered Au and Ag nanoparticles in one-step. Additionally, the synthesized hydrotalcite-supported CeO_2-covered Au catalyst (Au@CeO_2/HT) promoted chemoselective hydrogenation of unsaturated aldehydes, epoxides and alkynes while retaining C=C bonds (Scheme 1-16).
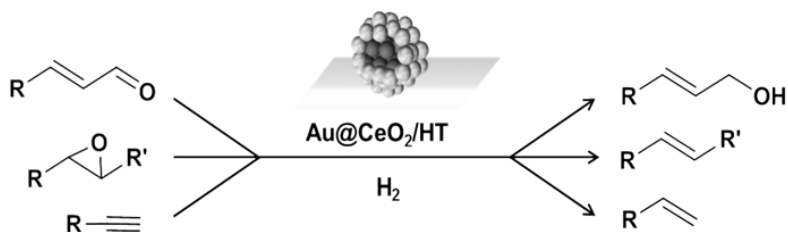

Scheme 1-16. Selective reduction reactions catalyzed by Au@CeO_2/HT catalyst

The next chapter represents the efficient dehydrogenative coupling of hydrosilanes with amines or amides using hydrpxyapatite-supported gold nanoparticle catalyst (Au/HAP). Various silylamines were selectively obtained from diverse combinations of equimolar amounts of hydrosilanes (Scheme 1-17). Furthermore, Au/HAP also promoted selective synthesis of silylamides through the coupling of hydrosilanes with amides, demonstrating the first example of an efficient heterogeneous catalyst.
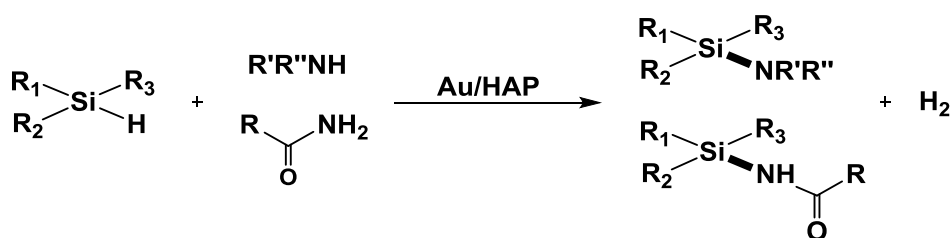
Scheme 1-17. Dehydrogenative coupling of hydrosilanes with amines and amides catalyzed by Au/HAP

In Chapter V and VI, the author demonstrates O_2-enhacement effect on catalytic activity of Au nanoparticles for aqueous oxidation of hydrosilanes to silanols (Scheme 1-18). In this catalytic system, O_2 acted as a non-consumed activator for Au nanoparticles in the oxidation of hydrosilanes, providing an acceleration effect on 200 times the reaction rate relative to Ar atmosphere. Additionally, through the size-selective synthesis of Au nanoparticle catalysts, the author attained further improvement of catalytic activity for the hydrosilane oxidation. Moreover, the author applied this catalytic system as an environmental-friendly H_2-generation system.
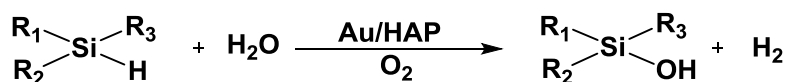
Scheme 1-18. O_2-boosted hydrosilanes oxidation and associated hydrogen production catalyzed by Au nanoparticles

Finally, the author describes overall conclusions of this thesis and the scope for the extensive application of supported metal nanoparticle catalysts.

5. References

[1] *Handbook of Green Chemistry & Technology* (Eds: J. Clark, D. Macquarrie), Wiley-Blackwell, New Jersey, **2002**.

[2] P. Tundo, P. Anastas, D. StC. Black, J. Breen, T. Cllins, S. Memoli, J. Miyamoto, M. Polyakoff, W. Tumas, *Pure Appl. Chem.* **2000**, *72*, 1207-1228.

[3] D. J. Cole-Hamilton, *Science* **2003**, *299*, 1702-1706.

[4] *Handbook of Heterogeneous Catalysis* (Eds: G. Ertl, H. Knözinger, J. Weitkamp), Wiley-VCH, Weinheim, **1997**.

[5] *Clusters and Colloids* (Eds: G. Schmid), Wiley-VCH, Weinheim, **1994**.

[6] L. N. Lewis, *Chem. Rev.* **1993**, *93*, 2693-2730.

[7] R. H. Crabtree, *Chem. Rev.* **2012**, *112*, 1536-1554.

[8] L. N. Lewis, N. Lewis, *J. Am. Chem. Soc.* **1986**, *108*, 7228-7231.

[9] N. T. S. Phan, M. V. D. Sluys, C. W. Jones, *Adv. Synth. Catal.* **2006**, *348*, 609-679.

[10] D. R. Anton, R. H. Crabtree, *Organomet.* **1983**, *2*, 855-859.

[11] R. Jin, *Nanotechnol. Rev.* **2012**, *1*, 31-46.

[12] C. T. Campbell, *Nat. Chem.* **2012**, *4*, 59-598.

[13] G. Pacchioni, *Phys. Chem. Chem. Phys.* **2013**, *15*, 1737-1757.

[14] G. R. Jenness, J. R. Schmidt, *ACS Catal.* **2013**, *3*, 2881-2890.

[15] C. S. Ewing, G. Veser, J. J. McCarthy, J. K. Johnson, D. S. Lambrecht, *J. Phys. Chem. C* **2015**, *119*, 19934-19940.

[16] S. Carrettin, P. Concepción, A. Corma, J. M. L. Nieto, V. F. Puntes, *Angew. Chem. Int. Ed.* **2004**, *43*, 2538-2540.

[17] J. Guzman, S. Carrettin, J. C. Fierro-Gonzalez, Y. Hao, B. C. Gates, A. Corma, *Angew. Chem. Int. Ed.* **2005**, *44*, 4778-4781.

[18] X. Zhang, A. Corma, *Angew. Chem. Int. Ed.* **2008**, *47*, 4358-4361.

[19] A. Corma, C. González-Arellano, M. Iglesias, F. Sánchez, *Angew. Chem. Int. Ed.* **2007**, *46*, 7820-7822.

[20] C. González-Arellano, A. Abad, A. Corma, H. Garcia, M. Iglesias, F. Sánchez, *Angew. Chem. Int. Ed.* **2007**, *46*, 1536-1538.

[21] L. Alves, B. Ballesteros, M. Boronat, J. R. Cabrero-Antonino, P. Concepion, A. Corma, M. A. Correa-Duartel, E. Mendoza, *J. Am. Chem. Soc*. **2011**, *133*, 10251-10261.

[22] Y. Yamada, C.-K. Tsung, W. Huang, Z. Huo, S. E. Habas, T. Soejuma, C. E. Aliaga, G. A. Somorjai, P. Yang, *Nat. Chem*. **2011**, *3*, 372-376.

[23] A. Hervier, L. R. Baker, K. Komvopoulos, G. A. Somorjai, *J. Chem. Phys. C* **2011**, *115*, 22960-22964.

[24] E. Gross, G. A. Somorjai, *Top. Catal.* **2013**, *56*, 1049-1058.

[25] B. Zhang, X.-W. Guo, H. Liang, H. Ge, X. Gu, S. Chen, H. Yang, Y. Qin, *ACS Catal*. **2016**, *6*, 6560-6566.

[26] G. Chen, C. Xu, X. Huang, J. Ye, L. Gu, G. Li, Z. Tang, B. Wu, H. Yang, Z. Zhao, Z. Zhou, G. Fu, N. Zheng, *Nat. Mater*. **2016**, *15*, 564-569.

[27] W. Shi, B. Zhang, Y. Lin, Q. Wang, Q. Zhang, D. S. Su, *ACS Catal*. **2016**, *6*, 7844-7854.

[28] J. M. Planeix, N. Coustel, B. Coq, V. Brotons, P. S. Kumbhar, R. Dutarte, P. Geneste, P. Bernier, P. M. Ajayan, *J. Am. Chem. Soc*. **1994**, *116*, 7935-7936.

[29] Y. Motoyama, Y. Lee, K. Tsuji, S.-H. Yoon, I. Mochida, H. Nagashima, *ChemCatChem* **2011**, *3*, 1578-1581.

[30] B. Zhang, D. S. Su, *ChemCatChem* **2015**, *7*, 3639-3645.

[31] C. T. Campbell, C. H. F. Peden, *Science* **2005**, *309*, 713-714.

[32] L. Vivier, D. Duprez, *ChemSusChem* **2010**, *3*, 654-678.

[33] X. Chen, S. S. Mao, *Chem. Rev*. **2007**, *107*, 2891-2959.

[34] T. Yamaguchi, *Catal. Today* **1994**, *20*, 199-218.

[35] H. G. Manyar, C. Paun, R. Pilus, D. W. Rooney, J. M. Thompson, C. Hardacre, *Chem. Commun*. **2010**, *46*, 6279-6281.

[36] M. J. Mendes, O. A. A. Santos, E. Jordão, A. M. Silva, *Appl. Catal. A: Gen.* **2001**, *217*, 253-262.

[37] A. Corma, P. Serna, *Science* **2006**, *313*, 332-334.

[38] A. J. R. Hensley, Y. Hong, R. Zhang, H. Zhang, J. Sun, Y. Wang, J.-S. McEwen, *ACS Catal*. **2014**, *4*, 3381-3392.

[39] K. Kandel, U. Chaudhary, N. C. Nelson, I. I. Slowing, *ACS Catal*. **2015**, *5*, 6179-6723.

[40] M. Manikandan, A. K. Venuqopal, A. S. Naqpure, S. Chilukuri, T. Raja, *RSC Adv*. **2016**, *6*, 3888-3898.

[41] T. Mitsudome, Y. Mikami, T. Mizugaki, K. Jitsukawa, K. Kaneda, *Angew. Chem. Int. Ed*. **2008**, *47*, 138-141.

[42] T. Mitsudome, A. Noujima, T. Mizugaki, K. Jitsukawa, K. Kaneda, *Green. Chem*. **2009**, *11*, 793-797.

[43] T. Mitsudome, A. Noujima, T. Mizugaki, K. Jitsukawa, K. Kaneda, *Adv. Synth. Catal.* **2009**, *351*, 1890-1896.

[44] A. Noujima, T. Mitsudome, T. Mizugaki, K. Jitsukawa, K. Kaneda, *Angew. Chem. Int. Ed.* **2011**, *50*, 2986-2989.

[45] A. Noujima, T. Mitsudome, T. Mizugaki, K. Jitsukawa, K. Kaneda, *Molecules* **2011**, *16*, 8209-8227.

[46] A. Noujima, T. Mitsudome, T. Mizugaki, K. Jitsukawa, K. Kaneda, *Chem. Commun*. **2012**, *48*, 6723-6725.

[47] T. Mitsudome, Y. Mikami, M. Matoba, T. Mizugaki, K. Jitsukawa, K. Kaneda, *Angew. Chem. Int. Ed.* **2012**, *51*, 136-139.

[48] T. Mitsudome, M. Matoba, T. Mizugaki, K. Jitsukawa, K. Kaneda, *Chem. Eur. J.* **2013**, *19*, 5255-5258.

[49] T. Mitsudome, M. Matoba, T. Mizugaki, K. Jitsukawa, K. Kaneda, *Chem. Lett.* **2013**, *42*, 660-662.

[50] T. Mitsudome, M. Yamamoto, Z. Maeno, T. Mizugaki, K. Jitsukawa, K. Kaneda, *J. Am. Chem. Soc.* **2015**, *137*, 13452-13455.

[51] Y. Nie, S. Jaenicke, H. van Bekkum, G.-K. Chuah, *J. Catal.* **2007**, *246*, 223-231.

[52] M. J. Climent, A. Corma, S. Ibora, M. Mifsud, *J. Catal.* **2007**, *247*, 223-230.

[53] J. Shi, *Chem. Rev.* **2013**, *113*, 2139-2181.

[54] M. J. Climent, A. Corma, S. Ibora, M. J. Sabater, *ACS Catal.* **2014**, *4*, 870-891.

[55] M. Zhao, K. Deng, L. He, Y. Liu, G. Li, H. Zhao, Z. Tang, *J. Am. Chem. Soc.* **2014**, *136*, 1738-1741.

[56] T. Yatabe, X. Jin, K. Yamaguchi, N. Mizuno, *Angew. Chem. Int. Ed.* **2015**, *54*, 13302-13306.

[57] C. S. Hinde, W. R. Webb, B. K. J. Chew, H. R. Tan, W.-H. Zhang, T. S. A. Hor, R. Raja, *Chem. Commun.* **2016**, *52*, 6557-6560.

[58] G.C. Bond, *Sur. Sci.* **1985**, *156*, 966-981.

[59] S. H. Oh, C. C. Eickel, *J. Catal.* **1991**, *128*, 526-536.

[60] Y. Sun, Y. Xia, *Science* **2002**, *298*, 2176-2179.

[61] B. Lim, M. Jiang, J. Tao, P. H. C. Camargo, Y. Zhu, Y. Xia, *Adv. Funct. Mater.* **2008**, *19*, 189-200.

[62] Y. Zhang, M. E. Grass, J. N. Kuhn, F. Tao, S. E. Habas, W. Huang, P. Yang, G. A. Somorjai, *J. Am. Chem. Soc.* **2008**, *130*, 5868-5869.

[63] C. Wang, H. Daimon, T. Onodera, T. Koda, S. Sun, *Angew. Chem. Int. Ed.* **2008**, *47*, 3588-3591.

[64] C.-K. Tsang, J. N. Kuhn, W. Huang, C. Aliaga, L. I. Hung, G. A. Somorjai, P. Yang, *J. Am. Chem. Soc.* **2009**, *131*, 5816-5822.

[65] R. Jin, *Nanotechnol. Rev*. **2012**, *1*, 31-56.

[66] K. An, G. A. Somorjai, *ChemCatChem* **2012**, *4*, 1512-1524.

[67] E. Schmidt, A. Vargas, T. Mallat, A. Baiker, *J. Am. Chem. Soc.* **2009**, *131*, 12358-12367.

[68] L. Hu, X. Cao, D. Ge, H. Hong, Z. Guo, L. Chen, X. Sun, J. Tang, J. Zheng, J. Lu, H. Gu, *Chem. Eur. J.* **2011**, *17*, 14283-14287.

[69] Z.-N. Xu, J. Sun, C.-S. Lin, X.-M. Jiang, Q.-S. Chen, S.-Y. Peng, M.-S. Wang, G.-C. Guo, *ACS Catal*. **2013**, *3*, 118-122.

[70] K. Chanda, S. Rej, M. H. Huang, *Nanoscale* **2013**, *5*, 12494-12501.

[71] J. Chung, C. Kim, H. Jeong, T. Yu, D. H. Binh, J. Jang, J. Lee, B. M. Kim, B. Lim, *Chem. Asian. J.* **2013**, *8*, 919-925.

[72] M. H. Huang, S.Rei, S.-C. Hsu, *Chem. Commun*. **2014**, *50*, 1634-1644.

[73] K.. Chanda, S. Rei, S.-Y. Liu, M. H. Huang, *ChemCatChem* **2015**, *7*, 1813-1817.

[74] L. Guczi, *Catal. Today* **2005**, *101*, 53-64.

[75] I. N. Francesco, F. Fontaine-Vive, S. Antonini, *ChemCatChem* **2014**, *6*, 2784-2791.

[76] M. Sankar, N. Dimitratos, P. J. Miedziak, P. P. Wells, C. J. Kiely, G. J. Hutchings, *Chem. Soc. Rev.* **2012**, *41*, 8099-8139.

[77] G.-H. Wang, J. Hilgert, F. H. Richter, F. Wang, H.-S. Bongard, B. Spliethoff, C. Weidenthaler, F. Schüth, *Nat. Mater*. **2014**, *13*, 293-300.

[75] L. Zhang, Z. Xie, J. Gong, *Chem. Soc. Rev.* **2016**, *45*, 3916-3934.

[76] R. K. Rai, D. Tyagi, K. Gupta, S. K. Singh, *Catal. Sci. Technol.* **2016**, *6*, 3341-3361.

[77] S. C. Tsang, N. Cailuo, W. Oduro, A. T. S. Kong, L. Clifton, K. M. K. Yu, B. Thiebaut, J.

Cookson, P. Bishop, *ACS Nano* **2008**, *2*, 2547-2553.

[81] K. Taniguchi, X. Jin, K. Yamaguchi, N. Mizuno, *Chem. Commun*. **2015**, *51*, 14969-14972.

[82] D. I. Enache, J. K. Edwards, P. Landon, B. Solsona-Espriu, A. F. Carley, A. A. Herzig, M. Watanabe, C. J. Kiely, D. W. Knight, G. J. Hutchings, *Science* **2006**, *311*, 362-365.

[83] J. Pritchard, M. Piccinini, R. Tiruvalam, Q. He, N. Dimitratos, J. A. Lopez-Sanchez, D. J. Morgan, A. F. Carley, J. K. Edwards, C. J. Kiely, G. J. Hutchings, *Catal. Sci. Technol*. **2013**, *3*, 308-317.

[84] S. Nishimura, Y. Yakita, M. Katayama, K. Higashimine, K. Ebitani, *Catal. Sci. Technol.* **2013**, *3*, 351-359.

[85] Z. Chen, S. Wang, C. Lian, Y. Liu, D. Wang, C. Chen, Q. Peng, Y. Liu, *Chem. Asian. J*. **2016**, *11*, 351-355.

Chapter II.

Selective Semihydrogenation of Alkynes to Alkenes
Using Pd-Core/Ag-Shell Nanocomposite Catalysts

1. Introduction

Nano-structured composites with a core (inner material) and shell (outer layer) structure, so-called core-shell materials, have attracted enormous attention as highly functionalized nanoarchitectures in diverse areas such as sensors [1-3], quantum dots [4, 5], photonic crystals [6-8] and catalysts [9-14]. The extensive study on design of core-shell materials stems from their own intriguing characteristics, including optical, electronic, and chemical properties. In the catalytic applicability of core-shell nanoparticles, Chenon *et al*. developed the magnetic and catalytic Co@Pt nanoparticles for hydrogenation of olefins [12]. The developed nanoparticle catalyst showed high activity for hydrogenation under ambient conditions and was magnetically separable after the reactions. This dual functionality was attributed to the combination of high hydrogen activity of Pt shells and magnetism of Co oxide cores. Wang *et al*. demonstrated size-selective catalysis for the alcohol oxidation using mesoporous SiO_2-covered Pd core-shell nanoparticles (Pd/SiO_2@$n$$SiO_2$) [13]. With adjusting pore-sizes of SiO_2, in the mixture of benzylalcohol and 3,5-di-t-butylbenzylalcohol, Pd/SiO_2@$n$$SiO_2$ oxidized benzylalcohol to benzaldehyde size-selectively whereas bulky 3,5-di-t-butylbenzylalcohol was intact.

The semihydrogenation of alkynes to alkenes is one of the most important and fundamental reactions in manufacturing processes of bulk and fine chemicals [15, 16]. In this context, Lindlar catalyst (Pd/$CaCO_3$ treated by Pb salts) has been a good first port of call in the synthesis of diverse alkenes [17]. However, the Lindlar catalyst has serious drawbacks such as high toxicity of Pb species and the low alkene selectivity when employing terminal alkynes due to the rapid overhydrogenation of terminal alkenes to alkanes. Therefore, the development of the alternative Pb-free catalysts using Pd [18-26], Ni [27, 28], Cu [29], Ru [30] and Au [31-34] have been extensively studied. Ohkuma *et al.* developed highly active Pd nanoparticles -tetrabutylammonium borohydride (Pd-(C_4H_9)$_4$$NBH_4$) catalyst system for selective

semihydrogenation [20]. Pd-$(C_4H_9)_4$NBH$_4$ effectively hydrogenated 4-octyne to *trans*-4-octene under 8 atm of H$_2$, where the turnover frequency and turnover number reached 2700 min^{-1} and 20000, respectively. However, the substrate-applicability of the developed Pd catalyst was limited to internal alkenes; the overhydrogenation of terminal alkenes to alkanes occurred at high conversion level. Alonso *et al.* demonstrated Ni nanoparticle-catalyzed semihydrogenation of various functional alkynes including amines, ethers, carboxylic acids, silanes and hydroxyl moieties although requiring Li additives [28]. The above background of semihydorgneation of alkynes clearly highlights that more environmentally benign and efficient catalysts applicable to terminal alkynes is highly desired

It is well known that unmodified Pd nanoparticles inherently show high catalytic activity for hydrogenation of alkynes, but low selectivity for alkenes [20-23, 25]. For example, Sajiki *et al.* revealed that boron nitride-supported Pd nanoparticles (unmodified catalyst) hydrogenated alkynes to alkanes rapidly whereas amine-decorated catalyst exhibited high selectivity for the corresponding alkenes [23]. In contrast, Ag nanoparticles has extremely low catalytic activity for semihydrogenation, requiring high temperature or high H$_2$ pressure, despite intrinsically showing high alkene-selectivity due to the rather weak complexation of Ag with alkenes [35-37]. In Ag/SiO$_2$ system reported by Copèret *et al.* [37], semihydrogenation of 1-hexyne was performed at 200 ^{o}C under 1 atm of H$_2$ and the developed catalyst showed 94% selectivity in 20% conversion.

In consideration of beneficial properties of Pd and Ag nanoparticles, it was anticipated that the construction of a bimetallic core-shell nanocomposite catalyst consisting of Pd nanoparticles in the core and Ag nanoparticles in the shell (Pd@Ag) would address the trade-off between activity and selectivity for Pd and Ag nanoparticles in semihydrogenation. This concept of Pd@Ag represents the building of a compatible relationship between Pd, with its high activity, and Ag, with its high alkene-selectivity, by construction of a core-shell structure. Pd nanoparticles in the core store hydrogen to form palladium-hydride (PdH) [38-40] through the H$_2$-permeable Ag shell nano-layer

[41-43]. The inner PdH serves hydrogen to the outer Ag shell, providing the Pb-free and selective semihydrogenation of alkynes occurring on the Ag surface. Simultaneously, coating the Pd nanoparticles by a Ag layer results in efficient suppression of the overhydrogenation of alkenes at the Pd surface. This complementary action of Pd and Ag, in which the advantages of Pd and Ag are integrated while their disadvantages are remedied in a synergistic manner, allows selective semihydrogenation under mild reaction conditions (Figure 2-1).
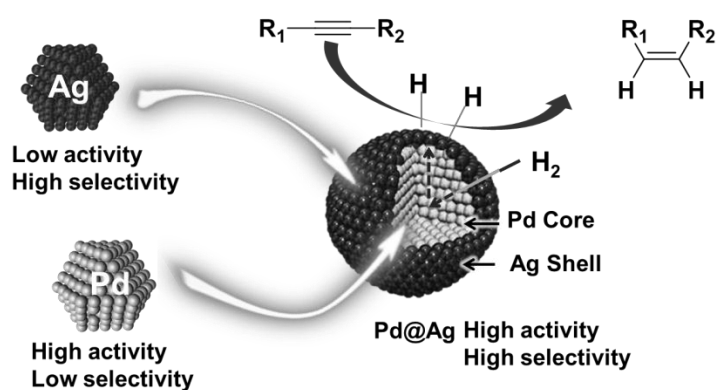
Figure 2-1. Design concept of complementary bimetallic core-Pd/shell-Ag catalyst for selective semihydrogenation of alkynes

This chapter demonstrates the development of core-Pd/shell-Ag nanocomposite catalyst for selective semihydrogenation of terminal and internal alkynes to the corresponding alkenes with high Z-selectivity. The rational design and precise fabrication of the nanocomposite catalysts provided highly selective catalysis for Pb-free semihydrogenation under mild reaction conditions without any additives.

2. Experimental section

2-1. General

All organic reagents were purified before use. Pd(acac)$_2$ was obtained from Sigma-Aldrich. Ag(NO$_3$) and HAP (Apatite HAP, monoclinic) were purchased from Wako Pure Chemical Co., Ltd. GC-FID and GC-MS were performed on a Shimadzu GC-2014 instrument equipped with a Unisole 30 T and a GCMS-QP2010 SE instrument equipped with an Inert Cap WAX-HT capillary column (30 m × 0.25 mm i.d., 0.25 μm), respectively. Inductively coupled plasma measurements were performed on a SII Nano Technology SPS7800 instrument. ^{1}H and ^{13}C nuclear magnetic resonance (NMR) spectra were recorded on a JEOL JNM-ESC400 spectrometer and the chemical shifts are reported in ppm from TMS as a reference. Transmission electron microscopy (TEM) observations were carried out using a FEI Tecnai G2 20ST instrument operated at 200 kV. Scanning transmission electron microscopy (STEM) images with elemental maps were collected using a FEI Titan Cubed G2 60-300 instrument operated at 300 kV with a probe size of 30 pm, and equipped with Super-X energy-dispersive X-ray spectroscopy (EDX) detector. Elemental mapping based on quantification analysis of EDX spectra was carried out using Esprit. Raman spectra were recorded on a confocal Raman microscopy (LabRAM HR-800, Horiba, Ltd., Kyoto, Japan).

2-2. Preparation of catalysts

Preparation of Pd seed: Pd(acac)$_2$ (0.1 mmol) and PVA (0.055 g) were added to ethylene glycol (20 ml) and heated at 150 °C under stirring. After 30 min, the reaction was stopped and acetone (20 mL) was added. The Pd seeds were collected by centrifugation (4000 rpm × 5 min) and dispersed in deionized water (10 mL).

Preparation of single Pd nanoparticles loaded on HAP: HAP (1.0 g) was added to the above aqueous Pd seed colloid solution (30 mL, 0.33 × 10^{-2} M) and stirred for 1 h. The resulting slurry was filtered, washed with deionized water and dried *in vacuo*, yielding Pd/HAP as gray powder.

Preparation of Pd@Ag core-shell nanoparticles: The obtained Pd seed aqueous solution (10 mL, 1.0×10^{-2} M) was added to 10 mL of 0.5 M CTAB solution and heated at 60 °C for 10 min. Then, L-ascorbic acid (5 equivalent to the Ag amount) and silver nitrate (Ag/Pd = 0.10, 0.15, 0.20, 0.25, 0.50) were added and the reaction mixture was kept at 60 °C for 2 h under stirring. The obtained Pd@Ag catalysts were labeled as Pd@Ag-X where X denotes the ratio of Ag/Pd.

Preparation of HAP-supported Pd@Ag core-shell nanoparticles: HAP (1.0 g) was added to the prepared Pd@Ag colloid solution and stirred for 1 h. The obtained slurry was filtered, washed with deionized water and dried *in vacuo*, yielding Pd@Ag loaded on HAP as gray powder.

Preparation of single Ag nanoparticles loaded on HAP: Single Ag nanoparicles loaded on HAP were prepared according to our previous report [44]. HAP (2.0 g) was soaked in a 150 mL aqueous solution of silver nitrate (6.7×10^{-3} M) and stirred at room temperature for 6 h. The resulting slurry was filtered, washed, and dried at room temperature *in vacuo*. Next, the HAP containing Ag was treated with an aqueous solution of KBH₄ (5.0×10^{-2} M) for 1 h at room temperature. Again, the slurry was filtered, washed, and dried at room temperature in vacuo, giving HAP-supported Ag nanoparticles.

Preparation of Pd-Ag alloys: Palladium trifluoroacetate (0.10 mmol) and silver nitrate (0.020 mmol) were added to water (20 ml) in the presence of PVP (0.10 g) and then stirred at room temparature. After 5 min, aqueous solution of KBH₄ (10 mL, 5.0×10^{-2} M) was added to the mixture and Pd-Ag colloid solution was obtained. HAP (1.0 g) was added to the prepared Pd-Ag solution and stirred for 1 h. The obtained slurry was filtered, washed with ethanol and dried *in vacuo*.

2-3. Reaction procedure

Typical reaction procedure: A typical reaction procedure for semihydrogenation of alkynes using Pd@Ag-0.20 was as follows. Pd@Ag-0.20 (0.10 g: Pd 0.010 mmol, Ag 0.0020 mmol) was placed in a reaction vessel connected to a gas bag filled with 1 atm of H₂. Next, EtOH (2 mL) and alkynes (0.3

mmol) were added to the reaction vessel and the mixture was stirred at room temperature. The yields of the products were determined by GC using naphthalene as an internal standard.

Reuse experiment: After semihydrogenation under the above typical reaction conditions, Pd@Ag-0.20 loaded on HAP was recovered by simple filtration and washed with EtOH. The used catalyst was treated again under identical reaction conditions. The yields of the products were determined by GC using naphthalene as an internal standard.

Hydrogenation of 1 using a continuous plug flow reactor: Pd@Ag-0.20 (0.50 g) and SiO$_2$ (Wakogel C-200: 75-150 μm, 0.6 g) as a filler were added to hexane (10 mL) and the mixture was stirred for 5 min, followed by evaporation to dryness at room temperature. The obtained powder was packed in a stainless steel column (inner diameter: 5.0 mm, length: 200 mm, volume: 3925 mm^3). A solution of **1** in ethanol (1.10 g: 10 mmol in 100 mL) was introduced to the column (4.2 mL/h), which was maintained at room temperature, along with a flow of hydrogen gas (60 mL/h).

2-3. CO adsorption FTIR experiments

FT-IR data were collected on a JASCO FT-IR 410 spectrometer equipped with a MCT detector. Self-supporting pellets were prepared from the sample powders and treated directly in the IR cell, which allowed for thermal treatments under a controlled atmosphere. The sample was first pretreated at 300 K under outgassing for 30 min, then exposed to 15 mmHg CO for 30 min. After evacuation (< 0.1 mmHg) for 5 min, IR spectra were recorded.

2-4. CO adsorption FTIR experiments

Raman spectra (Figure 2-15-A): Metal nanoparticle ethanol suspension (10 μL, M:0.1 μmol) were mixed with 5 mL of ethanol containing phenylacetylene (0.12 mM) at room temperature. The Raman spectra were recorded from solution phase with 20x objective lens. The collection time was 20 s for all samples, together with a power of 100 mW for 532 nm excitation laser.

In situ SERS monitoring of semihydrogenation catalyzed by Pd@Ag-0.20 (Figure 2-15-B): Pd@Ag-0.20 ethanol suspension (5 mL, Pd: 0.05 mmol, Ag: 0.01 mmol) was placed in a reaction vessel connected to a gas bag filled with 1 atm of H_2. Next, phenylacetylene (0.4 mmol) was added to the reaction vessel and the mixture was stirred at room temperature. We withdrew 0.2 mL of the reaction solution every 6 h and 20 μL were used for measurements. The Raman spectra were recorded from solution phase with 20x objective lens. The collection time was 20 s for all samples, together with a power of 100 mW for 532 nm excitation laser. The conversions of phenylacetylene were determined by GC.

2-5. H_2-D_2 exchange reaction

The H_2-D_2 exchange reaction was performed in a closed gas-circulation system equipped with an online quadrupole mass spectrometer (BELMass-S, BEL Japan, Inc.). The prepared single Ag/HAP (0.05 g; Ag 5 μmol) was placed in a reactor followed by evacuation of the air. A mixture of H_2 (0.1 mmol) and D_2 (0.1 mmol) gases was introduced to the reaction system and the total pressure adjusted with Ar to 720 Torr. After the H_2-D_2 exchange reaction at room temperature for 20 h, the gas phase was analyzed by monitoring the signals of $m/z = 2$, 3, and 4.

2-6. Product identification

The products were characterized by GC, GC-MS, and NMR. Retention times (GC) and chemical shifts (^1H and ^{13}C NMR) of the products were in agreement with those of authentic samples or previously reported values.

1-Octene: CAS registry No. [111-66-0] (Table 2-3, Entry 1)

^1H NMR (400 MHz, CDCl$_3$): δ 5.76-5.86 (m, 1H), 4.90-5.20 (m, 2H), 2.04 (dd, J = 14.8 Hz, J = 6.4 Hz, 2H), 1.21-1.46 (m, 8H), 0.87 (t, J = 8.0 Hz, 3H). ^{13}C NMR (100 MHz, CDCl$_3$): δ 138.5, 115.4, 114.0, 33.8, 31.7, 28.6, 22.6, 14.0 ppm.

4-Penten-1-ol: CAS registry No. [821-09-0] (Table 2-3, Entry 3)

^{1}H NMR (400 MHz, CDCl$_3$): δ 5.77-5.93 (m, 1H), 4.94-5.13 (m, 2H), 3.59-3.75 (m, 2H), 2.11-2.21 (m, 2H), 1.93 (br s, 1H), 1.66-1.72 (m, 2H). ^{13}C NMR (100 MHz, CDCl$_3$): δ 138.2, 114.8, 62.3, 31.7, 30.0 ppm.

6-Chloro-1-hexene: CAS registry No. [928-89-2] (Table 2-3, Entry 4)

^{1}H NMR (400 MHz, CDCl$_3$): δ 5.73-5.91 (m, 1H), 4.91-5.13 (m, 2H), 3.53 (t, J = 6.4 Hz, 2H), 2.10 (dd, J = 15.6 Hz, J = 7.2 Hz, 2H), 1.58-1.75 (m, 2H), 1.47-1.58 (m, 2H). ^{13}C NMR (100 MHz, CDCl$_3$): δ 138.1, 114.9, 44.9, 32.9, 31.9, 26.1 ppm.

5-Hexenoic acid: CAS registry No. [1577-22-6] (Table 2-3, Entry 5)

^{1}H NMR (400 MHz, CDCl$_3$): δ 11.0 (br s, 1H), 5.67-5.86 (m, 1H), 4.93-5.08 (m, 2H), 2.37 (t, J = 9.2 Hz, 2H), 2.03-2.17 (m, 2H), 1.71-1.80 ppm (m, 2H). ^{13}C NMR (100 MHz, CDCl$_3$): δ 179.9, 137.5, 115.5, 33.2, 32.9, 23.7 ppm.

5-Hexenenitrile: CAS registry No. [5048-19-1] (Table 2-3, Entry 6)

^{1}H NMR (400 MHz, CDCl$_3$): δ 5.69-5.80 (m, 1H), 5.03-5.14 (m, 2H), 2.35 (t, J = 7.2 Hz, 2H), 2.21 (dd, J = 13.2 Hz, J = 7.2 Hz, 2H), 1.76 (m, 2H); ^{13}C NMR (100 MHz, CDCl$_3$): δ 135.9, 119.5, 116.6, 32.3, 24.4, 16.3 ppm.

Vinylcyclohexane: CAS registry No. [695-12-5] (Table 2-3, Entry 7)

^{1}H NMR (400 MHz, CDCl$_3$): δ 5.69-5.94 (m, 1H), 4.79-5.12 (m, 2H), 1.86-2.09 (m, 1H), 1.45-1.85 (m, 5H), 0.87-1.44 (m, 5H). ^{13}C NMR (100 MHz, CDCl$_3$): δ 144.8, 111.5, 41.5, 32.5, 26.2, 26.0 ppm.

Allylbenzene: CAS registry No. [300-57-2] (Table 2-3, Entry 8)

^{1}H NMR (400 MHz, CDCl$_3$): δ 7.10-7.44 (m, 5H), 5.92-6.03 (m, 1H), 5.04-5.11 (m, 2H), 3.34 ppm (d, J = 6.8 Hz, 2H). ^{13}C NMR (100 MHz, CDCl$_3$): δ 140.0, 137.4, 128.5, 128.4, 126.0, 115.7, 40.2 ppm.

4-Phenyl-1-butene: CAS registry No. [768-56-9] (Table 2-3, Entry 9)

^{1}H NMR (400 MHz, CDCl$_3$): δ 7.10-7.44 (m, 5H), 5.66-6.03 (m, 1H), 4.84-5.18 (m, 2H), 2.54-2.95 (m, 2H), 2.21-2.50 ppm (m, 2H). ^{13}C NMR (100 MHz, CDCl$_3$): δ 141.8, 138.1, 128.4, 128.2, 125.8, 114.9, 35.5, 35.4 ppm.

4-Octene: CAS registry No. [7642-15-1] (Table 2-3, Entry 10)

^{1}H NMR (400 MHz, CDCl$_3$): δ 5.34-5.38 (m, 2H), 2.01 (dd, J = 13.2 Hz, J = 7.2 Hz, 4H), 1.37 (dd, J = 14.4 Hz, J = 7.2 Hz, 4H), 0.90 (t, J = 7.6 Hz, 6H). ^{13}C NMR (100 MHz, CDCl$_3$): δ 130.5, 29.3, 22.9, 13.7 ppm.

3-Hexen-1-ol: CAS registry No. [928-96-1] (Table 2-3, Entry 11)

^{1}H NMR (400 MHz, CDCl$_3$): δ 5.53-5.60 (m, 1H), 5.29-5.38 (m, 1H), 3.64 (t, J = 6.4 Hz, 2H), 2.34 (dd, J = 14 Hz, J = 6.8 Hz, 2H), 2.08 (m, 2H), 1.59 (s, 1H), 0.97 (t, J = 10 Hz, 3H). ^{13}C NMR (100 MHz, CDCl$_3$): δ 134.5, 123.8, 62.3, 30.6, 20.6, 14.1 ppm.

2-Hexen-1-ol: CAS registry No. [928-94-9] (Table 2-3, Entry 12)

^{1}H NMR (400 MHz, CDCl$_3$): δ 5.50-5.67 (m, 2H), 4.19 (d, J = 6.0 Hz, 2H), 2.06 (dd, J = 14.8 Hz, J = 7.6 Hz, 2H), 1.57 (br s, 1H), 1.40-1.44 (m, 2H), 0.90 (t, J = 10.4 Hz, 3H). ^{13}C NMR (100 MHz, CDCl$_3$): δ 132.8, 128.5, 58.5, 29.4, 22.7, 13.6 ppm.

Ethyl 2-butenoate: CAS registry No. [6776-19-8] (Table 2-3, Entry 13)

^{1}H NMR (400 MHz, CDCl$_3$): δ 6.90-7.03 (m, 1H), 5.78-5.88 (m, 1H), 4.18 (dd, J = 13.6 Hz, J = 7.2 Hz, 2H), 1.86-1.88 (d, 3H), 1.27 (t, J = 8.4 Hz, 3H).

Diethyl maleate: CAS registry No. [141-05-9] (Table 2-3, Entry 14)

^{1}H NMR (400 MHz, CDCl$_3$): δ 6.22 (s, 2H), 4.25 (dd, J = 13.2 Hz, J = 6.8 Hz, 4H), 1.31 ppm (t, J = 7.6 Hz, 6H). ^{13}C NMR (100 MHz, CDCl$_3$): δ 165.1, 129.7, 61.3, 13.9 ppm.

***N, N*-Diethyl-2-nonen-1-amine**: CAS registry No. [86112-00-7] (Table 2, Entry 15)

^{1}H NMR (400 MHz, CDCl$_3$): δ 5.43-5.59 (m, 2H), 3.10 (d, J = 6.4 Hz, 2H), 2.52 (dd, J = 12.0 Hz, J

= 6.4 Hz, 4H), 2.06 (t, J = 6.5 Hz, 2H), 1.23-1.40 (m, 8H), 1.04 (t, J = 6.8 Hz, 6H), 0.85-0.92 (m,

3H). ^{13}C NMR (100 MHz, CDCl$_3$): δ 132.4, 126.8, 49.6, 46.7, 31.7, 29.6, 29.0, 27.5, 22.6, 14.0, 11.8

3. Results and Discussion

Representative images of Pd@Ag-0.20 observed by transmission electron microscopy

(TEM) and high-angle annular dark-field STEM (HAADF-STEM) are depicted in Figure 2-2. It can

be seen that the synthesized nanoparticles had a mean diameter of 26.2 ± 5.7 nm (Figure 2-2-a). In

the HAADF-STEM image of Pd@Ag, well-defined lattice fringes were observed (Figure 2-2-b). The

detected lattice fringes had d-spacing attributed to Ag {111} (2.36 Å) and Ag {200} (2.04 Å). This

fact indicates that crystalline Ag grows on the surface of the Pd seed. The elemental distribution of

Ag on the Pd nanoparticles in Pd@Ag (Figure 2-2-c) was examined by scanning TEM (STEM)

coupled with energy-dispersive X-ray spectroscopy (EDX) (Figures 2-2-d, e, and f). Elemental

mapping of Pd@Ag based on quantification analysis of EDX spectra clearly revealed that it

comprised Pd nanoparticles in the core (Figure 2-2-d) and a nano-layer of Ag with a thickness of ca.

1 nm in the shell (Figure 2-2-e). The formation of a thin shell of Ag was also supported by XRD

analysis, as no peak attributed to the formation of Ag nanoparticles or an alloy of Ag and Pd was

observed around 35–50° (Figure 2-3).
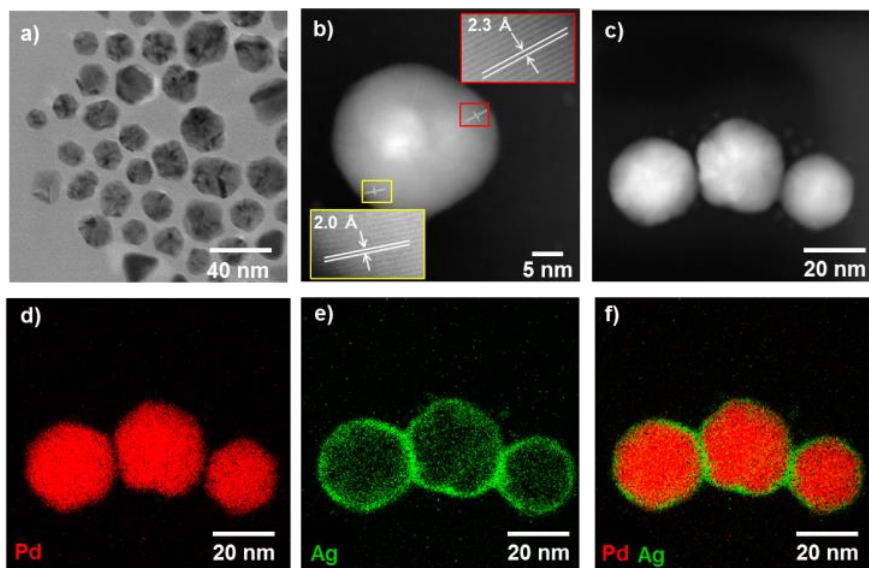
Figure 2-2. Composition and structural analysis of Pd@Ag-0.20. a) TEM image. b) and c) HAADF-STEM images. Elemental mapping images of d) Pd and e) Ag. f) Composite overlay image formed from d) and e).
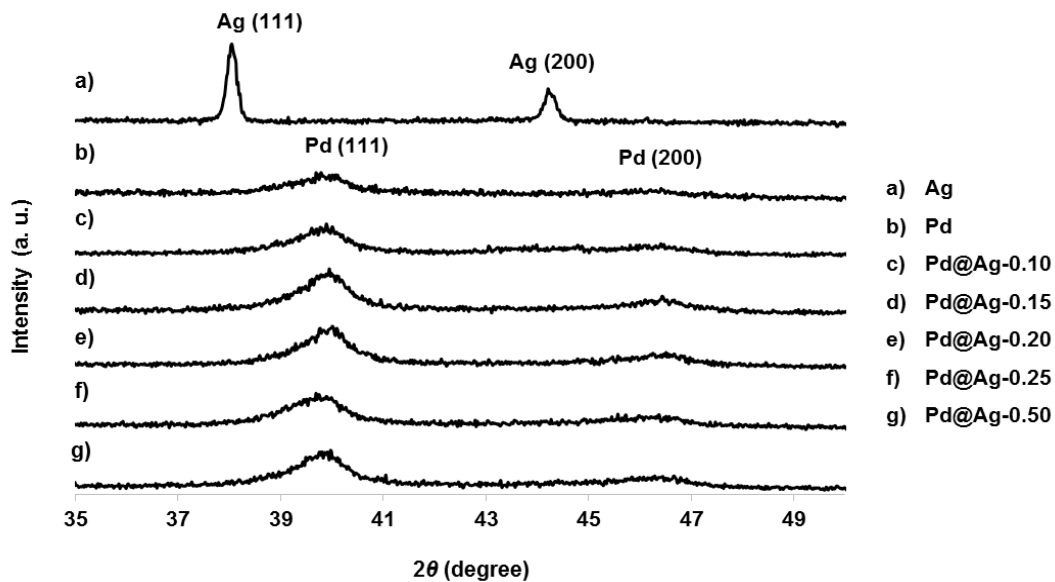
Figure 2-3. XRD measurements of Pd@Ag-X and single Pd and Ag nanoparticles

For the purpose of easy handling and ensuring high dispersion of the synthesized nanoparticles, Pd@Ag was loaded on the supports and the support effect was investigated (Table 2-1). However, Pd@Ag on various supports such as hydroxyapatite (HAP), TiO_2, hydrotalcite, and MgO, showed similar activities, indicating that the activity of Pd@Ag does not significantly depend on the supports. Then, HAP was selected as the support because it exhibited slightly higher efficiency among the tested supports.

Table 2-1. Support effect[a]

Hex $\equiv$ **1** $\xrightarrow[\text{EtOH (2 mL), H}_2 \text{ (balloon), r.t., 30 min}]{\substack{\text{Pd@Ag/Support} \\ \text{(Pd: 3.3 mol\%, Ag: 0.66 mol\%)}}}$ Hex $\diagdown$ **2** + Hex $\diagup$ **3**

Entry	Support	Conv. of **1** [%][b]	**2** [%][b]	**3** [%][b]
1	HAP	23	23	0
2	TiO_2	22	22	0
3	Hydrotalcite	21	21	0
4	MgO	14	14	0

[a]Reaction conditions: Catalyst (0.10 g, Pd: 3.3 mol%, Ag: 0.66 mol%), **1** (0.3 mmol), EtOH (2 ml). [b]Determined by GC using internal standard technique.

The Pd@Ag-X composites were used as catalysts in the batchwise semihydrogenation of 1-octyne (**1**) at room temperature under atmospheric pressure of H_2. In order to compare catalytic activity, both single Pd nanoparticles (Pd seed for Pd@Ag) and Ag nanoparticles loaded on HAP were prepared. The results are shown in Table 2-2. Pd nanoparticles promoted rapid overhydrogenation, quantitatively giving the undesired product *n*-octane (**3**) (Entry 1). Ag nanoparticles did not show any catalytic activity under the conditions used (Entry 2). As previously reported [36], highly alkene-selective catalysis of Ag nanoparticles was confirmed under high pressure of H_2 (50 atm), although with extremely low activity (turnover frequency = 0.035 h^{-1})

(Entry 3). In contrast, the various Pd@Ag-X composites showed differing activity and selectivity toward **2** depending on the value of X. When the Ag/Pd ratio X was increased from 0.10 to 0.20, alkene-selectivity steadily increased (Entries 4–6), with Pd@Ag-0.20 exhibiting the highest catalytic activity, affording **2** in quantitative yield (Entry 6). Upon a further increase in the Ag/Pd ratio to 0.50, complete alkene-selectivity was retained but the activity of the catalyst gradually decreased (Entries 8 and 9). Interestingly, the excellent alkene-selectivity of Pd@Ag-0.20 was maintained even when the reaction time was prolonged after full conversion of **1** (Figure 2-4). Notably, the C=C bond of **2** remained almost intact up to a H_2 pressure of 50 atm (Entry 7). This high performance of Pd@Ag-0.20 arising from the core-shell structure is in sharp contrast with many previous catalysts, including the Lindlar catalyst [17] (Figure 2-5) and Pd-Ag alloys (Figure 2-6) [45-55], which easily causes overhydrogenation of terminal alkenes to alkanes.

Table 2-2. Semihydrogenation of **1** using various Pd-Ag catalysts[a]

Hex ═══ **1** — Catalyst, H_2 (1 atm), r.t. → Hex ⌇ **2**   Hex ⌇ **3**

Entry	Catalyst	Time [h]	Conv. [%][b]	2 [%][b]	3 [%][b]
1	Pd nanoparticles	0.5	> 99	0	> 99
2[c]	Ag nanoparticles	2.5	0	-	-
3[d]	Ag nanoparticles	20	36	36	0
4	Pd@Ag-0.10	2.5	> 99	23	76
5	Pd@Ag-0.15	2.5	> 99	80	19
6	Pd@Ag-0.20	2.5	> 99	> 99	0
7[e]	Pd@Ag-0.20	1.0	> 99	> 99	0
8	Pd@Ag-0.25	2.5	65	65	0
9	Pd@Ag-0.50	2.5	22	22	0

[a]Reaction conditions: Catalyst (0.10 g, Pd: 3.3 mol%, Ag: 0.33 mol%-1.7 mol%), **1** (0.3 mmol), EtOH (2 ml). [b]Determined by GC using internal standard technique. [c]Ag/HAP (Ag: 0.33 mol%). [d]Ag/HAP (Ag: 50 mol%), H_2 (50 atm). [e]H_2 (50 atm).
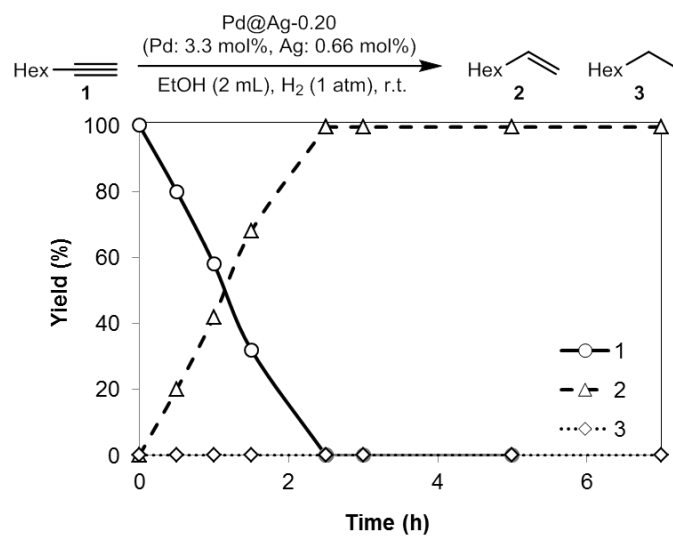
Figure 2-4. Time profile of semihydrogenation of **1** using Pd@Ag-0.20
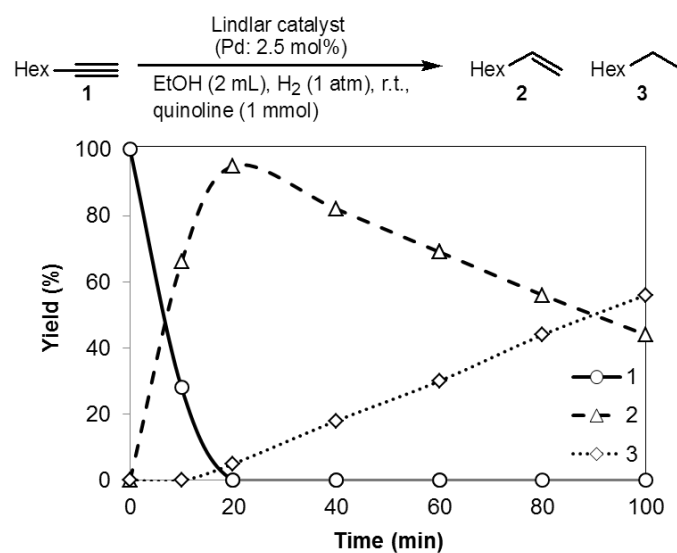
Figure 2-5. Time profile of semihydrogenation of **1** using Lindlar catalyst
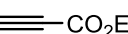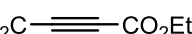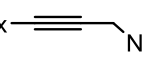
45
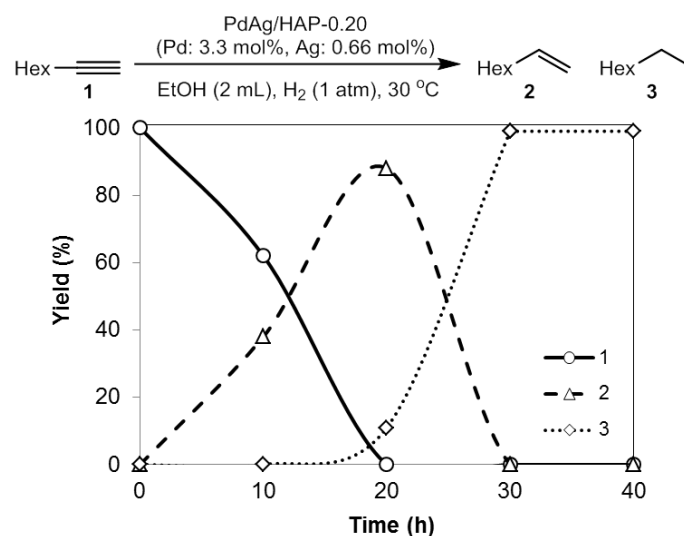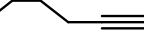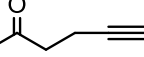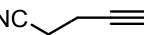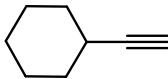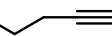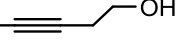
Figure 2-6. Time profile of semihydrogenation of **1** using PdAg/HAP-0.20

The catalytic potential of Pd@Ag-0.20, which exhibited the best performance, was investigated using various alkynes in a batch reactor (Table 2-3). A wide range of terminal and internal alkynes containing functional groups such as hydroxyl (Entries 3, 11, 12), halogen (Entry4), carboxylic acid (Entry 5), cyano (Entry 6), ester (Entries 13 and 14) and amine (Entry 15) groups were smoothly converted to the corresponding alkenes with >99% selectivity. After the reaction, the Pd@Ag catalyst loaded onto HAP was easily recovered by filtration, and proved to be reusable, retaining its high activity and selectivity during five recycling experiments (Table 2-3, Entry 2). No aggregations of the nanoparticles and significant change of the average diameter were observed in TEM image (Figure 2-7), demonstrating its high durability. The practical utility of Pd@Ag was also examined by using a column flow reactor for gram-scale synthesis. When **1** (10 mmol, 1.10 g) in ethanol (0.10 M) was passed through a Pd@Ag-0.20-packed column reactor at a flow rate of 4.2 mL h^{-1} along with H_2 at atmospheric pressure, **2** was successively obtained in over 99% yield (96% isolated yield; 1.07 g) (Scheme 2-1).

Figure 2-3. Semihydrogenation of various alkynes using Pd@Ag-0.20[a]

$$R \text{---}\!\!\equiv\!\!\text{---} R' \xrightarrow[\text{H}_2\ (1\ \text{atm), r. t.}]{\text{Pd@Ag-0.20}} \quad \underset{R}{\diagdown}\!\!=\!\!\underset{R'}{\diagup} \quad R\diagdown\!\!\diagup\!\!\diagdown R'$$

Entry	Alkyne	Time [h]	Conv. [%][b]	Yield [%][b]	E/Z ratio[b]
1	Hex—≡	2.5	> 99	> 99 (95)	-
2[c]		2.5	> 99	> 99	-
3	HO⌒⌒—≡	1.0	> 99	> 99 (93)	-
4	Cl⌒⌒⌒—≡	1.5	> 99	> 99 (91)	-
5	HO(C=O)⌒⌒—≡	3.0	> 99	> 99 (92)	-
6	NC⌒⌒—≡	3.0	> 99	> 99 (93)	-
7[d]	cyclohexyl—≡	14	> 99	> 99 (92)	-
8	Ph⌒—≡	3	> 99	> 99 (96)	-
9	Ph⌒⌒—≡	3	> 99	> 99 (95)	-
10	Pr—≡—Pr	4	> 99	> 99 (94)	0/100
11	Et—≡—⌒OH	5	> 99	> 99 (94)	0/100
12	Pr—≡—⌒OH	5.5	> 99	> 99 (94)	0/100
13	≡—CO$_2$Et	5	> 99	> 99 (91)	4/96
14[e]	EtO$_2$C—≡—CO$_2$Et	12	> 99	> 99 (92)	16/84
15	Hex—≡—⌒NEt$_2$	5	> 99	> 99 (93)	0/100

[a]Reaction conditions: Pd@Ag-0.20 (0.10 g, Pd: 0.33 mol%, Ag: 0.066 mol%), alkyne (0.3 mmol), EtOH (2 ml). [b]Determined by GC using internal standard technique. Values in parentheses are isolated yields. [c]5th reuse. [d]Hexane (2 mL). [e]50 °C.
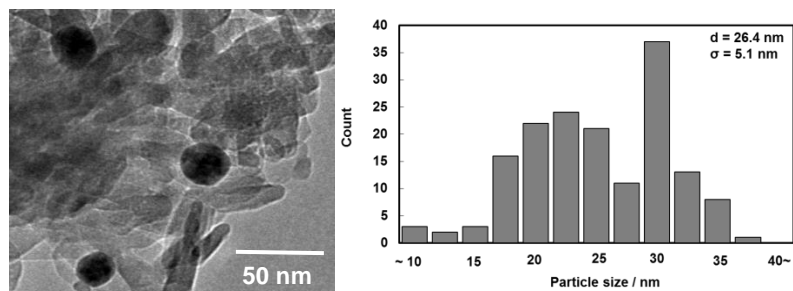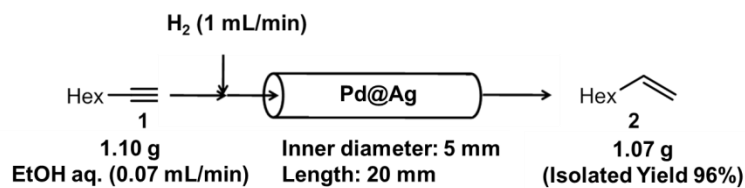

Figure 2-7. TEM image and size-distribution of used Pd@Ag-0.20 on HAP

Scheme 2-1. Application of Pd@Ag to the column flow reactor

To elucidate the reasons for the significant differences in the performance of Pd@Ag-X depending on X, the shell effect of Ag was investigated by CO adsorption FTIR spectroscopy (Figure 2-8). It is well known that CO is not adsorbed onto the Ag nanoparticle surface but is strongly adsorbed on Pd nanoparticles [56 and 57]. In fact, when single Ag nanoparticles and Pd nanoparticles were treated with CO, no CO adsorption peaks were observed for Ag nanoparticles, while two CO adsorption peaks derived from CO stretching at 1930 cm^{-1} and 2060 cm^{-1} were observed for Pd nanoparticles. IR spectra of Pd@Ag-0.10 and Pd@Ag-0.15 treated with CO showed two peaks in the same position as for single Pd nanoparticles. On the other hand, it is notable that Pd@Ag-0.20, Pd@Ag-0.25, and Pd@Ag-0.50 showed no CO adsorption peaks, demonstrating that the Pd nanoparticles were entirely covered by Ag in a core-shell structure. These results showed that the low alkene-selectivity of Pd@Ag-0.10 and Pd@Ag-0.15 was strongly associated with the presence of the exposed Pd nanoparticles, causing overhydrogenation. The steadily decreasing activity of Pd@Ag-X as X increased from 0.20 to 0.50 was explained by the increase in thickness of the Ag shell, which hinders the supply of hydrogen from the core-Pd nanoparticles to the surface Ag sites. TEM images of Pd@Ag supported the contention that the thickness of the Ag shell could be controlled by changing the amount of Ag used. The mean diameters of Pd@Ag-X, where X was 0.10, 0.15, 0.20, 0.25, and 0.50, were 25.2 ± 4.0, 25.9 ± 4.9, 26.2 ± 5.7, 26.6 ± 5.9, and 27.0 ± 4.5 (Figure 2-9).
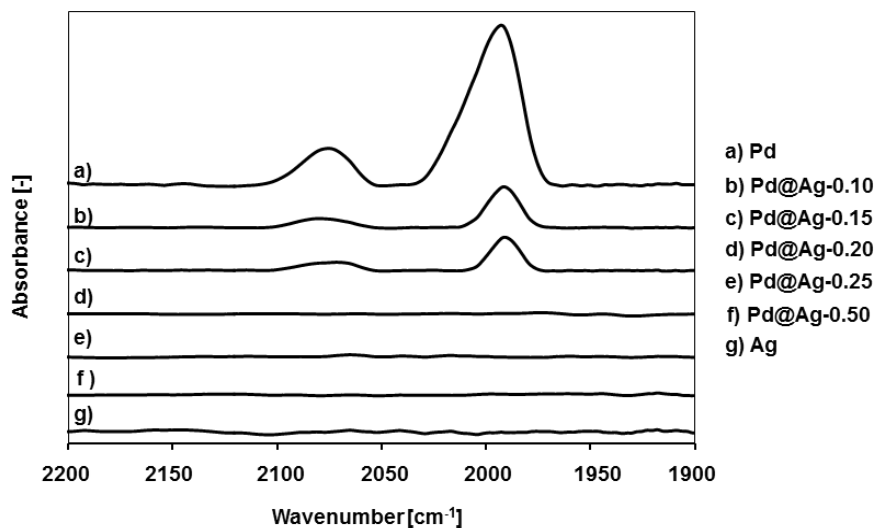
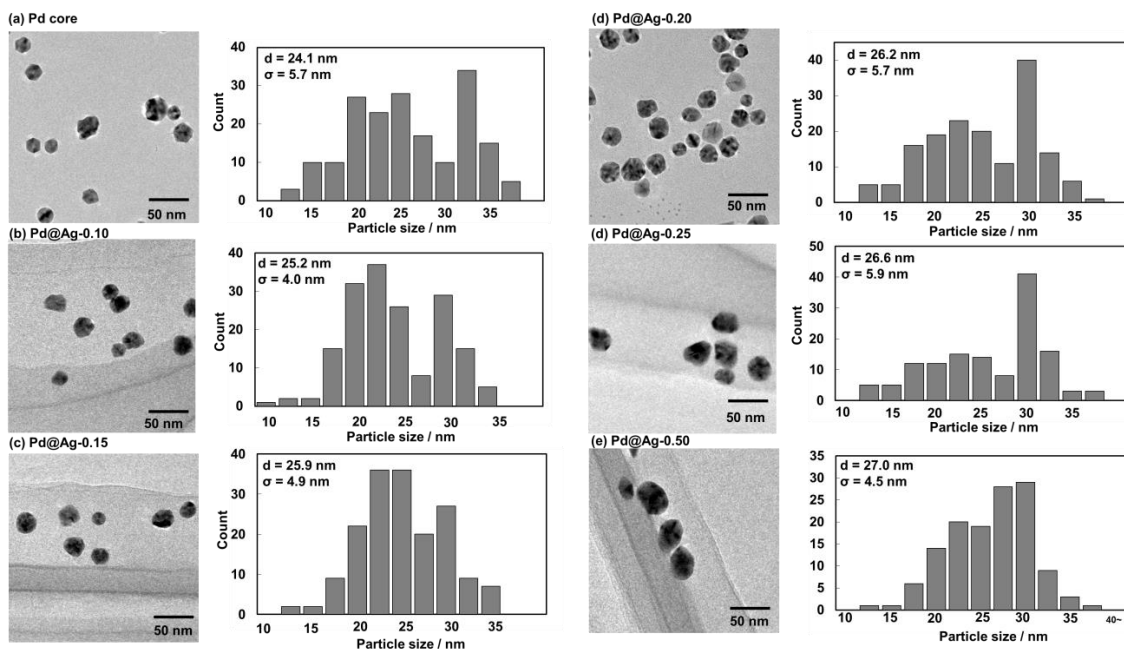**Figure 2-8**. FTIR spectra of Pd@Ag-X and single Pd and Ag nanoparticles treated with CO

Figure 2-9. TEM images and size-distributions of (a) Pd core, (b) Pd@Ag-0.10, (c) Pd@Ag-0.15, (d) Pd@Ag-0.20, (e) Pd@Ag-0.25, (f) Pd@Ag-0.50.

49

Among noble metals, Ag nanocrystals have uniquely bifunctional properties with not only the alkene-selective catalysis but also the high activity for surface-enhanced Raman spectroscopy (SERS), allowing in-situ monitoring of Ag-catalyzed surface reaction [58-61]. Therefore, Pd@Ag-catalyzed semihydrogenation was investigated using SERS. Figure 2-10-(A) shows SERS spectra from ethanol suspension of Pd nanoparticles and Pd@Ag in the presence of phenylacetylene (PA) as a Raman probe. No peaks of PA (0.12 mM) without nanoparticles or with Pd nanoparticles were confirmed (Figure 2-10-A, (a) and (b)). Interestingly, when the colloidal Pd@Ag was dropped into the ethanol solution of PA, new peaks at 1980 cm^{-1} (C≡C stretching mode) and 1590 cm^{-1} (benzene ring mode) appeared, demonstrating the SERS activity of Pd@Ag (Figure 2-10-A, (c)). The shift in the peak at 2111 cm^{-1} for the C≡C stretching of free PA to 1980 cm^{-1} is assigned to surface adsorption of PA on Ag (Figure 2-10-A, (c) vs. (d)), in agreement with previous finding [58]. Moreover, the SERS activity of Pd@Ag enabled the in-situ monitoring of the Pd@Ag-catalyzed semihydrogenation of PA. After adding Pd@Ag to the PA solution under atmospheric H$_2$ conditions, the SERS spectrum was recorded (Figure 2-10-B). The peaks attributed to the PA adsorbed on the surface of Ag gradually decreased during the semihydrogenation of PA, supporting that the semihydrogenation undergoes on the surface of Ag shell of Pd@Ag where the Pd core serves as a hydrogen source due to the formation of a PdH species. The formation of the PdH was confirmed by XRD analysis (Figure 2-11) where the XRD peaks attributed to Pd core of Pd@Ag shifted to low-angle side under H$_2$ atmosphere. This lattice expansion indicated that H atom entered into the Pd lattice and the formation of PdH occurred. Furthermore, the H$_2$-D$_2$ exchange experiment using Ag nanoparticles catalyst revealed the formation of HD (Scheme 2-2). This result supported the possibility for H$_2$-permeability of Ag shell where Ag nanoparticles cleave H-H bonds and the resulting H atoms pass through the Ag layer.
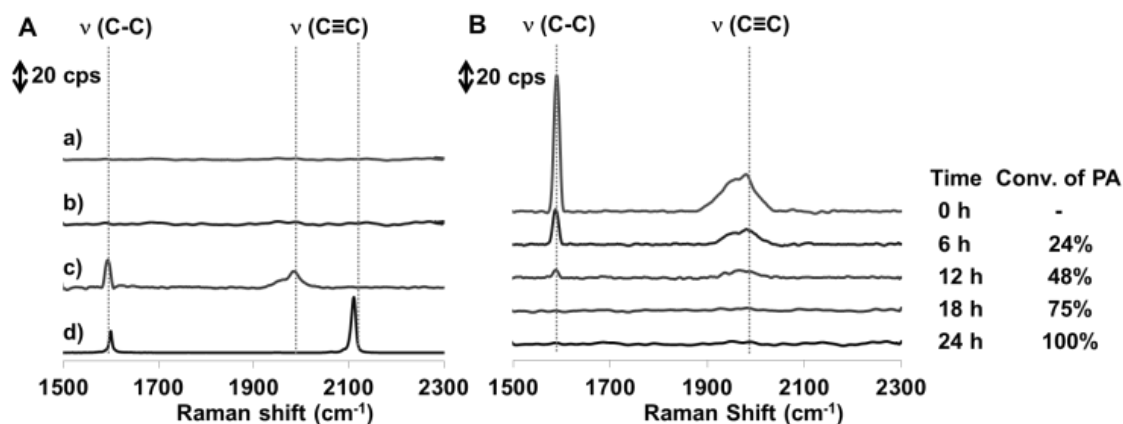
Figure 2-10. (A) Raman spectra recorded from ethanol suspension of nanoparticles in the presence of PA: a) 0.12 mM PA, b) 0.12 mM PA with Pd nanoparticles, c) 0.12 mM PA with Pd@Ag-0.20 and d) reference PA (intensity: 1/500). (B) SERS spectra recorded during the semihydrogenation of PA catalyzed by Pd@Ag-0.20 at r. t. under 1 atm of H_2.
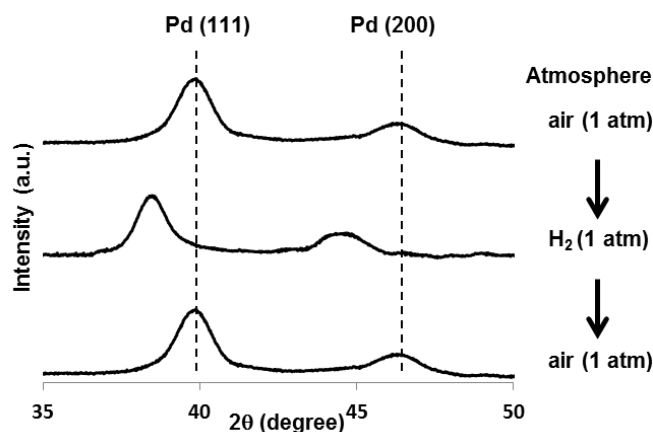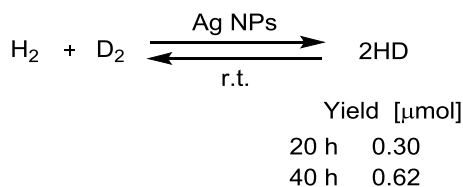

Figure 2-11. *In situ* XRD measurements of Pd@Ag-0.20

Scheme 2-2. H_2-D_2 exchange reaction using Ag nanoparticles

4. Conclusion

This chapter demonstrated the design of core-Pd/shell-Ag nanocomposite catalysts (Pd@Ag) whose components acted in complementary fashion to achieve Pb-free and highly selective semihydrogenation of alkynes under mild reaction conditions. The Pd@Ag catalyst was reusable and applicable to use in a column flow reactor. It was found that the core-Pd enhanced the activity of the shell-Ag by serving as a hydrogen source, while, at the same time, the shell Ag reduced the intrinsically low alkene-selectivity of Pd by inhibiting contact between Pd and alkenes. As a whole, the complementary relationship between Pd and Ag derived from the core-shell arrangement resulted in highly active and selective catalysis in the semihydrogenation of alkynes. This study reveals that precise synthesis of bimetal nanoparticles with core-shell nanostructures would realize unprecedentedly selective catalysis for the fine chemical synthesis.

5. References

[1] D. K. Lim, K.-S. Jeon, H. M. Kim, J.-M. Nam, Y. D. Suh, *Nat. Mater.* **2010**, *9*, 60-67.

[2] J. F. Li, Y. F. Huang, Y. Ding, Z. L. Yang, S. B. Li, X. S. Zhou, F. R. Fan, W. Zhang, Z. Y. Zhou, D. Y. Wu, B. Ren, Z. L. Wang, Z. Q. Tian, *Nature* **2010**, *464*, 392-395.

[3] H. Zhu, A. Sigdel, S. Zhang, D. Su, Z. Xi, Q. Li, S. Sun, *Angew. Chem. Int. Ed.* **2014**, *53*, 12508-12512.

[4] A. Rogach, A. Susha, F. Caruso, G. Sukhorukov, A. Kornowski, S. Kershaw, H. Möhwald, A. Eychmüller, H. Weller, *Adv. Mater.* **2000**, *12*, 333-337.

[5] J. Ge, H. Lee, L. He, J. Kim, Z. Lu, H. Kim, J. Goebl, S. Kwon, J. Yin, *J. Am. Chem. Soc*. **2009**, *131*, 15687-15694.

[6] A. Burns, H. Ow, U. Wiesner, *Chem. Soc. Rev.* **2006**, *35*, 1028-1042.

[7] A. M. Smith, A. M. Mohs, S. Nie, *Nat. Nanotechnol.* **2009**, *4*, 56-63.

[8] R. Makki, X. Ji, H. Mattoussi, O. Steinbock, *J. Am. Chem. Soc.* **2014**, *136*, 6463-6469.

[9] S. Alayoglu, A. U. Nilekar, M. Mavrikakis, B. Eichhorn, *Nat. Mater.* **2008**, *7*, 333-338.

[10] T. Mitsudome, Y. Mikami, M. Matoba, T. Mizugaki, K. Jitsukawa, K. Kiyotomi, *Angew. Chem. Int. Ed.* **2012**, *51*, 136-139.

[11] Y. Yang, X. Liu, X. Li, J. Zhao, S. Bai, J. Liu, Q. Yang, *Angew. Chem. Int. Ed.* **2012**, *51*, 9164-9168.

[12] C.-H. Jun, Y. J. Park, Y.-R. Yeon, J. R. Choi, W.-R. Lee, S.-J. Ko, J. Cheon, *Chem. Commun.* **2006**, 1619-1621.

[13] H. Yang, Y. Chong, X. Li, H. Ge, W. Fan, J. Wang, *J. Mater. Chem.* **2012**, *22*, 9069-9076.

[14] T. Mitsudome, Y. Takahashi, S. Ichikawa, T. Mizugaki, K. Jitsukawa, K. Kaneda, *Angew. Chem. Int. Ed.* **2013**, *52*, 1481-1485.

[15] M. L. Derrien, *Stud. Surf. Sci. Catal.* **1986**, *27*, 613-640.

[16] *Plastic Packaging: Interactions with Food and Pharmaceuticals* (Eds: O. G. Piringer, A. L. Baner), Wiley, New Jersey, **2008**, 32-46.

[17] H. Lindlar, R. Dubuis, *Org. Synth. Coll.* **1973**, *5*, 880-882.

[18] M. Gruttadauria, R. Natto, G. Deganello, L. F. Liotta, *Tetrahedron Lett.* **1999**, *40*, 2857-2858.

[19] H. Sajiki, S. Mori, T. Ohkubo, T. Ikawa, A. Kume, T. Maegawa, Y. Monguchi, *Chem. Eur. J.* **2008**, *14*, 5109-5111.

[20] J. Hori, K. Murata, T. Sugai, H. Shinohara, R. Noyori, N. Arai, N. Kurono, T. Ohkuma, *Adv. Synth. Catal.* **2009**, *351*, 3143-3149.

[21] Y. Takahashi, N. Hashimoto, T. Hara, S. Shimazu, T. Mitsudome, T. Mizugaki, K. Jitsukawa, K. Kaneda, *Chem. Lett.* **2011**, *40*, 405-407.

[22] C. W. A. Chan, Y. Xie, N. Cailuo, K. M. K. Yu, J. Cookson, P. Bishop, S. C. Tsang, *Chem. Commun.* **2011**, *47*, 7971-7973.

[23] Y. Yabe, T. Yamada, S. Nagata, Y. Sawara, Y. Monguchi, H. Sajiki, *Adv. Synth. Catal.* **2012**, *354*, 1264-1268.

[24] Y. Lee, Y. Motoyama, K. Tsuji, S.-H. Yoon, I. Mochiba, H. Nagashima, *ChemCatChem* **2012**, *4*, 778-781.

[25] Y. Yabe, Y. Sawama, Y. Monguchi, H. Sajiki, *Catal. Sci. Technol*. **2014**, *4*, 260-271.

[26] E. D. Slack, C. M. Gabriel, B. H. Lipshutz, *Angew. Chem. Int. Ed*. **2014**, *53*, 14051-14054.

[27] F. Alonso, I. Osante, M. Yus, *Adv. Synth. Catal.* **2006**, *348*, 305-308.

[28] F. Alonso, I. Osante, M. Yus, *Tetrahedron* **2007**, *63*, 93-102.

[29] K. Semba, T. Fujihara, T. Xu, J. Terao, Y. Tsuji, *Adv*. *Synth*. *Catal*. **2012**, *354*, 1542-1550.

[30] M. Niu, Y. Wang, W. Li, J. Jiang, Z. Jin, *Catal*. *Commun*. **2013**, *38*, 77-81.

[31] L. Shao, X. Huang, D. Teschner, W. Zhang, *ACS Catal*. **2014**, *4*, 2369-2373.

[32] G. Li, R. Jin, *J. Am. Chem. Soc*. **2014**, *136*, 11347-11354.

[33] E. Vasilikogiannaki, I. Titilas, G. Vassilikogiannakis, M. Stratakis, *Chem. Commun*. **2015**, *51*, 2384-2387.

[34] T. Mitsudome, M. Yamamoto, Z. Maeno, T. Mizugaki, K. Jitsukawa, K. Kaneda, *J. Am. Chem. Soc.* **2015**, *137*, 13452-11354.

[35] A. Sárkány, Zs. Révay, *Appl. Catal. A: Gen.* **2003**, *243*, 347-355.

[36] G. Vilé, D. Baudouin, I. N. Remediakis, C. Copèret, N. Lòpez, J. Pèrez-Ramìrez, *ChemCatChem* **2013**, *5*, 3750-3759.

[37] E. Oakton, G. Vilé, D. S. Levine, E. Zocher, D. Baudouin, J. Pèrez-Ramìrez, C. Copèret, *Dalton Trans.* **2014**, *43*, 15138-15142.

[38] *Hydrogen in Metals II* (Eds.: G. Alefeld, J. Völkl), Springer-Verlag, Berlin, **1978**, 73-155.

[39] K. Christmann, *Surf. Sci. Rep.* **1988**, *9*, 8-10.

[40] M. Yamauchi, H. Kobayashi, H. Kitagawa, *ChemPhysChem* **2009**, *10*, 2566-2576.

[41] H. Katsuta, R. B. McLellan, *Scripta Metallurgica* **1979**, *13*, 65-66.

[42] I.-M. Chou, *Am. J. Sci.* **1986**, *286*, 638-658.

[43] Y. Aoki, L. Shi, T. Sugimoto, H. Hirayama, *Surface Science* **2010**, *604*, 420-423.

[44] T. Mitsudome, S. Arita, H. Mori, T. Mizugaki, K. Jitsukawa, K. Kaneda, *Angew. Chem. Int. Ed.* **2008**, *47*, 7438-7440.

[45] M. M. Johnson, D. W. Walker, G. P. Nowack, (Phillips Petroleum Company), US 4404124, **1983**.

[46] Q. Zhang, J. Li, X. Liu, Q. Zhu, *Appl. Catal. A: Gen.* **2000**, *197*, 221-228.

[47] R. N. Lamb, B. Ngamson, D. L. Trimm, B. Gong, P. L. Silveston, P. Praserthdam, *Appl. Catal. A: Gen.* **2004**, *268*, 43-50.

[48] H. Zea, K. Lester, A. K. Datye, E. Rightor, R. Gulotty, W. Waterman, M. Smith, *Appl. Catal. A: Gen.* **2005**, *282*, 237-245.

[49] W. Huang, W. Pyrz, R. F. Lobo, J. G. Chen, *Appl. Catal. A: Gen.* **2007**, *333*, 254-263.

[50] A. A. Lamberov, S. R. Il'yasov, Kh. Gil'manov, S. V. Trifonov, V. M. Shatilov, A. Sh. Ziyatdinov, *Kinet. Catal.* **2007**, *48*, 136-142.

[51] I. Y. Ahn, J. H. Lee, S. K. Kim, S. H. Moon, *Appl. Catal. A: Gen.* **2009**, *360*, 38-42.

[52] J. H. Lee, S. K. Kim, I. Y. Ahn, W.-J. Kim, S. H. Moon, *Catal. Commun.* **2011**, *12*, 1251-1254.

[53] A. Pachulski, R. Schödel, P. Claus, *Appl. Catal. A: Gen.* **2011**, *400*, 14-24.

[54] Y. Zhang, W. Diao, C. T, Williams, J. R. Monnier, *Appl. Catal. A: Gen.* **2014**, *469*, 419-426.

[55] G. X. Pei, X. Y. Liu, A. Wang, A. F. Lee, M. A. Isaacs, L. Li, X. Pan, X. Yang, X. Wang, Z. Tai, K. Wilson, T. Zhang, *ACS Catal.* **2015**, *5*, 3717-3725.

[56] D. Cormack, J. Pritchard, R. L. Moss, *J. Catal.* **1975**, *37*, 548-552.

[57] Y. Han, D. Peng, Z. Xu, H. Wan, S. Zheng, D. Zhu, *Chem. Commun.* **2013**, *49*, 8350-8352.

[58] T. W. Lee, K. Kim, M. S. Kim, *J. Mol. Struct.* **1992**, *274*, 59-73.

[59] E. Lee, S. S. Yi, M. S. Kim, K. Kim, *J. Mol. Struct.* **1993**, *298*, 47-54.

[60] K. Kim, D. Shin, J.-Y. Choi, K. L. Kim, K. S. Shin, *J. Phys. Chem. C* **2011**, *115*, 24960-24966.

[61] J. Du, J. Cui, C. Jing, *Chem. Commun.* **2014**, *50*, 347-349.

Chapter III.

Green One-step Synthesis of Core-Shell Nanoparticle and Their Catalysis for Chemoselective Hydrogenations

1. Introduction

The development of novel synthetic techniques of nanomaterials such as metal nanoparticles [1, 2], zeolites [3, 4], metal organic frameworks [5, 6] and carbon nanotubes [7, 8] with unique morphology have become an important research area along with advance of analytical methods on an atomic scale. These newly synthesized nanomaterials are widely applied in the various fields, for example, electronics [9], medicals [10, 11] and biotechnologies [12]. Among these nanomaterials, precisely structure-controlled metal nanoparticles, especially core-shell structured nanoparticles, have gathered attention as promising research targets due to their multi-functionality and enhanced properties that cannot be obtained from their mono-metal counterparts [13-19]. To date, various core-shell nanoparticles have been synthesized by using the established techniques such as the seeded-growth method [20-23], galvanic replacement method [24-27], and decomposition method [28-30]. Murray *et al*. prepared Ni@FePt core-shell nanoparticles through the seeded-growth method [22]. In the presence of preformed Ni cores (4.2 nm), Pt and Fe precursors were reduced using oleylamine as the stabilizer and reductant, forming 0.8 nm of FePt thinlayer on Ni cores uniformly. Cheon *et al*. applied the galvanic replacement method to synthesis Co@M (M = Au, Pd, Pt and Cu) core-shell nanoparticles [24]. When Co nanoparticles were treated with shell metal precursors, the redox-transmetalation reactions between Co and shell precursors occurred on the Co surface and surface Co atoms were replaced by shell metal atoms, yielding core-shell nanoparticles precisely. These above-mentioned methods are quite useful for the precise synthesis of the core-shell nanoparticles. However, they are generally complicated, and often require time-consuming and multiple steps with harmful and expensive reagents such as surfactants, reductants, and organic solvents, thus resulting in the production of large amounts of waste, the consumption of the energy and limiting the wide applicability of the core-shell nanoparticles. Furthermore, the presence of un-removed surfactants often declines their intriguing properties.

58

Especially, in the catalytic field, the residue surfactants would decrease the activity of the core-shell nanoparticles by blocking active metal sites. Therefore, the development of a facile and clean synthesis of core-shell nanoparticles has been highly desired and still a challenging issue.

Redox-coprecipitation method is attractive and promising for the facile synthesis of core-shell nanoparticles, where the redox reaction between core and shell metal precursors spontaneously occurs in the presence of bases, yielding core-shell nanoparticles in one step without any reductants (Figure 3-1, a) [31-38]. However, the redox-coprecipitation method generally yields large core-shell nanoparticles (> 100 nm) unsuitable for catalytic applications due to their low surface area to volume ratio and toxic bases such as NaOH are essentially required. For example, Kayama *et al*. synthesized CeO_2-covered Ag nanoparticles through the redox-coprecipitation using ammonia as an additional base [31]. The synthesized nanoparticles had a diameter of ca. 150 nm and consisted of 28 nm of Ag nanoparticles and 14 nm of CeO_2 nanoparticles. Zhao *et al.* demonstrated the one-step redox synthesis of $Au@TiO_2$ and $Pt@TiO_2$ [34]. However, the sizes ofthese nanoparticles also became so large (ca. 200 nm).
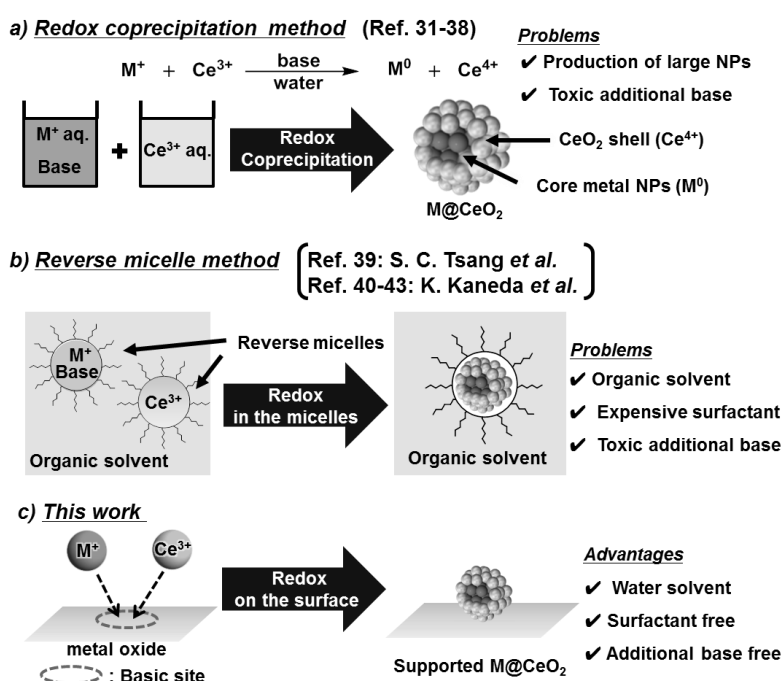

Figure 3-1. Comparison of the synthetic methods of core-shell nanoparticles

Recently, a new method using the combination of the reverse micelle technique with redox-coprecipitation was reported to synthesize small core-shell nanoparticles (Figure 3-1, b) [39-43]. In this strategy, the redox reaction between core and shell metal precursors proceeds in nanoscale aqueous phase inside the reverse micelles, producing small core-shell nanoparticles with a mean diameter of less than 10 nm in the core. Tsang *et al.* revealed that when using cetyltrimethylammonum bromide (CTAB) as the surfactant, small Pt@CeO$_2$ nanoparticles which possessed ca. 2 nm Pt nanoparticles in the core were obtained [39]. Kaneda *et al.* synthesized CeO$_2$-covered 10 nm of Ag [40-42] and 8.6 nm of Au [43] nanoparticles with the reverse micelle technique. However, the unavoidable use of surfactants, organic solvents, and additional bases is still costly and environmentally problematic.

Toward a more effective synthesis of core-shell nanoparticles, an alternatively new and green route for the synthesis of small core-shell nanoparticles without any organic reagents under neutral conditions is developed. Namely, simply mixing core and shell metal precursors in the presence of metal oxides with basicity in water enables the one-step fabrication of small core-shell nanoparticles without the requirement of the reductants, surfactants, organic solvents or additional toxic bases that are essential in existing methods (Figure 3-1, c). In this method, the basic site on the metal oxides acts as a nanoscale reaction place to promote the redox reaction between core and shell precursors, efficiently affording core-shell nanoparticles highly dispersed on the solid surface with suppressing the agglomeration of the core-shell nanoparticles. The sizes of core-shell nanoparticles are small and suitable for the catalytic application because the *in-situ* generated core-shell nanoparticles are immediately immobilized on the metal oxides without overgrowth of metal nanoparticles. Furthermore, the metal oxide-supported core-shell nanoparticles can be obtained by simple filtration and the conventional calcination process for removing the residual surfactants is not necessity. The obtained metal oxide-supported core-shell nanoparticles are also easily handled as

heterogeneous catalysts.

This chapter demonstrates the facile one-step synthesis of small CeO_2-covered Au and Ag core-shell nanoparticle catalysts through the redox-coprecipitation method using basic materials. This is the first success of a green one-step synthesis of small core-shell nanoparticles in water under organic reagent-free and neutral conditions. Furthermore, the synthesized HT-supported CeO_2-covered Au catalyst (Au@CeO_2/HT) promoted chemoselective hydrogenation of unsaturated aldehydes, epoxides and alkynes while retaining C=C bonds.

2. Experimental section

2-1. General

$HAuCl_4 \cdot xH_2O$ was obtained from Mitsuwa Chemicals. $AgNO_3$ and $Ce(NO_3)_3$ were purchased from Wako Pure Chemical Co., Ltd. MgO (JRC-MGO-3) was obtained from the Catalysis Society of Japan as a reference catalyst. Hydrotalcite, silica, and laponite were purchased from Tomita Pharmaceutical Co., Fuji Silysia and BYK Additives & Instruments, respectively. GC-FID and GC-MS were performed on a Shimadzu GC-2014 instrument equipped with a Unisole 30T column and a GCMS-QP2010 SE instrument equipped with an Inert Cap WAX-HT capillary column (30 m × 0.25 mm i.d., 0.25 μm). Transmission electron microscopy (TEM) images were obtained using an FEI Tecnai G2 20ST instrument operating at 200 kV. HAADF-STEM observations were carried out using a JEOL JEM-2800 High Throughput Electron Microscope, which was equipped with an energy dispersive X-ray spectroscopy (EDS) detector. IR spectra were collected on a JASCO FT-IR 410 spectrometer equipped with a MCT detector. [1]H and ^{13}C nuclear magnetic resonance (NMR) spectra were recorded on a JEOL JNM-ESC400 spectrometer, and the chemical shifts are reported in ppm from TMS as a reference.

2-2. Preparation of catalysts

Au@CeO₂/HT (HT: Tomita Pharmaceutical Co., Ltd. AD 500NS): HT (0.5 g) was soaked in 50 mL of deionized water. To the obtained HT suspension, 50 mL of a mixture of cerium nitrate (0.80 mmol) and chloroauric acid (0.05 mmol) was added dropwise at 15 °C. The resulting mixture was stirred at 15 °C for 1 h in an air atmosphere. The obtained slurry was filtered, washed with deionized water, and then dried at room temperature *in vacuo*.

Au@CeO₂/HT prepared in a large scale: HT (100 g) was soaked in 10 L of deionized water. Under stirring vigorously, 10 L of a mixture of cerium nitrate (160 mmol) and chloroauric acid (10 mmol) was added dropwise (0.1 L/h) to the HT suspension at 15 °C. The obtained slurry was filtered, washed with deionized water, and then dried at room temperature *in vacuo*.

Ag@CeO₂/HT (HT: Tomita Pharmaceutical Co., Ltd. AD 500NS): HT (0.5 g) was soaked in 50 mL of deionized water. To the obtained HT suspension, 50 mL of a mixture of cerium nitrate (0.40 mmol) and silver nitrate (0.05 mmol) was added dropwise at 45 °C. The resulting mixture was stirred at 45 °C for 4 h in an air atmosphere. The obtained slurry was filtered, washed with deionized water, and then dried at room temperature *in vacuo*.

Au@CeO₂/MgO (MgO: JRC-MGO-3): MgO (0.5 g) was soaked in 50 mL of deionized water. To the obtained MgO suspension, 50 mL of a mixture of cerium nitrate (0.80 mmol) and chloroauric acid (0.05 mmol) was added dropwise at 15 °C. The resulting mixture was stirred at 15 °C for 1 h in an air atmosphere. The obtained slurry was filtered, washed with deionized water, and then dried at room temperature *in vacuo*.

Au@CeO₂/Laponite (Laponite: BYK Additives & Instruments Laponite-RD): Laponite (0.5 g) was soaked in 50 mL of deionized water. To the obtained colorless solution, 50 mL of a mixture of cerium nitrate (0.80 mmol) and chloroauric acid (0.05 mmol) was added dropwise at 45 °C. The resulting mixture was stirred at 45 °C for 1 h in an air atmosphere. The obtained catalyst was

collected by centrifugation, washed with deionized water, and dried at room temperature *in vacuo*.

Amine-functionalized silica (silica: Fuji Silysia CARIACT Q-3): Silica (4.0 g) was soaked in 10 mL of toluene. To the obtained suspension, 4.0 g of 3-(2-aminoethylamino)propyltrimethoxysilane was added and the resulting mixture was stirred at 120 °C for 10 h. The obtained slurry was filtered, washed with EtOH, and then dried at room temperature *in vacuo*.

Au@CeO$_2$/Amine-functionalized silica: Amine-functionalized silica (0.5 g) was soaked in 50 mL of deionized water. To the obtained colorless solution, 50 mL of a mixture of cerium nitrate (0.80 mmol) and chloroauric acid (0.05 mmol) was added dropwise at 45 °C. The resulting mixture was stirred at 45 °C for 1 h in an air atmosphere. The obtained slurry was filtered, washed with deionized water, and then dried at room temperature *in vacuo*.

Au/HT or Au/CeO$_2$: HT or CeO$_2$ (1.0 g) was soaked in 50 mL of an aqueous solution of HAuCl$_4$ (2 mM). After stirring for 2 min, 0.2 mL of aqueous NH$_3$ (10%) was added and the resulting mixture was stirred at room temperature for 12 h in an air atmosphere. The obtained slurry was filtered, washed with deionized water, and then dried at room temperature *in vacuo*. Subsequently, the obtained yellow powder was added to 50 mL of an aqueous solution of KBH$_4$ (18 mM) and stirred at room temperature for 1 h to yield the supported gold nanoparticle catalyst as a purplish red powder.

2-3. Typical reaction procedure

A typical reaction procedure for hydrogenation of **1** to **2** using Au@CeO$_2$/HT is as follows. Au@CeO$_2$/HT (0.05 g, Au: 0.0042 mmol) was placed in a 50-mL stainless steel autoclave (with a Teflon inner cylinder) followed by addition of toluene (4 mL) and **1** (0.3 mmol). The reaction mixture was stirred vigorously at 120 °C under 30 atm of H$_2$. After the reaction, Au@CeO$_2$/HT was filtered and the yield was determined by GC analysis.

2-4. FT-IR study

Self-supporting pellets were prepared from Au@CeO$_2$/HT powders and treated directly in

the IR cell. Au@CeO$_2$/HT was evacuated at 423 K for 1 h, and then treated under 50 mmHg of H$_2$ or D$_2$ at 393 K. After the treatment, IR spectra were recorded at 300 K.

2-5. Product identification

The products were characterized by GC, GC-MS, and NMR. Retention times (GC) and chemical shifts (^{1}H and ^{13}C NMR) of the products were in agreement with those of authentic samples or previously reported values.

3. Results and Discussion

First, Au, Ce and hydrotalcite (HT: Mg$_6$Al$_2$(CO$_3$)(OH)$_{16}$·4(H$_2$O)) was chosen as core, shell precursors and the inorganic base material, respectively for the synthesis of core-shell nanoparticles. To the aqueous suspension of HT, a mixture of an aqueous solution of cerium nitrate and chloroauric acid was added dropwise. Interestingly, the color of the suspension became dark gray during the stirring of the resulting mixture at 15 °C for 1 h in air, indicating that the redox reaction between Au(III) and Ce(III) to Au(0) and Ce(IV) occurred on HT. The obtained slurry was filtered, washed
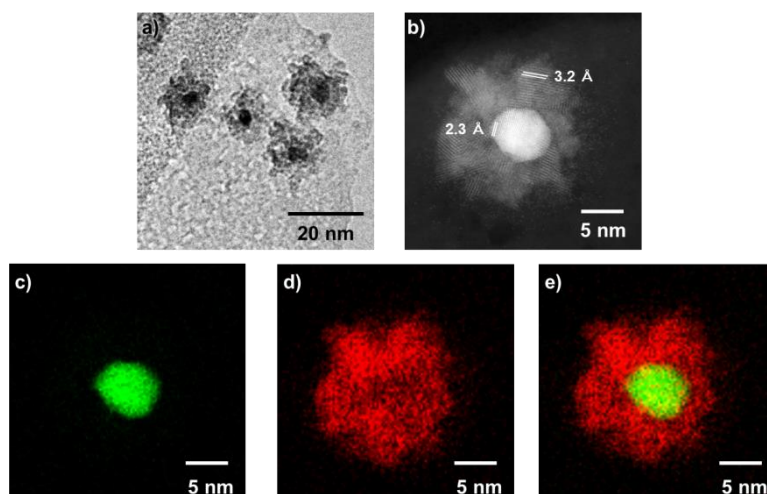
Figure 3-2. Composition and structural analysis of Au@CeO$_2$/HT. a) TEM image. b) HAADF-STEM image. Elemental mapping images of c) Au and d) Ce. e) Composite overlay image formed from c) and d).

with deionized water, and then dried at room temperature *in vacuo*, yielding the HT containing Au and Ce as gray powder.

The obtained powder was characterized using transmission electron microscopy (TEM). The TEM image showed that size-ordered nanoparticles with diameters of 10 nm were highly dispersed on HT (Figure 3-2, a). The nanoparticle consisted of an electron-dense core area and electron-lucent shell area, revealing the formation of core-shell nanoparticles. A HAADF-STEM image showed spherical core nanoparticles with a mean diameter of 5 nm and the shell with a thickness of around 4 nm (Figure 3-2, b). The lattice fringes of the core and shell nanoparticles had the d-spacing attributed to Au {111} (2.3 Å) and CeO_2 {111} (3.2 Å), respectively. Energy-dispersive X-ray spectroscopy mapping clearly proved that the core-shell nanoparticles were comprised of Au nanoparticles in the core and CeO_2 in the shell (Figure 3-2, c-e). To the best of our knowledge, this is the first success of a green one-step synthesis of small core-shell nanoparticles in water without the use of surfactants, organic solvents, reductants, or toxic bases. This method is quite different from those previously reported for the core-shell nanoparticles in the viewpoints of organic reagents-free and neutral conditions. The CeO_2-covered Au nanoparticles immobilized on HT is denoted as Au@CeO_2/HT.

It should be noted that this simple preparation of Au@CeO_2 was easily scalable; 100 g of Au@CeO_2/HT was successfully synthesized in one-step where the morphology of Au@CeO_2 on HT did not significantly change (Figure 3-3, a), demonstrating the utility of this method. The present method also allowed the use of various metal oxides with basicity in the synthesis of Au@CeO_2. For example, MgO (Figure 3-3, b), synthetic layered silicate (Figure 3-3, c), and amine-functionalized silica (Figure 3-3, d) were applicable to form Au@CeO_2 on the surface. In contrast, Au@CeO_2 was not formed using non-basic materials such as silica, carbon, and alumina, confirming the necessity of surface basic sites to promote the redox reaction between Au and Ce. Moreover, this method was

adapted to the fabrication of core-shell Ag nanoparticles of Ag@CeO$_2$/HT, in which core Ag nanoparticles with a mean diameter of 15 nm were coated with the shell CeO$_2$ to a thickness of 10 nm (Figure 3-3, h).

The dependence of the morphology of Au@CeO$_2$/HT on the preparation temperature was also investigated (Figure 3-3, e-g). The redox reaction between Au(III) and Ce(III) did not proceed at 0 °C. Upon increasing the temperature to 15, 30, and 45 °C, the core-shell structures of Au@CeO$_2$ were observed and the mean diameters of Au nanoparticles in the core increased to 5, 10, and 20 nm, respectively. The core-shell structure was not formed at 60 °C and bare Au nanoparticles were observed. These results revealed that the present method allowed the size-controllable synthesis of core-shell nanoparticles by changing the preparation temperature.
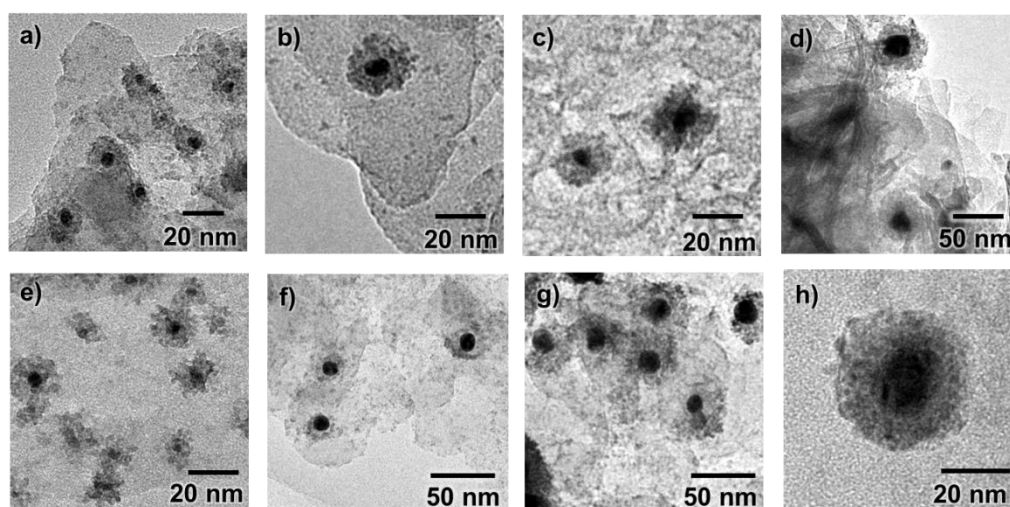
Figure 3-3. TEM images of a) Au@CeO$_2$/HT prepared on a 100 g scale. Au@CeO$_2$ supported on b) MgO, c) synthetic layered silicate (laponite), and d) amine-functionalized silica. Au@CeO$_2$/HT prepared at e) 15 °C, f) 30 °C, and g) 45 °C. h) Ag@CeO$_2$/HT.
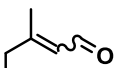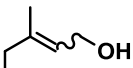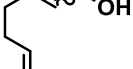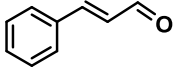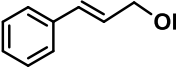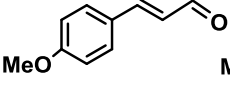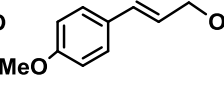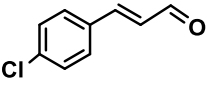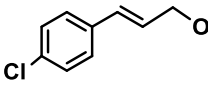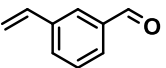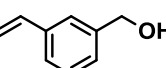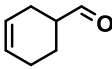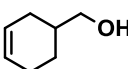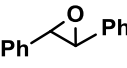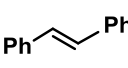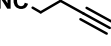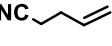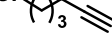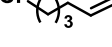
The catalytic potential of the Au@CeO$_2$/HT was investigated in the chemoselective reductions of various target functional groups in the presence of C=C bonds using molecular hydrogen (H$_2$). Chemoselective reduction of functional groups with retaining reducible C=C bonds are widely used for the synthesis of valuable chemical compounds such as pharmaceutical, natural products and agrichemicals [44-46]. Conventionally, these reductions were performed with stoichiometric reductants, for example, sodium borohydride, lithium borohydride and lithium aluminum hydride, where the reductants generated the polar hydrogen species and reduced polar functional groups selectively while non-polar C=C bonds were intact [47]. However, these stoichiometric reagents would produce the large amount of hazardous wastes. From the standpoint of Green Chemistry, catalytic procedures are superior to stoichiometric reagents. In this context, various catalytic systems using metal-free reductants such as alcohols, formic acid and hydrosilanes are developed for the chemoselective reduction reactions [48]. Generally, these systems shows high activity and selectivity for target reactions, but still suffer from byproduction of wastes originated from reductants, causing low atom efficiency. To realize the greener processes, H$_2$ is an ideal reductant due to the formation of water as the sole byproduct. However, chemoselective reductions using H$_2$ are more difficult compared with the case of other reductants because of easily promoting undesired hydrogenation of C=C bonds. Therefore, the development of the efficient catalytic systems for chemoselective hydrogenation with retaining C=C bonds using H$_2$ is highly desired and still challenging issue.

Au nanoparticle catalysts have attracted attention due to their high chemoselectivity for the hydrogenation of polar functional groups using H$_2$ [46, 49-61]. For example, van Leeuwen *et al.* revealed that Au nanoparticles ligated by phosphine oxides promoted highly chemoselective hydrogenation of aldehydes including alkynl, alkenyl, aldehyde, cyano, carboxylic acid, and ether groups, demonstrating Au nanoparticles intrinsically show high chemoselectivity [54]. However, Au

catalyst systems still suffer from limited substrate scope [49-50] and the requirement of harmful additives [55, 56, 58, 61]. Therefore, the chemoselective reductions of various functional groups catalyzed by Au nanoparticles using H_2 as a green reductant under additive-free conditions are still challenging issues.

Interestingly, Au@CeO$_2$/HT prepared at 15 °C showed high chemoselectivity for the unsaturated aldehyde, citral (**1**), giving nerol and geraniol (**2**) in quantitative yield with the C=C bonds remaining completely intact during the reduction (Table 3-1, Entry 1). Au@CeO$_2$/HT with larger Au nanoparticles prepared at 30 °C and 45 °C also promoted the selective hydrogenation of **1**, but they were considerably less active than that prepared at 15 °C (Entry 1 vs. 3 and 4), revealing that small Au nanoparticles that are sub-10 nm in diameter are more effective as a catalyst. In control experiments, bare Au nanoparticles (without core-shell structure) supported on CeO$_2$ and HT were prepared and tested in the hydrogenation of **1**. However, these catalysts hydrogenated the C=C bond of **1**, resulting in low selectivity for **2** (Scheme 3-1). This sharp contrast in the catalytic performance of Au nanoparticles with or without core-shell structure disclosed that the core-shell structure is the key for promoting highly selective hydrogenation. Note that Au@CeO$_2$/HT prepared at 15 °C showed the highest catalytic performance (all catalytic activity, product yield and selectivity) amongthose of previously reported Au-based catalysts (Table 3-2). Furthermore, Au@CeO$_2$/HT was able to catalyze versatile chemoselective hydrogenations while retaining C=C bonds under additive-free conditions, such as the hydrogenation of other unsaturated aldehydes (Entries 5-9), deoxygenation of epoxides (Entries 10-13), and semihydrogenation of alkynes (Entries 14-18). The selectivity for the desired products was significantly high (>99%) at high conversion levels in all these hydrogenations and the perfect regioselectivity for the *Z*-alkene was obtained in semihydrogenation of the internal alkyne (Entry 14).

Table 3-1. Chemoselective hydrogenation using Au@CeO$_2$/HT[a]

Entry	Substrate	Product	Time (h)	Yield (%)[b]	Sel. (%)[b]
1			40	>99	>99
2[c]				>99	>99
3[d]				34	>99
4[e]	(E/Z = 61/39)	(E/Z = 61/39)		4	>99
5			25	>99	>99
6[f]			40	>99	>99
7			35	>99	>99
8			30	>99	>99
9			30	97	>99
10			35	>99	>99
11			30	>99	>99
12			35	>99	>99
13[f]			10	98	>99
14	Bu—≡—Bu		40	>99	>99
15	Hex—≡		35	97	>99
16[f]	Ph—≡		35	>99	>99
17			30	>99	>99
18			25	>99	>99

[a]Reaction conditions: Au@CeO$_2$/HT (0.05 g, Au: 0.005 mmol), substrate (0.3 mmol), toluene (4 mL), H$_2$ (30 atm), 120 °C. [b]Determined by GC using an internal standard technique. [c]Reuse. [d]Prepared at 30 °C. [e]Prepared at 45 °C. [f]100 °C.
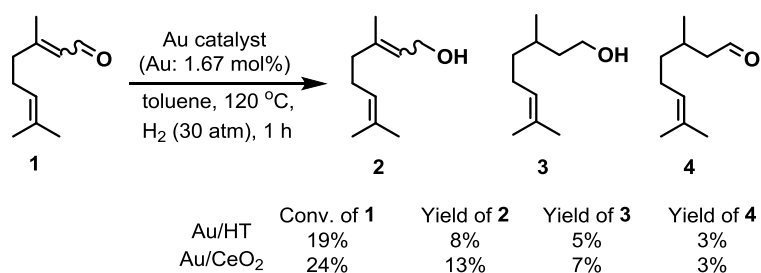
Scheme 3-1. Hydrogenation of **1** using conventional supported Au catalysts

	Conv. of **1**	Yield of **2**	Yield of **3**	Yield of **4**
Au/HT	19%	8%	5%	3%
Au/CeO₂	24%	13%	7%	3%

Table 3-2. Reports for hydrogenation of **1** using Au catalysts

Entry	Catalyst	Conv. [%]	Sel. [%]	TON	Reference
1	Au@CeO$_2$/HT	>99	>99	200	This work
2	AuNP-phosphine complex	95	>99	50	55
3	Au/Mg$_2$AlO	56.4	97.5	-	53
4	Au/Fe$_2$O$_3$	>99	96.9	-	51
5	Au/*meso*-CeO$_2$	>99	92	100	54
6	Au/Fe(OH)$_x$	93	63	-	52

Au@CeO$_2$/HT also worked well for gram-scale reactions (Scheme 3-2). Thus, 20 mmol of substrates were chemoselectively hydrogenated, giving the desired products in excellent yields. After the hydrogenation of **1**, the solid Au@CeO$_2$/HT catalyst was easily recoverable by simple filtration and reusable without any loss of its catalytic activity or selectivity (Entry 2). The absence of Au species in the liquid phase was confirmed by inductively coupled plasma atomic emission spectroscopy (ICP-AES), which indicated no leaching of Au species from Au@CeO$_2$/HT. The TEM image of the reused Au@CeO$_2$/HT showed that the core-shell structure of Au@CeO$_2$ was retained without the aggregation of Au nanoparticles (Figure 3-4).
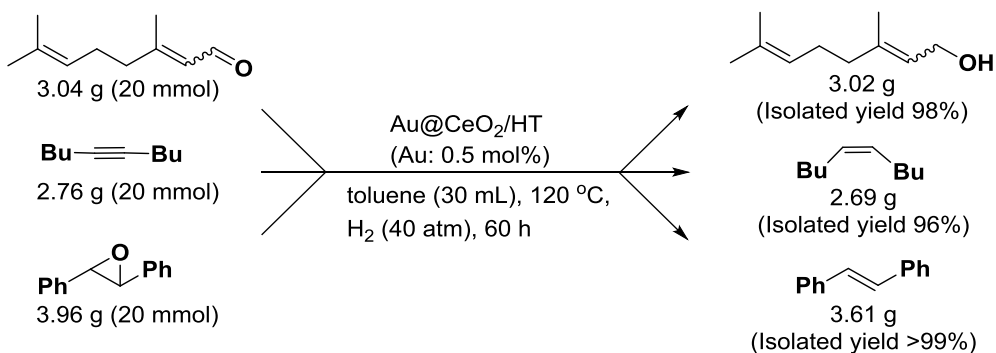
Scheme 3-2. Gram-scale reactions using Au@CeO$_2$/HT

Reactants:
- 3.04 g (20 mmol)
- Bu—≡—Bu, 2.76 g (20 mmol)
- 3.96 g (20 mmol)

Conditions:
Au@CeO$_2$/HT
(Au: 0.5 mol%)
toluene (30 mL), 120 °C,
H$_2$ (40 atm), 60 h

Products:
- OH, 3.02 g (Isolated yield 98%)
- Bu / Bu, 2.69 g (Isolated yield 96%)
- Ph / Ph, 3.61 g (Isolated yield >99%)

20 nm
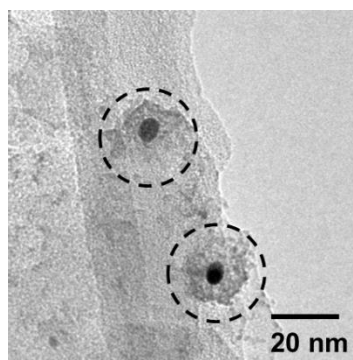
Figure 3-4. TEM image of the used Au@CeO$_2$/HT

Recently, Kaneda *et al.* reported that CeO$_2$-covered Au and Ag core-shell nanoparticle catalysts were effective in the chemoselective reductions of various functional groups while retaining C=C bonds (as was mentioned in Chapter I, Section 2-3) [40-43]. The high chemoselectivity originated from the cooperative action at the interface between core-Au or Ag and shell-CeO$_2$, where polar hydrogen species of M-H$^{\delta-}$ and CeO$_2$-H$^{\delta+}$ effectively formed through the heterolytic dissociation of H$_2$. These polar hydrogen species would be active for the targeted functional groups but inactive for the C=C bond, resulting in high chemoselectivity. To confirm the above idea, IR study was performed. When Au@CeO$_2$/HT was treated with H$_2$, new bands appeared around 2120 cm^{-1} and 3294 cm^{-1}, respectively (Figure 3-5, a). These peak positions were consistent with those attributed to Au-H$^{\delta-}$ and CeO$_2$-H$^{\delta+}$ in previous reports [62-65]. The formation of these

polar hydrogen species was well supported by the treatment of Au@CeO$_2$/HT with D$_2$ instead of H$_2$ (Figure 3-5, b). After the treatment of Au@CeO$_2$/HT with D$_2$ in place of H$_2$, no band around 2120 cm^{-1} was observed nor was a new band expected at 1503 cm^{-1} (νAu-H/1.41) found, indicating that the band at 2120 cm^{-1} shifted and overlapped with a strong peak derived from the ceria framework. Thus, the new band at 2120 cm^{-1} was due to the Au-H species. The treatment with D$_2$ also decreased the band around 3294 cm^{-1}, attributed to the O-H vibration, and a new band appeared around 2531 cm^{-1} corresponding to the O-D vibration, indicating the formation of CeO$_2$-D. Furthermore, the band attributed to Au-H$^{\delta-}$ gradually disappeared during the treatment with **1** at 120 $^{\circ}$C. These results clearly revealed that active polar hydrogen species were formed in the selective hydrogenation reactions.
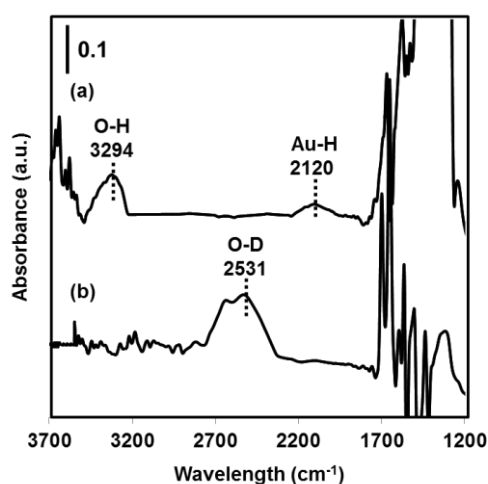
Figure 3-5. FT-IR spectra of Au@CeO$_2$/HT treated with (a) H$_2$ and (b) D$_2$.

4. Conclusion

This chapter demonstrated for the first time a green synthetic route for the core-shell nanoparticles under organic reagent-free and neutral conditions by using a redox-coprecipitation technique combined with metal oxides. Simply mixing core and shell precursors with various metal oxides in water allowed for the fabrication of small CeO$_2$-covered Au and Ag nanoparticles in one

step without reductants, surfactants, organic solvents or toxic bases. This facile method was also applicable to the large-scale synthesis of core-shell nanoparticles. Furthermore, the synthesized Au@CeO$_2$/HT acted as a highly efficient and reusable heterogeneous catalyst for a series of highly chemoselective hydrogenations of unsaturated aldehydes, alkynes and epoxides where the desired products were obtained with over 99% selectivities while retaining C=C bonds under additive-free conditions. Consequently, higher environmental compatibility and more efficient energy saving were achieved across the entire process, including catalyst preparation, reaction, separation, and reuse.

5. References

[1] C.-J. Zhong, M. M. Maye, *Adv. Mater.* **2001**, *13*, 1507-1511.

[2] S. Mourdikoudis, L. M. Liz-Marzan, *Chem. Mater.* **2013**, *25*, 1465-1476.

[3] S. L. Suib, *Chem. Rev.* **1993**, *93*, 803-826.

[4] K. Na, M. Choi, R. Ryoo, *Micropor. Mesopor. Mater.* **2013**, *166*, 3-19.

[5] S. Li, F. Huo, *Nanoscale* **2015**, *7*, 7842-501.

[6] B. Li, H.-M. Wen, Y. Cui, W. Zhou, G. Qian, B. Chen, *Adv. Mater.* **2016**, *28*, 8819-8860.

[7] D. Tasis, N. Tagmatarchis, A. Bianco, M. Prato, *Chem. Rev.* **2006**, *106*, 1105-1136.

[8] R. H. Baughman, A. A. Zakhidov, W. A. de Heer, *Science* **2002**, *297*, 787-792.

[9] A. D. Franklin, *Nature* **2013**, *498*, 443-444.

[10] J. Kim, Y. Piao, T. Hyeon, *Chem. Soc. Rev.* **2009**, *38*, 32-390.

[11] S. Sharifi, S. Behzadi, S. Laurent, M. L. Forrest, P. Stroeve, M. Mahmoudi, *Chem. Soc. Rev.* **2012**, *41*, 2323-2343.

[12] F. Peng, Y. Su, Y. Zhong, C. Fan, S.-T. Lee, Y. He, *Acc. Chem. Res.* **2014**, *47*, 612-623.

[13] S. Alayoglu, A. U. Nilekar, M. Mavrikakis, B. Eichhorn, *Nat. Mater.* **2008**, *7*, 333-338.

[14] F. Tao, M. E. Grass, Y. Zhang, D. R. Butcher, J. R. Renzas, Z. Liu, J. Y. Chung, B. S. Mun, M.

Salmeron, G. A. Somorjai, *Science* **2008**, *322*, 932-934.

[15] J. Ge, Q. Zhang, T. Zhang, Y. Yin, *Angew. Chem. Int. Ed.* **2008**, *47*, 8924-8928.

[16] Y. Yang, X. Liu, X. Li, J. Zhao, S. Bai, J. Liu, Q. Yang, *Angew. Chem. Int. Ed.* **2012**, *51*, 9164-9168.

[17] T. Mitsudome, Y. Takahashi, S. Ichikawa, T. Mizugaki, K. Jitsukawa, K. Kaneda, *Angew. Chem. Int. Ed.* **2013**, *52*, 1481-1485.

[18] D. I. Enache, J. K. Edwards, P. Landon, B. Solsona-Espriu, A. F. Carley, A. A. Herzing, M. Watanabe, C. J. Kiely, D. W. Knight, G. J. Hutchings, *Science* **2006**, *311*, 362-365.

[19] M. Cargnello, J. J. Delgaldo, J. C. H. Garrido, K. Bakhmutsky, T. Montini, J. J. C. Gamez, R. J. Gorte, P. Fornasiero, *Science* **2012**, *337*, 713-717.

[20] J. Zhang, Y. Tang, K. Lee, M. Ouyang, *Science* **2010**, *327*, 1634-1638.

[21] C. J. Serpell, J. Cookson, D. Ozkaya, P. D. Beer, *Nat. Chem.* **2011**, *3*, 478-483.

[22] S. Zhang, Y. Hao, D. Su, V.V. T. Doan-Nguyen, Y. Wu, J. Li, S. Sun, C. B. Murray, *J. Am. Chem. Soc.* **2014**, *136*, 15921-15924.

[23] J. Lai, K. V. P. M. Shafi, A. Ulman, K. Loos, R. Popovitz-Biro, Y. Lee, T. Vogt, C. Estournes, *J. Am. Chem. Soc.* **2005**, *127*, 5730-5731.

[24] W.-R. Lee, M. G. Kim, J.-R. Choi, J.-L. Park, S. J. Ko, S. J. Oh, J. Cheon, *J. Am. Chem. Soc.* **2005**, *127*, 16090-16097.

[25] J.-M. Yan, X.-B. Zhang, T. Akita, M. Haruta, Q. Xu, *J. Am. Chem. Soc.* **2010**, *132*, 5326-5327.

[26] S. Park, D. Yoon, S. Bang, J. Kim, H. Baik, H. Yang, K. Lee, *Nanoscale* **2015**, *7*, 15065-15069.

[27] Y. Lu, W. Chen, *Chem. Commun.* **2011**, *47*, 2541-2543.

[28] M. Cargnello, N. L. Wieder, T. Montini, R. J. Gorte, P. Fornasiero, *J. Am. Chem. Soc*. **2010**, *132*, 1402-1409.

[29] F. Qu, Y. Wang, J. Liu, S. Wen, Y. Chen, S. Ruan, *Mater. Lett.* **2014**, *132*, 167-170.

[30] Y. Lim, S. K. Kim, S.-C. Lee, J. Choi, K. S. Nahm, S. J. Yoo, P. Kim, *Nanoscale* **2014**, *6*, 4038-4042.

[31] T. Kayama, K. Yamazaki, H. Shinjoh, *J. Am. Chem. Soc.* **2010**, *132*, 13154-13155.

[32] J. Zhang, L. Li, X. Huang, G. Li, *J. Mat. Chem.* **2012**, *22*, 10480-10487.

[33] X. Wang, D. Liu, S. Song, H. Zhang, *J. Am. Chem. Soc.* **2013**, *135*, 15864-15872.

[34] Z. Xiong, L. Zhang, X. S. Zhao, *Chem. Eur. J.* **2014**, *20*, 14715-14720.

[35] X. Wang, D. Liu, J. Li, J. Zhen, F. Wang, H. Zhang, *Chem. Sci.* **2015**, *6*, 2877-2884.

[36] D. Liu, W. Li, X. Feng, Y. Zhang, *Chem. Sci.* **2015**, *6*, 7015-7019.

[37] X. Wang, D. Liu, J. Li, J. Zhen, H. Zhang, *NPG Asia Materials* **2015**, *7*, e158.

[38] Y. Liu, M. Wang, L. J.M.-Y. Yang, S. H.-S. Cheng, C.-W. Cao, K.-L. Leung, C.-Y. Chung, Z.-G. Lu, *J. Power Source* **2015**, *285*, 136-144.

[39] C. M. Y. Yeung, K. M. K. Yu, Q. J. Fu, D. Thompsett, M. I. Petch, S. C. Tsang, *J. Am. Chem. Soc.* **2005**, *127*, 18010-18011.

[40] T. Mitsudome, Y. Mikami, M. Matoba, T. Mizugaki, K. Jitsukawa, K. Kaneda, *Angew. Chem. Int. Ed.* **2012**, *51*, 136-139.

[41] T. Mitsudome, M. Matoba, T. Mizugaki, K. Jitsukawa, K. Kaneda, *Chem. Eur. J.* **2013**, *19*, 5255-5258.

[42] T. Mitsudome, M. Matoba, M. Yamamoto, T. Mizugaki, K. Jitsukawa, K. Kaneda, *Chem. Lett.* **2013**, *42*, 660-662.

[43] T. Mitsudome, M. Yamamoto, Z. Maeno, T. Mizugaki, K. Jitsukawa, K. Kaneda, *J. Am. Chem. Soc.* **2015**, *137*, 13452-13455.

[44] H.-U. Blaser, C. Malan, B. Pugin, F. Spindler, H. Steiner, M. Studer, *Adv. Synth. Catal.* **2003**, *345*, 103-151.

[45] K. Junge, K. Schröder, M. Beller, *Chem. Commun.* **2011**, *47*, 4849-4859.

[46] T. Mitsudome, K. Kaneda, *Green Chem*. **2013**, *15*, 2636-2654.

[47] *Comprehensive Organic Synthesis*, *second edition* (Eds: P. Knochel, G. A. Molander), Elsevier, Amsterdam, **2014** , *8*, 1-197.

[48] *Comprehensive Organic Synthesis*, *second edition* (Eds: P. Knochel, G. A. Molander), Elsevier, Amsterdam, **2014** , *8*, 198-299.

[49] P. Claus, A. Bruckner, C. Mohr, H. Hofmeister, *J. Am. Chem. Soc.* **2000**, *122*, 11430-11439.

[50] J. E. Baillie, H. A. Abdullah, J. A. Anderson, C. H. Rochester, N. V. Richardson, N. Hodge, J.-G. Zhang, A. Burrows, C. J. Kiely, G. J. Hutchings, *Phys. Chem. Chem. Phys.* **2001**, *3*, 4113-4121.

[51] C. Malone, M. L. Tropeano, G. Gulino, G. Neri, R. Ingoglia, S. Galvango, *Chem. Commun.* **2002**, 868-869.

[52] L. Liu, B. Qiao, Y. Ma, J. Zhang, Y. Deng, *Dalton Trans.* **2008**, 2542-2548.

[53] M.-M. Wang, L. He, Y.-M. Liu, Y. Cao, H.-Y. He, K.-N. Fan, *Green Chem.* **2011**, *13*, 602-607.

[54] I. Cano, A. M. Chapman, A. Urakawa, P. W. N. M. van Leeuwen, *J. Am. Chem. Soc.* **2014**, *136*, 2520-2528.

[55] B. S. Takale, S. Wang, X. Zhang, X. Feng, X. Yu, T. Jin, M. Bao, Y. Yamamoto, *Chem. Commun.* **2014**, *50*, 14401-14404.

[56] T. Mitsudome, A. Noujima, Y. Mikami, T. Mizugaki, K. Jitsukawa, K. Kaneda, *Chem. Eur. J.* **2010**, *16*, 11818-11821.

[57] A. Noujima, T. Mitsudome, T. Mizugaki, K. Jitsukawa, K. Kaneda, *Angew. Chem. Int. Ed.* **2011**, *50*, 2986-2989.

[58] J. Ni, L. He, Y.-M. Liu, Y. Cao, H.-Y. He, K.-N. Fan, *Chem. Commun.* **2011**, *47*, 812-814.

[59] L. Shao, X. Huang, D. Teschner, W. Zhang, *ACS Catal.* **2014**, *4,* 2369-2373.

[60] G. Li, R. Jin, *J. Am. Chem. Soc.* **2014**, *136*, 11347-11354.

[61] A. Corma, H. García, *Chem. Soc. Rev*. **2008**, *37*, 2096-2126.

[62] R. Juárez, S. F. Parker, P. Concepción, A. Corma, H. García, *Chem. Sci.* **2010**, *1*, 731-738.

[63] I. P. Silverwood, S. M. Rogers, S. K. Callear, S. F. Parker, R. A. Catlow, *Chem. Commun.* **2016**, *52*, 533-536.

[64] X. Wang, L. Andrews, *Angew. Chem.* **2003**, *115*, 5395-5364; *Angew. Chem. Int. Ed.* **2003**, *42*, 5201-5206.

[68] M. Manzoil, A. Chiorino, F. Vindigni, F. Boccuzzi, *Catal. Today* **2012**, *181*, 62-67.

Chapter IV.

Dehydrogenative Coupling of Hydrosilanes and Amines or Amides
Catalyzed by Hydroxyapatite-Supported Gold Nanoparticles

1. Introduction

Silylamines and silylamides are important materials for silylation reagents, ligands and valuable building blocks of silicone polymers [1-7]. Conventionally, these compounds have been synthesized through stoichiometric reactions of chlorosilanes with amines or amides, respectively, in the presence of bases [8, 9]. However, in this stoichiometric method, an excess amount of amines is required to obtain monosilylamines selectively and basic conditions are indispensable (Scheme 4-1, a), which restricts the applicability of these transformations. Furthermore, chlorosilanes are unstable in air moisture and hard-to-handle. In this context, dehydrogenative coupling of hydrosilanes with amines or amides is an alternative and attractive synthetic method of silylamines or silylamides (Scheme 4-1, b). The practical advantages of this coupling reaction such as usage of stable substrates, hydrosilanes, neutral reaction conditions, clean and separable byproduct (H_2) and no need to separate halogen salts enable efficient synthesis of diverse Si-N bond-containing compounds.

(a) Stoichiometric synthesis methods

$$R_3SiCl \ + \ R'NH_2 \xrightarrow[\text{Base}]{} R_3SiNHR' \ + \ (R_3Si)_2NR' \ + \ HCl \ salt$$
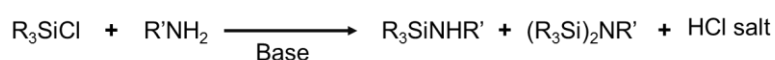
Disadvantage ・Unstable reagents   ・By-production of disilazanes

・Stoichiometric production of Cl salts   ・Basic conditions

(b) Alternative methods: Dehydrogenative coupling

$$R_3SiH \ + \ R'NH_2 \xrightarrow[]{\text{Catalyst}} R_3SiNHR' \ + \ H_2$$
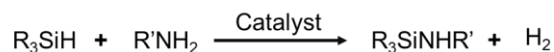
Advantage   ・Stable reagents   ・Clean and separable co-product (H_2)

・Neutral conditions

Scheme 4-1. Synthesis method of Si-N containing compounds

To date, several catalysts for the coupling reaction of hydrosilanes with amines have been developed [10-22]. However, these catalysts still have suffered from low activities [11-13, 17-19, 22], limitations of substrate scopes [11-21] and necessity of excess amounts of hydrosilanes or amines for

the highly selective coupling. Sadow *et al.* reported that To^MMgMe (To^M = tris(4,4-dimethyl-2-oxazolinyl)phenylborate) catalyst could promote this coupling reaction with the delicate modulation of the ratio of hydrosilane/amine [18]. However, without the modulation, the mixture of several products and polysilazanes were obtained. Moreover, this Mg catalyst was not applicable to the coupling reaction of the bulky hydrosilanes such as benzyldimethylsilane and triethylsilane. Cui *et al.* demonstrated homogeneous Yb-catalyzed dehydrogenative coupling of less bulky hydrosilanes with various amines [20]. In this report, high selectivity was attained by using bulky amines and less bulky amines caused low selectivity for target compounds because of the formation of the mixture of mono- and di-aminosilanes. M. Oestreich *et al.* developed the Ru-catalyzed efficient catalytic system for the coupling reactions [21]. Although this Ru catalyst showed relatively high catalytic activity (TON = 100, TOF = 2000 h^{-1}), the applicability of this catalyst was limited only to the coupling of aniline derivates. With regard to the coupling reaction of hydrosilanes with amides, only one catalytic method has been reported despite the utility of silylamides [23]. In this report, $NiCl_2$ acted as homogeneous catalyst for dehydrogenative coupling of tertialy hydrosilanes with amides. However, this catalytic system suffered from low acotivity (TON = 12), unavoidable addition of diethylsulfide and requirement of strictly dehydrated conditions. Therefore, it is clear that the development of an environmentally benign and highly efficient catalytic system for the selective coupling of hydrosilanes with amines or amides is still an important research target.

Hydroxyapatites (HAP, $Ca_{10}(PO_4)_6(OH)_2$) are the functional materials which act as biomaterials [24, 25], adsorbents [26, 27] and ion-exchangers [28]. Due to the high ion-exchange properties, HAP can immobilize the active metal species into its lattice and are widely used as metal ion-immobilized catalyst for various organic transformations [29, 30]. Furthermore, HAP shows the excellent adsorption ability and can stabilize small metal nanoparticles [31-34]. Moreover, HAP

81

possesses the high affinity with organic molecules and effectively collects the substrates on its surface during the heterogeneous catalytic reactions.

This chapter demonstrate a green protocol for the selective coupling of hydrosilanes with amines or amides using Au nanoparticle catalysts. Hydroxyapatite-supported Au nanoparticles with a mean diameter of 3.0 nm (Au/HAP) can act as an efficient heterogeneous catalyst for the selective coupling of various kinds of hydrosilanes with amines or amides. This catalytic system requires only equimolar amounts of hydrosilanes and amines or amides to achieve high-yielding synthesis of the desired Si–N bond-containing compounds. Furthermore, the catalytic activity of Au/HAP is significantly higher than those of the previously reported catalysts. Moreover, the Au/HAP catalyst is recoverable and reusable while maintaining its high catalytic performance.

2. Experimental Section

2-1. General

All organic reagents were purified before use. $HAuCl_4 \cdot xH_2O$ was obtained from Mitsuwa Chemicals Co., Ltd., and SiO_2 (JRC-SIO-6), Al_2O_3 (JRC-ALO-4) and TiO_2 (JRC-TIO-4) were obtained from the Catalysis Society of Japan as reference catalysts. GC-FID and GC-MS were performed on a Shimadzu GC-2014 instrument equipped with a OV-17 column (3 m) and a GCMS-QP2010 SE instrument equipped with an Inert Cap WAX-HT capillary column (30 m $\times$ 0.25 mm i.d., 0.25 μm), respectively. Inductively coupled plasma measurements were performed on a SII Nano Technology SPS7800 instrument. Gas-phase analysis was done with an on-line quadropole mass spectrometer (BELMass-S, BEL Japan, Inc.). ^1H and ^{13}C nuclear magnetic resonance (NMR) spectra were recorded on a JEOL JNM-ESC400 spectrometer and the chemical shifts are reported in ppm from TMS as a reference. Transmission electron microscopy (TEM) micrographs were obtained with a Hitachi HF-2000 microscope. Au L-edge X-ray absorption spectra were collected in the quick mode and recorded at room temperature in transmission mode at the facilities installed on the

BL-01B1 line attached with a Si (311) monochromator at SPring-8, Japan Atomic Energy Research Institute (JASRI), Harima, Japan. Data analysis was performed using the REX 2000 program, ver. 2.0.4 (Rigaku).

2-2. Preparation of catalysts

Au/HAP: Au/HAP was prepared according to previously reported method [31]. HAP (1.0 g) was added to 50 mL of aqueous solution of $HAuCl_4$ (2 mM). Then, 0.2 mL of aqueous NH_3 (10%) was added and the resulting mixture was stirred at room temperature for 12 h. The obtained slurry was filtered, washed with deionized water, and then dried at room temperature *in vacuo*. Subsequently, the obtained yellow powder was added to 50 mL of an aqueous solution of KBH_4 (18 mM) and stirred at room temperature for 1 h to yield Au/HAP as a purplish red powder.

Ag/HAP: Ag/HAP was prepared according to previously reported method [32]. HAP (2.0 g) was added to 150 mL of aqueous solution of $AgNO_3$ (6.7 mM) and stirred at room temperature for 6 h. The obtained slurry was filtered, washed with deionized water, and then dried at room temperature *in vacuo*. Subsequently, the obtained gray powder was added to 100 mL of an aqueous solution of KBH_4 (0.1 M) and stirred at room temperature for 1 h to yield Ag/HAP as a purplish red powder.

Cu/HAP: Cu/HAP was prepared according to previously reported method [35]. HAP (1.0 g) was added to 50 mL of aqueous solution of $Cu(SO_3CF_3)_2$ (16 mM), then the pH of the mixture was adjusted to 8.0 with aqueous NH_3 (25%). The resulting mixtures were stirred at room temperature for 1 h. After stirring, the slurry was filtered, washed with deionized water, and then dried at room temperature *in vacuo*. The obtained blue powder was reduced with 1 atm of H_2 at 180 ^{o}C before the reactions.

Supported other metal nanoparticles: HAP (1.0 g) was added to 50 mL of aqueous solution of Na_2PdCl_4, $RhCl_3$, Na_2PtCl_4 and $RuCl_3$ (2 mM). The mixtures were stirred at room temperature for 6 h, followed by evaporation to dryness. Subsequent treatment with KBH_4 at room temperature for 1 h

yielded Pd/HAP, Rh/HAP, Pt/HAP and Ru/HAP.

2-3. Characterization of Au/HAP

The amount of Au loading on Au/HAP was estimated to be 1.65 wt% by elemental analysis. The shape of the Au L_{III}-edge X-ray absorption near-edge structure (XANES) spectrum of Au/HAP was closely similar to that of Au foil and the absorption edge was assigned to the formation of Au(0) species. The Fourier transform of the k_3-weighted Au L_{III}-edge extended X-ray absorption fine structure (EXAFS) of Au/HAP revealed a peak around 2.8 Å attributed to Au-Au bonds. The peak magnitude for Au/HAP was much lower than that for the Au foil, showing the formation of Au nanoparticles in Au/HAP (Figure 4-1). TEM confirmed that Au nanoparticles with a mean diameter of 3 nm were highly dispersed on the surface of HAP (Figure 4-2).
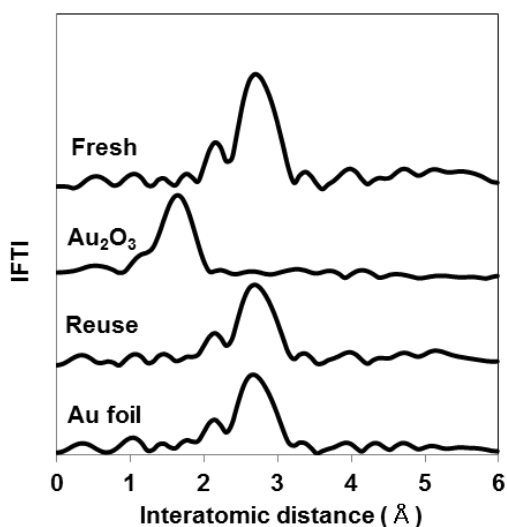
Curve fitting analysis of Au L-edge EXAFS

	Coord. no. (CN)	Interatomic dis. (Å)	$\Delta\sigma$ (Å)[a]
Au/HAP (fresh)	10.0	2.85	0.0080
Au/HAP (after two times reuse)	10.2	2.85	0.0076
Au foil	12	2.88	-

[a] Difference between Debye-Waller factor.

Figure 4-1. Fourier transformed k^3-weighted Au L-edge EXAFS for Au catalysts
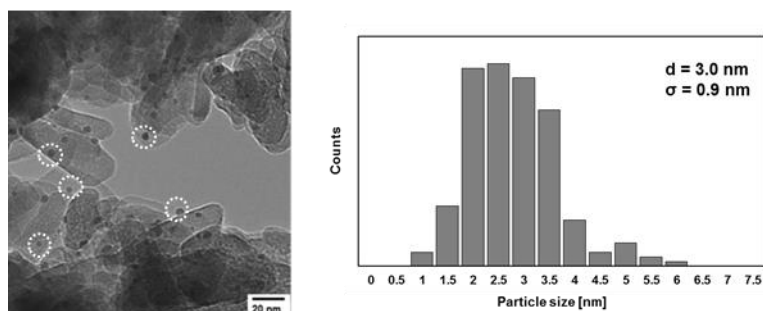
Figure 4-2. TEM image of Au/HAP and its size distribution histogram

2-4. Typical reaction procedures

A typical reaction procedure for the dehydrogenative coupling of dimethylphenylsilane (**1**) with *n*-butylamine (**2**) using the Au/HAP catalyst was as follows. Au/HAP (0.1 g, 0.0083 mmol Au) was placed in a reaction vessel, followed by the addition of internal standard (naphthalene: 0.5 mmol), THF (3 mL), **1** (1 mmol) and **2** (1 mmol). The reaction mixture was vigorously stirred at 60 °C under Ar atmosphere for 4 h. Au/HAP was filtered and the yield was determined by GC analysis. The product was isolated by Kugelrohr distillation.

2-5. Large-scale reaction

Large-scale reaction of **1** with **2** was performed in a pressure resistant vessel at 110 °C under Ar atmosphere for 40 h. After the coupling reaction, Au/HAP was filtered and the yield was determined by GC analysis. The product was isolated by Kugelrohr distillation.

2-6. Measurement of H_2

The amount of H_2 generated during the reaction was measured by GC-TCD. The dehydrogenation was carried out under standard reaction conditions in a closed vessel with on-line GC-TCD. After the reaction, the gas phase was subjected to GC-TCD for qualitative and quantitative analysis of H_2. Once the H_2 concentration in the headspace was determined, quantity was simply multiplied by the total flask volume.

2-7. Detection of HD

The formation of HD was confirmed with an on-line quadropole mass spectrometer (BELMass-S, BEL Japan, Inc.). The dehydrogenation was carried out in a closed vessel under standard reaction conditions. After the reaction, the gas phase was subjected to BELMass-S. The gas phase was analyzed by monitoring the signal of $m/z = 2$, 3 and 4.

2-8. Product identification

The products were identified by GC, GC-MS, and NMR analyses. Chemical shifts (^{1}H and ^{13}C NMR) of the product were in agreement with previous reports.

N-*n*-Butyldimethylphenylsilylamine: CAS registry No. [4774-69-0] (Table 2-1)

^{1}H NMR (400 MHz, CDCl$_3$): δ 7.55-7.60 (m, 2H), 7.38-7.34 (m, 3H), 2.72 (dd, J = 12.0 Hz, J = 6.4 Hz, 2H), 1.23-1.46 (m, 4H), 0.87 (t, J = 4.0 Hz, 3H), 0.64 (br s, 1H), 0.30 ppm (s, 6H); ^{13}C NMR (100 MHz, CDCl$_3$): δ 133.6, 128.8, 127.7, 127.6, 41.8, 36.9, 19.9, 13.9, -1.4 ppm.

N-*t*-Butyldimethylphenylsilylamine: CAS registry No. [91308-42-8] (Table 2-2, Entry 2)

^{1}H NMR (400 MHz, CDCl$_3$): δ 7.21-7.31 (m, 2H), 6.96-7.06 (m, 3H), 1.12 (s, 6H), 0.80 (br s, 1H), 0.33 ppm (s, 6H); ^{13}C NMR (100 MHz, CDCl$_3$): δ 141.7, 133.4, 128.6, 127.5, 49.6, 33.8, 1.2 ppm.

N-Allyldimethylphenylsilylamine: (Table 2-2, Entry 3)

^{1}H NMR (400 MHz, CDCl$_3$): δ 7.56-7.60 (m, 2H), 7.34-7.37 (m, 3H), 5.83-5.95 (m, 1H), 5.10-5.16 (m, 1H), 4.95-5.00 (m, 1H), 3.36 (dd, J = 3.2 Hz, J = 4.8 Hz, 2H), 0.74 (br s, 1H), 0.31 ppm (s, 6H); ^{13}C NMR (100 MHz, CDCl$_3$): δ 140.5, 139.9, 133.6, 129.0, 127.7, 113.0, 44.7, -1.4 ppm. HRMS (DART) exact mass for (C$_{11}$H$_{18}$NSi + H) calcd m/z 192.1203, found 192.1205.

N-Dimethylphenylsilylmorpholine: CAS registry No. [863454-94-8] (Table 2-2, Entry 4)

^{1}H NMR (400 MHz, CDCl$_3$): δ 7.49-7.57 (m, 2H), 7.30-7.39 (m, 3H), 3.54 (t, J = 10.8 Hz, 2H), 2.88 (t, J = 7.2 Hz, 3H), 0.32 ppm (s, 6H); ^{13}C NMR (100 MHz, CDCl$_3$): δ 138.6, 133.7, 129.0, 127.7,

68.5, 45.8, -2.4 ppm.

N,N-Diethyldimethylphenylsilylamine: CAS registry No. [26210-60-6] (Table 2-2, Entry 5)

^{1}H NMR (400 MHz, CDCl$_3$): δ 7.51-7.57 (m, 2H), 7.31-7.37 (m, 3H), 2.84 (dd, J = 12.0 Hz, J = 8.4 Hz, 4H), 0.98 (dd, J = 6.8 Hz, J = 6.8 Hz, 6H), 0.30 ppm (s, 6H); ^{13}C NMR (100 MHz, CDCl$_3$): δ 140.7, 133.8, 128.7, 127.5, 40.2, 15.8, -1.3 ppm.

Dimethylphenylsilylamine: (Table 2-2, Entry 6)

^{1}H NMR (400 MHz, CDCl$_3$): δ 7.51-7.58 (m, 2H), 7.30-7.37 (m, 3H), 0.29 ppm (s, 6H); ^{13}C NMR (100 MHz, CDCl$_3$): δ 141.2, 133.4, 128.9, 127.7,, 1.1 ppm. HRMS (DART) exact mass for (C$_8$H$_{13}$NSi + H) calcd m/z 152.0890, found 152.0892.

N-Dimethylphenylsilylaniline: CAS registry No. [13091-06-0] (Table 2-2, Entry 7)

^{1}H NMR (400 MHz, CDCl$_3$): δ 7.56-7.67 (m, 2H), 7.30-7.41 (m, 3H), 7.03-7.11 (m, 2H), 6.55-6.73 (m, 3H), 3.62 (br s, 1H), 0.49 ppm (s, 6H); ^{13}C NMR (100 MHz, CDCl$_3$): δ 146.8, 133.5, 129.5, 129.0, 127.9, 117.7, 116.4, -1.8 ppm.

N-Dimethylphenylsilyl-4-bromoaniline: (Table 2-2, Entry 8)

^{1}H NMR (400 MHz, CDCl$_3$): δ 7.56-7.60 (m, 2H), 7.32-7.39 (m, 3H), 7.10-7.16 (m, 2H), 6.42-6.50 (m, 2H), 3.66 (br s, 1H), 0.47 ppm (s, 6H); ^{13}C NMR (100 MHz, CDCl$_3$): δ 146.0, 137.4, 133.6, 131.9, 129.7, 128.1, 127.9, 110.1, 109.7, -1.4 ppm. HRMS (FAB) exact mass for (C$_{14}$H$_{16}$BrNSi) calcd m/z 305.0235, found 305.0235.

N-Dimethylphenylsilyl-4-methoxyaniline: (Table 2-2, Entry 9)

^{1}H NMR (400 MHz, CDCl$_3$): δ 7.54-7.64 (m, 2H), 7.33-7.39 (m, 3H), 6.63-6.75 (m, 2H), 6.51-6.59 (m, 2H), 3.70 (s, 3H), 3.43 (br s, 1H), 0.45 ppm (s, 6H); ^{13}C NMR (100 MHz, CDCl$_3$): δ 152.1, 140.5, 138.3, 133.6, 129.4, 127.9, 117.2, 114.7, 55.6, -1.3 ppm. HRMS (FAB) exact mass for (C$_{15}$H$_{19}$ONSi) calcd m/z 257.1236, found 257.1240.

***N-n*-Butylmethyldiphenylsilylamine**: CAS registry No. [4774-70-3] (Table 2-2, Entry 10)

^{1}H NMR (400 MHz, CDCl$_3$): δ 7.55-7.61 (m, 4H), 7.30-7.39 (m, 6H), 2.79 (ddd, *J* = 7.2 Hz, *J* = 14.8 Hz, 2H), 1.25-1.49 (m, 4H), 0.86 (t, *J* = 3.6 Hz, 3H), 0.57 ppm (s, 3H); ^{13}C NMR (100 MHz, CDCl$_3$): δ 137.9, 134.2, 129.4, 127.7, 42.0, 36.9, 20.6, 14.1, -2.37 ppm.

***N-n*-Butyltriphenylsilylamine**: CAS registry No. [18752-82-4] (Table 2-2, Entry 11)

^{1}H NMR (400 MHz, CDCl$_3$): δ 7.55-7.65 (m, 6H), 7.31-7.42 (m, 9H) , 2.81 (dd, *J* = 8.4 Hz, *J* = 16 Hz, 2H), 1.24-1.47 (m, 4H), 1.17 (br s, 1H), 0.84 ppm (t, *J* = 10 Hz, 3H); ^{13}C NMR (100 MHz, CDCl$_3$): δ 136.0, 135.4, 129.4, 127.7, 42.3, 36.6, 19.9, 13.8 ppm.

***N-n*-Butyltriethylsilylamine**: CAS registry No. [17940-18-0] (Table 2-2, Entry 12)

^{1}H NMR (400 MHz, CDCl$_3$): δ 2.72 (dd, *J* = 4.4 Hz, *J* = 12.4 Hz, 2H), 1.27-1.41 (m, 4H), 0.94 (dd, *J* = 8.0 Hz, *J* = 16.4 Hz, 12H), 0.52 (dd, *J* = 8.4 Hz, *J* = 15.6 Hz, 6H), 0.29 ppm (br s,1H); ^{13}C NMR (100 MHz, CDCl$_3$): δ 41.8, 37.2, 20.0, 14.0, 7.2, 4.7 ppm.

Triethylsilylamine: (Table 2-2, Entry 13)

^{1}H NMR (400 MHz, CDCl$_3$): δ 0.94 (t, *J* = 9.6 Hz, 9H), 0.55 ppm (dq, *J* = 8.0 Hz, *J* = 5.6 Hz, 6H); ^{13}C NMR (100 MHz, CDCl$_3$): δ 6.7, 6.4 ppm.

***N-n*-Butylbenzyldimethylsilylamine**: (Table 2-2, Entry 14)

^{1}H NMR (400 MHz, CDCl$_3$): δ 7.31-7.37 (m, 2H), 7.14-7.22 (m, 3H), 2.81 (dd, *J* = 7.2 Hz, *J* = 14.0 Hz, 2H), 1.37-1.52 (m, 4H), 1.02 (t, *J* = 6.8 Hz, 3H), 0.51 (br s,1H), 0.14 ppm (s, 6H); ^{13}C NMR (100 MHz, CDCl$_3$): δ 140.4, 128.1, 128.0, 123.7, 41.6, 36.9, 27.5, 19.9, 13.9, -2.2 ppm. HRMS (DART) exact mass for (C$_{13}$H$_{23}$NSi + H) calcd *m/z* 222.1673, found 222.1676.

***N-n*-Butyldiphenylsilylamine**: CAS registry No. [1334953-36-4] (Table 2-2, Entry 15)

^{1}H NMR (400 MHz, CDCl$_3$): δ 7.52-7.65 (m, 4H), 7.28-7.43 (m, 6H), 5.31 (s, 1H), 2.83 (dd, *J* = 7.6 Hz, *J* = 14.9 Hz, 2H), 1.22-1.49 (m, 4H), 0.74-0.98 ppm (m, 3H); ^{13}C NMR (100 MHz, CDCl$_3$): δ 134.7, 129.7, 127.8, 127.7, 42.7, 36.5, 20.0, 13.9 ppm.

Diphenylsilylaniline: CAS registry No. [5931-21-5] (Table 2-2, Entry 16)

^{1}H NMR (400 MHz, CDCl$_3$): δ 7.57-7.69 (m, 4H), 7.29-7.46 (m, 6H), 6.99-7.12 (m, 2H), 6.62-6.76 (m, 3H), 5.60 (d, J = 3.6 Hz, 1H), 3.83 ppm (s, 1H); ^{13}C NMR (100 MHz, CDCl$_3$): δ 146.5, 135.3, 134.5, 129.9, 128.8, 127.7, 118.6, 116.4 ppm.

N-n-Butylmethylphenylsilylamine: (Table 2-2, Entry 17)

^{1}H NMR (400 MHz, CDCl$_3$): δ 7.51-7.64 (m, 2H), 7.31-7.41 (m, 3H), 4.86 (s, 1H), 2.77 (dd, J = 5.2 Hz, J = 11.7 Hz, 2H), 1.24-1.45 (m, 4H), 0.87 (t, J = 7.6 Hz, 3H), 0.68 (br s, 1H), 0.34 ppm (d, J = 2.8 Hz, 3H); ^{13}C NMR (100 MHz, CDCl$_3$): δ 138.6, 134.7, 130.1, 128.5, 43.1, 37.2, 20.5, 14.5, -2.3 ppm. HRMS (DART) exact mass for (C$_{11}$H$_{19}$NSi + H) calcd m/z 194.1360, found 194.1362.

Methylphenylsilylaniline: CAS registry No. [66535-18-0] (Table 2-2, Entry 18)

^{1}H NMR (400 MHz, CDCl$_3$): δ 7.60-7.66 (m, 2H), 7.34-7.43 (m, 3H), 7.07-7.14 (m, 2H), 6.65-6.74 (m, 3H), 5.16 (s, 1H), 3.66 (s, 1H), 0.54 ppm (d, J = 2.4 Hz, 3H); ^{13}C NMR (100 MHz, CDCl$_3$): δ 146.7, 135.3, 134.0, 130.1, 129.2, 128.1, 118.1, 116.2, -3.4 ppm.

N-n-Butyl(di-t-butylsilyl)amine: (Table 2-2, Entry 19)

^{1}H NMR (400 MHz, CDCl$_3$): δ 3.76 (d, J = 5.2 Hz, 1H), 2.83 (ddd, J = 6.8 Hz, J = 13.6 Hz, 2H), 1.29-1.46 (m, 4H), 0.98 (s, 18H), 0.90 (t, J = 7.6 Hz, 3H), 0.27 ppm (br s, 1H); ^{13}C NMR (100 MHz, CDCl$_3$): δ 45.0, 36.9, 28.1, 20.0, 19.9, 14.0 ppm. HRMS (DART) exact mass for (C$_{12}$H$_{29}$NSi + H) calcd m/z 216.2142, found 216.2141.

Di-t-butylsilylaniline (Table 2-2, Entry 20)

^{1}H NMR (400 MHz, CDCl$_3$): δ 7.08-7.15 (m, 2H), 6.67-6.80 (m, 3H), 4.33 (d, J = 5.2 Hz, 1H), 3.28 (br s, 1H), 1.05 (s, 18H); ^{13}C NMR (100 MHz, CDCl$_3$): δ 148.4, 129.0, 117.8, 116.8, 27.9, 20.2 ppm. HRMS (DART) exact mass for (C$_{14}$H$_{25}$NSi + H) calcd m/z 236.1829, found 236.1830.

N-(Dimethylphenylsilyl)benzamide: CAS registry No. [75732-29-5] (Scheme 2-3)

^{1}H NMR (400 MHz, CDCl$_3$): δ 7.75-7.83 (m, 2H), 7.65-7.71 (m, 2H), 7.37-7.48 (m, 6H), 5.85 (br s,

1H), 0.64 ppm (s, 6H); ^{13}C NMR (100 MHz, CDCl$_3$): δ 172.2, 134.9, 133.6, 131.7, 130.0, 128.5, 128.1, 127.4, 127.3, -2.2 ppm.

N-(Dimethylphenylsilyl)-4-fluorobenzamide: (Scheme 2-3)

^{1}H NMR (400 MHz, CDCl$_3$): δ 7.76-7.83 (m, 2H), 7.65-7.68 (m, 2H), 7.36-7.47 (m, 3H), 7.02-7.12 (m, 2H), 5.77 (br s, 1H), 0.63 ppm (s, 6H); ^{13}C NMR (100 MHz, CDCl$_3$): δ 171.0, 163.6, 136.2, 133.6, 130.9, 130.0, 129.6, 128.0, 115.3, -2.2 ppm. HRMS (DART) exact mass for (C$_{15}$H$_{16}$FNOSi + H) calcd m/z 274.1058, found 274.1060.

N-(Dimethylphenylsilyl)-cyclohexanecarboxamide: (Scheme 2-3)

^{1}H NMR (400 MHz, CDCl$_3$): δ 7.45-7.57 (m, 2H), 7.22-7.37 (m, 3H), 5.39 (br s, 1H), 2.09-2.18 (m, 1H), 1.27-1.63 (m, 6H), 1.20-1.30 (m, 4H), 0.31 ppm (s, 6H); ^{13}C NMR (100 MHz, CDCl$_3$): δ 182.2, 133.5, 132.9, 128.0, 127.5, 46.6, 29.8, 25.7, 0.8, -2.2 ppm. HRMS (DART) exact mass for (C$_{15}$H$_{23}$NOSi + H) calcd m/z 262.1622, found 262.1623.

N-(Dimethylphenylsilyl)-n-valeramide: (Scheme 2-3)

^{1}H NMR (400 MHz, CDCl$_3$): δ 7.49-7.60 (m, 2H), 7.23-7.39 (m, 3H), 5.04 (br s, 1H), 2.19 (t, J = 10.8 Hz, 2H), 1.55 (m, 2H), 1.30 (m, 2H), 0.87 (t, J = 10.4 Hz, 3H), 0.56 ppm (s, 6H); ^{13}C NMR (100 MHz, CDCl$_3$): δ 178.9, 133.5, 132.9, 127.9, 127.7, 27.6, 22.3, 13.8, 0.8, -2.2 ppm. HRMS (DART) exact mass for (C$_{13}$H$_{21}$NOSi + H) calcd m/z 236.1465, found 236.1468.

3. Results and Discussion

Various HAP-supported metal nanoparticles were synthesized and the catalytic activities were investigated in the coupling reaction of an equimolar amount of dimethylphenylsilane (**1**) and *n*-butylamine (**2**) in THF solvent (Table 4-1). Among the tested metal nanoparticles, Au/HAP exhibited the best activity to afford *N*-(*n*-butyl)dimethylphenylsilylamine (**3**) in > 99% yield accompanied by the generation of equimolar amounts of H_2 (Entry 1). Ag/HAP and Pd/HAP were also active but the yields of **3** were much lower than that of Au/HAP (Entries 4 and 5). Other metal nanoparticles such as Cu, Ru, Rh and Pt did not show any activities (Entries 6-9), revealing that Au nanoparticles had uniquely high catalytic activity. Then, the support effect of different kinds of inorganic materials to immobilize Au nanoparticles was investigated, and it was revealed that HAP

Table 4-1. Dehydrogenative coupling of **1** with **2** using various catalysts[a]

$$PhMe_2SiH + \underset{\textbf{2}}{\textit{n}\text{-BuNH}_2} \xrightarrow[\text{THF, Ar, 60 }^\circ\text{C, 4 h}]{\text{catalyst}} \underset{\textbf{3}}{PhMe_2SiNH(\textit{n}\text{-Bu})}$$

Entry	Catalyst	d [nm]	Conv. (Yield) [%][b]
1	Au/HAP	3.0	99
2[c]	Au/HAP	3.0	99
3[d]	Au/HAP	3.0	99
4	Ag/HAP	5.4	54
5	Pd/HAP	3.2	48
6	Cu/HAP	4.0	0
7	Ru/HAP	2.4	0
8	Rh/HAP	3.3	0
9	Pt/HAP	4.8	0
10	Au/TiO$_2$	3.6	72
11	Au/Al$_2$O$_3$	3.6	63
12	Au/SiO$_2$	2.2	29
13	Au/MgO	3.1	15
14	Au/HAP	5.7	83
15	Au/HAP	6.5	33

[a]Reaction conditions: Catalyst (metal: 0.83 mol%), **1** (1 mmol), **2** (1 mmol), THF (3 mL). [b]Determined by GC using an internal standard technique. [c]Reuse 1. [d]Reuse 2.
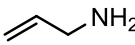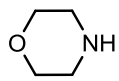
91

was an effective support compared to other supports such as TiO_2, Al_2O_3, SiO_2 and MgO (Entries 1 vs. 10-13). This prominent catalytic activity of Au/HAP may be due to the strong adsorption ability of HAP for hydrosilanes. The highly condensed hydrosilanes on the HAP surface efficiently interacted with active sites on Au nanoparticles, leading to high catalytic activity of Au/HAP [31]. The size effect of Au nanoparticles was also studied using Au/HAP having different Au particle sizes, confirming that smaller Au nanoparticles provided higher catalytic activities (Entries 1 vs. 14 and 15).

With the optimized Au/HAP catalyst having a mean diameter of 3.0 nm in hand, the scope of hydrosilanes and amines was explored in this transformation (Table 4-2). Au/HAP showed broad applicability for diverse combinations of hydrosilanes with amines in the use of an equimolar amount of hydrosilanes to amines. **1** was efficiently coupled with aliphatic (Entries 1-6) and aromatic (Entries 7-9) amines, providing the corresponding silylamines in high yields. Functionalized amines such as allylamine (Entry 3), morpholine (Entry 4) and bromoaniline (Entry 8) were also applicable. It is said that the use of ammonia in this coupling reaction often causes low selectivity [36] and low yields [18] of the corresponding mono-silylamines due to the production of disilazane by-products and poisoning by strong coordination of ammonia to active metal species, respectively. In contrast, Au/HAP worked well, giving the mono-silylamine in high yields (Entries 6 and 13). The high-yielding coupling reaction of other tertiary hydrosilanes with **2** was also successful (Entries 10-12 and 14). Although sterically hindered hydrosilanes such as triethylsilane and benzyldimethylsilane are known to be only slightly reactive [18], these were quantitatively coupled with **2** to afford the corresponding silylamines (Entries 12 and 14).

Selective synthesis of mono-aminosilanes from hydrosilanes containing multiple Si–H bonds is a challenging issue because of the easy formation of the undesired silazanes as the by-products. Notably, the present Au/HAP catalyst system was useful for the synthesis of

Table 4-2. Dehydrogenative coupling of hydrosilanes with amines using Au/HAP[a]

$$R_1R_2R_3SiH + R'R''NH \xrightarrow[\text{THF (3 mL), Ar}]{\text{Au/HAP (Au: 0.83 mol\%)}} R_1R_2R_3SiNR'R'' + H_2$$

Entry	Hydrosilane	Amine	Temp. [°C]	Time [h]	Yield [%][b]
1	$PhMe_2SiH$	$n\text{-}BuNH_2$	60	4	99 (87)
2		$t\text{-}BuNH_2$	100	10	96 (88)
3		NH₂	60	3	99 (86)
4		O NH	60	8	99 (86)
5		Et_2NH	100	10	92 (83)
6		NH_3	100	1	(90)
7	R NH₂	R = H	40	1	99 (88)
8		4-Br	40	2	97 (82)
9		4-MeO	40	2	99 (88)
10	Ph_2MeSiH	$n\text{-}BuNH_2$	60	16	95 (87)
11[c]	Ph_3SiH	$n\text{-}BuNH_2$	100	20	96 (85)
12	Et_3SiH	$n\text{-}BuNH_2$	100	12	99 (86)
13		NH_3	100	20	(86)
14	$BnMe_2SiH$	$n\text{-}BuNH_2$	60	12	99 (83)
15	Ph_2SiH_2	$n\text{-}BuNH_2$	60	2	99 (84)
16		$PhNH_2$	25	0.5	99 (86)
17	$PhMeSiH_2$	$n\text{-}BuNH_2$	60	2	95 (84)
18		$PhNH_2$	25	1	89 (78)
19	$t\text{-}Bu_2SiH_2$	$n\text{-}BuNH_2$	60	0.5	98 (88)
20		$PhNH_2$	25	1	99 (85)
21[d]	Ph_2SiH_2	$PhNH_2$	60	1	99[e]
22	$Ph_2SiHNHPh$	$PhNH_2$	60	1	0

[a]Reaction conditions: Au/HAP (Au: 0.83 mol%), hydrosilane (1 mmol), amine (1 mmol), THF (3 mL), Ar. [b]Determined by GC using an internal standard technique; values in parenthesis are the yield of the isolated products. [c]Au/HAP (Au: 1.6 mol%), hydrosilane (0.5 mmol), amine (0.5 mmol), THF (2 mL), Ar. [d]Aniline (2 mmol). [e]Yield of the monoaminosilane.

mono-aminosilanes from dihydrosilanes. The selective coupling of dihydrosilanes with simple amines in an equimolar ratio successfully proceeded, giving the desired mono-aminosilanes in excellent yields (Entries 15-20). This result is in sharp contrast with previous reports where the delicate modulation of the ratio of silane/amine [13, 18] or use of bulky amines [20] was required to achieve high selectivity of mono-aminosilanes.

To elucidate the reason of high selectivity toward mono-aminosilanes, the following control experiments were investigated. 1) Monoamino-hydrosilane was solely produced when using 2 equiv. of amine with hydrosilane (Entry 21). 2) When the monoamino-hydrosilane diphenylsilylaniline was employed as a starting material, no reaction occurred and diphenylsilylaniline was quantitatively recovered (Entry 22). These results clearly demonstrated that the reason for the high selectivity is due to no reactivity of the monoamino-hydrosilanes under our reaction conditions.

The possibility of the participation of homogeneous Au species leached from Au/HAP was also investigated. The coupling processes were abruptly and completely terminated by the removal of Au/HAP from the reaction mixtures by filtration and no leaching of Au species could be detected by inductively coupled plasma (ICP) analysis of the filtrate, thus proving that the observed catalysis of Au/HAP was intrinsically heterogeneous. In addition, Au/HAP showed excellent reusability in the recycling experiments (Table 4-1, Entries 2 and 3). Furthermore, the image of Au/HAP after the reuse showed that no aggregation of Au nanoparticles occurred and that the average diameters of the reused Au nanoparticles were similar to those of the fresh ones (Figure 4-3).
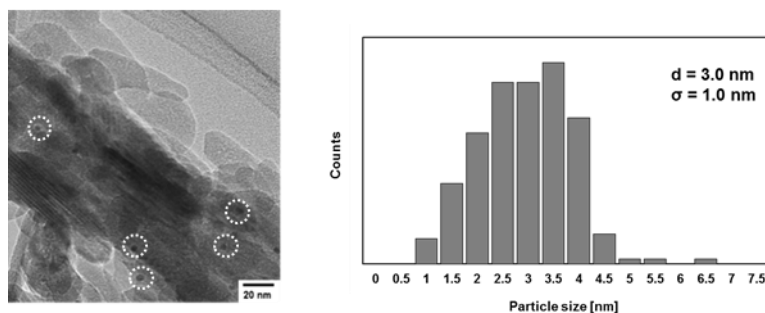
Figure 4-3. TEM image of Au/HAP after the reuse and its size distribution

.

The practical applicability of Au/HAP for the gram-scale synthesis of silylamines was also demonstrated in the coupling of **1** with **2** (Scheme 4-2). The transformation proceeded efficiently, giving 1.83 g of the silylamine (86% isolated yield), where the turnover number reached 5180. This value is the best among reported catalysts (Table 4-3).
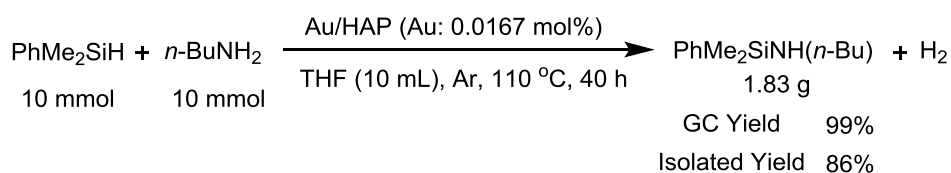

Scheme 4-2. Gram-scale synthesis of silylamine

Table 4-3. Comparison of TON

Catalyst	TON	Reference
Au/HAP	**5180**	**This work**
Pd/C	174	10
$[(Et_2N)_3U][BPh]_4$	118	15
tethered ruthenium complex	100	21
$Ru_3(CO)_{12}$	100	19
$[Cp(Pri_3P)Ru(NCMe)_2]^+BAF$	33	17
$Yb(\eta^2\text{-Ph}_2CNAr)(hmpa)_4$	33	14
$areneCr(CO)_2(\eta^2\text{-HSiHPh}_2)$	20	12
$[(NHC)Yb(SiMe_3)_2]$	20	20
$ToMMg\text{-}NR_2$	20	18
$[M\{N(SiMe_3)_2\}_2]_2$	20	21
CuCl	15	13

Next, the catalytic potential of Au/HAP to the selective synthesis of silylamides was investigated in the coupling of **1** with several amides. The results exemplified in Scheme 4-3 revealed that Au/HAP showed high efficiency in this transformation under additive-free conditions. Furthermore, the activity of Au/HAP was 13-fold higher than that of the reported homogeneous Ni catalyst, demonstrating the first example of a highly active heterogeneous catalyst [23].
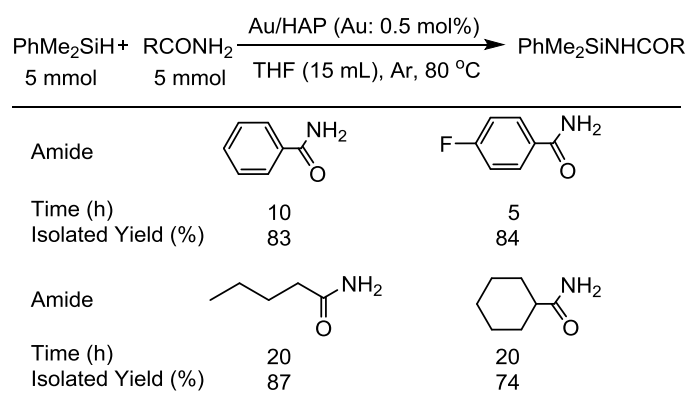
Scheme 4-3. Dehydrogenative of **1** with amides using Au/HAP

To gain insights into the catalytic features of Au/HAP in the coupling of hydrosilanes with amines, the dependency of reaction rates using **1** and **2** were investigated under Ar atmosphere at 60 °C. The initial rate was proportional to the amount of **1** (Figure 4-4) and independent of the concentration of **2** (Figure 4-5).
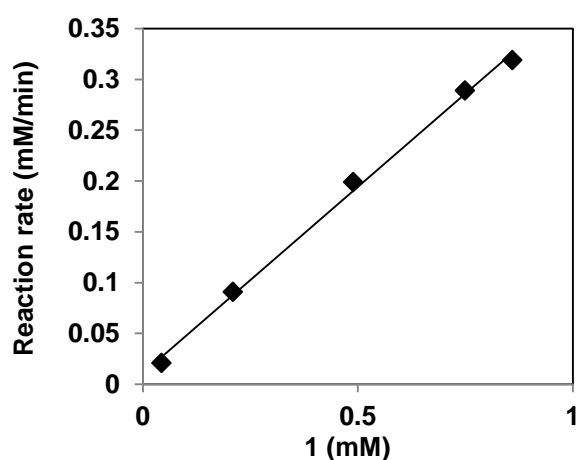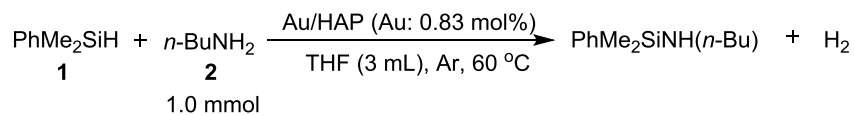
$$PhMe_2SiH + n\text{-}BuNH_2 \xrightarrow[\text{THF (3 mL), Ar, 60 °C}]{\text{Au/HAP (Au: 0.83 mol\%)}} PhMe_2SiNH(n\text{-}Bu) + H_2$$

1   **2**
1.0 mmol

Figure 4-4. Dependency on the concentration of **1**

$$PhMe_2SiH + n\text{-}BuNH_2 \xrightarrow[\text{THF (3 mL), Ar, 60 °C}]{\text{Au/HAP (Au: 0.83 mol\%)}} PhMe_2SiNH(n\text{-}Bu) + H_2$$
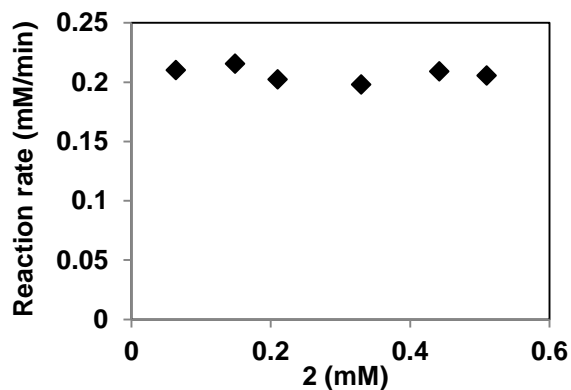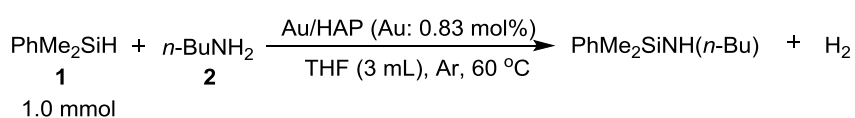
1   **2**
1.0 mmol

Figure 4-5. Dependency on the concentration of **2**

97

Next, a kinetic isotope effect was investigated in the oxidation coupling of **1** with **2**. When using D-labeled **1** (PhMe$_2$SiD), the initial production rate of **3** was slow (k_H/k_D = 1.5) (Figure 4-6), suggesting that the rate-determining step is the activation step of the Si–H bond of **1** by Au nanoparticles.
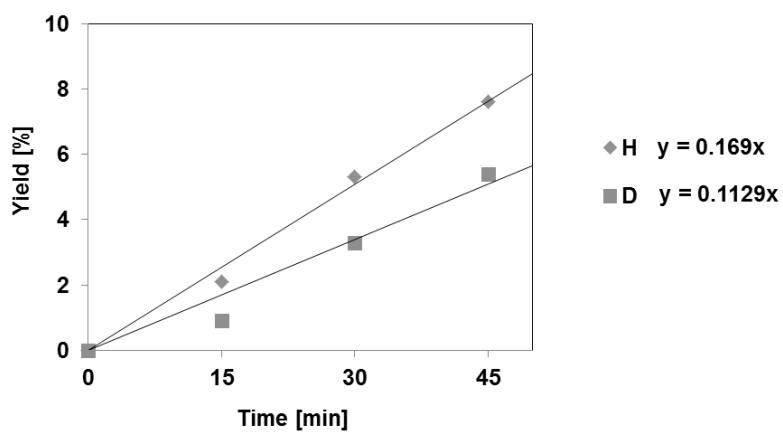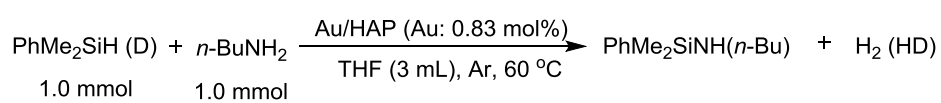
PhMe$_2$SiH (D) + *n*-BuNH$_2$ $\xrightarrow[\text{THF (3 mL), Ar, 60 °C}]{\text{Au/HAP (Au: 0.83 mol\%)}}$ PhMe$_2$SiNH(*n*-Bu) + H$_2$ (HD)

1.0 mmol 1.0 mmol

Figure 4-6. Kinetic isotope effect

In a separate experiment, the scrambling test was performed (Figure 4-7). The peaks attributed to Si-H bonds of PhMe$_2$SiH and n-Bu$_3$SiH were observed at 4.38 ppm and 3.74 ppm, respectively (Figure 4-7, a). In the mixture of PhMe$_2$SiD and n-Bu$_3$SiH, the peak originated from PhMe$_2$SiH was not detected (Figure 4-7, b). Interestingly, the treatment of an equimolar mixture of PhMe$_2$SiD and n-Bu$_3$SiH in the presence of Au/HAP in THF under Ar at 60 °C provided HD-scrambled PhMe$_2$SiH and n-Bu$_3$SiD (Figure 4-7, c) whereas no formation of the HD-scrambled hydrosilanes was confirmed in the absence of Au/HAP (Figure 4-7, d), clearly showing that Si–H bond cleavage occurred on Au nanoparticles. Furthermore, Kaneda *et al.* reported that the activation of the Si−H bond of **1** by Au nanoparticles was also confirmed by a Fourier transform infrared study [33]. They demonstrated that when **1** adsorbed on the Au nanoparticle surface, the peak attributed to the Si-H bond of **1** shifted to 2096 cm^{-1} from 2128 cm^{-1}. This redshift of the peaks originated in the Si-H bond vibration indicated that Au nanoparticles could activate the Si-H bond of **1**. From these results, the coupling reaction may occur as follows (Figure 4-8). First, a cleavage of Si-H bond of a hydrosilane adsorbed on Au/HAP by the Au atom occurs. Next, nucleophilic attack of an amine to the electrophilic Si atom bound on the Au atom gives the corresponding silylamine together with generation of H$_2$.

a) PhMe$_2$SiH + Bu$_3$SiH
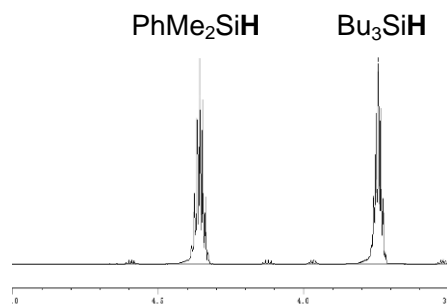
PhMe$_2$Si**H**   Bu$_3$Si**H**
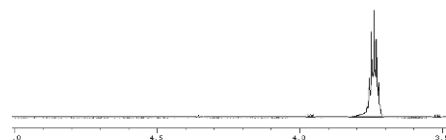
b) PhMe$_2$SiD + Bu$_3$SiH

c) PhMe$_2$SiD + Bu$_3$SiH in the presence of Au/HAP after stirring for 1 h at 60 °C
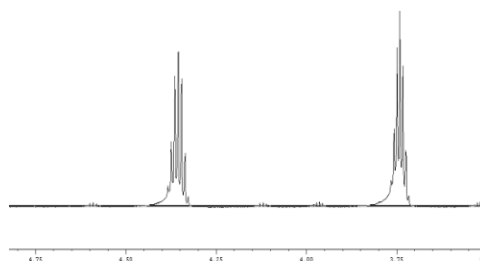
d) PhMe$_2$SiD + Bu$_3$SiH in the presence of HAP after stirring for 1 h at 60 °C
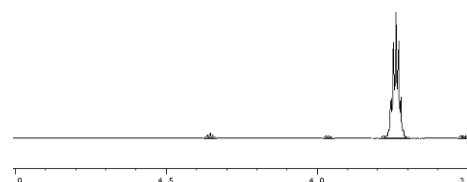
Figure 4-7. NMR spectra of hydrosilane mixtures. (a) PhMe$_2$SiH+Bu$_3$SiH, (b) PhMe$_2$SiD+Bu$_3$SiH, (c) PhMe$_2$SiD+Bu$_3$SiH in the presence of Au/HAP after stirring 1 h at 60 °C, (d) PhMe$_2$SiD+Bu$_3$SiH in the presence of HAP after stirring for 1 h at 60 °C.
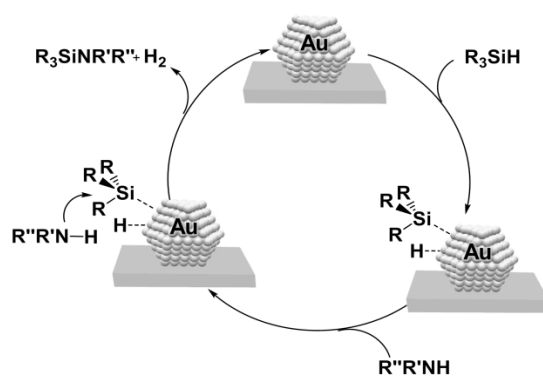
Figure 4-8. Plausible reaction mechanism

4. Conclusion

It was disclosed that hydroxyapatite-supported Au nanoparticles acted as a highly efficient catalyst for the selective coupling of hydrosilanes with amines and amides. A wide range of silylamines and silylamides were obtained in good to excellent yields, in which only an equimolar ratio of hydrosilanes to amines or amides could be utilized. This catalyst system provided a simple, efficient and sustainable protocol for the synthesis of various silylamines and silylamides.

5. References

[1] C. A. Roth, *Ind. Eng. Chem. Prod. Res. Develop.* **1972**, *11*, 134-139.

[2] T. P. Mawhinney, M. A. Madson, *J. Org. Chem*. **1982**, *47*, 3336-3339.

[3] D. A. Armitage, *The Silicon-Heteroatom Bond*, *Wiley:* Chichester, **1991**, 365-484.

[4] Y. Tanabe, M. Murakami, K. Kitaichi, Y. Yoshida, *Tetrahedron Lett.* **1994**, *35*, 8409-8412.

[5] Y. Tanabe, T. Misaki, M. Kurihara, A. Iida, Y. Nishii, *Chem. Commun*. **2002**, 1628-1629.

[6] A. Iida, A. Horii, T. Misaki, Y. Tanabe, *Synthesis* **2005**, *16*, 2677-2682.

[7] J. A. Hardwick, L. C. Pavelka, K. M. Baines, *Dalton Trans*. **2012**, *41*, 609-621.

[8] E. Larsson, R. Marin, *Acta Chemica Scandinavica* **1951**, *5*, 1173-1178.

[9] R. Fessenden, J. S. Fessenden, *Chem. Rev.* **1961**, *61*, 361-388.

[10] L. H. Sommer, J. D. Citron, *J. Org. Chem*. **1967**, 2470-2472.

[11] K. Yamamoto, M. Takemae, *Bull. Chem. Soc. Jpn*. **1989**, 2111-2113.

[12] E. Matarasso-Tchiroukhine, *J. Chem. Soc., Chem. Commun*. **1990**, 681-682.

[13] H. Q. Liu, J. F. Harrod, *Can. J. Chem*. **1992**, *70*, 107-110.

[14] K. Takaki, T. Kamata, Y. Miura, T. Shishido, K. Takehira, *J. Org. Chem*. **1999**, *64*, 3891-3895.

[15] J. X. Wang, A. K. Dash, J. C. Berthet, M. Ephritikhine, M. S. Eisen, *J. Organomet. Chem.* **2000**, *610*, 49-57.

[16] F. Buch, S. Harder, *Organometallics* **2007**, *26*, 5132-5135.

[17] D. V. Gutsulyak, S. F. Vyboishchikov, G. I. Nikonov, *J. Am. Chem. Soc*. **2010**, *132*, 5950-5951.

[18] J. F. Dunne, S. R. Neal, J. Engelkemier, A. Ellern, A. D. Sadow, *J. Am. Chem. Soc*. **2011**, *133*, 16782-16785.

[19] C. K. Toh, H. T. Poh, C. S. Lim, W. Y. Fan, *J. Organomet. Chem*. **2012**, *717*, 9-13.

[20] W. Xie, H. Hu, C. Cui, *Angew. Chem. Int. Ed*. **2012**, *51*, 11141-11144.

[21] C. D. F. Königs, M. F. Müller, N. Aiguabella, H. F. T. Klare, M. Oestreich, *Chem. Commun.*

2013, *49*, 1506-1508.

[22] M. S. Hill, D. J. Liptrot, D. J. MacDougall, M. F. Mahon, T. P. Robinson, *Chem. Sci*. **2013**, *4*, 4212-4222.

[23] M. Paul, E. Frainnet, *C. R. Acad. Sc. Paris* **1974**, *279*, 213-216.

[24] W. Suchanek, Y. Masahiro, *J. Mater. Res.* **1988**, *13*, 94-117.

[25] M. Vallet-Regi, *J. Chem. Soc. Dal. Trans.* **2001**, *2*, 97-108.

[26] C. S. Ciobanu, S. L. Iconaru, C. Popa, A. Costesca, M. Motelica-Heino, D. Predoi, *J. Nanometer.* **2014**, Article ID 361061.

[27] D. Manatunga, C. Danushika, R. M. de Silva, K. M. N. de Silva, R. Ratnaweera, *RSC Adv*. **2016**, *6*, 105618-105630.

[28] J. F. Cawthray, A. L. Creagh, C. A. Haynes, C. Orving, *Inorg. Chem*. **2015**, *54*, 1440-1445.

[29] K. Kaneda, T. Mizugaki, *Ener. Environ. Sci.* **2009**, *2*, 655-673.

[30] M. Gruselle, *J. Organimet. Chem.* **2015**, *793*, 93-101.

[31] T. Mitsudome, A. Noujima, T. Mizugaki, K. Jitsukawa, K. Kaneda, *Chem. Commun*. **2009**, 5302-5304.

[32] T. Mitsudome, S. Arita, H. Mori, T. Mizugaki, K. Jitsukawa, K. Kaneda, *Angew. Chem. Int. Ed*. **2008**, *47*, 7438-7440.

[33] T. Mitsudome, Y. Yamamoto, A. Noujima, T. Mizugaki, K. Jitsukawa, K. Kaneda, *Chem. Eur. J.* **2013**, *19*, 14398-14402.

[34] L. Nie, J. Yu, M. Jaroniec, F. F. Tao, *Catal. Sci. Technol.* **2016**, *6*, 3649-3669.

[35] T. Mitsudome, Y. Mikami, K. Ebata, T. Mizugaki, K. Jitsukawa, K. Kaneda, *Chem. Commun*. **2008**, 4804-4806.

[36] H. Q. Liu, J. F. Harrod, *Organometallics* **1992**, *11*, 822-827.

Chapter V.

O$_2$-Enhanced Catalytic Activity of Gold Nanoparticles
in Dehydrogenative Coupling of Hydrosilanes with Water to Silanols

1. Introduction

Silanols are valuable building blocks for silicon-based polymeric materials [1-4] and nucleophilic coupling partners in organic synthesis [5-8]. Previously, silanols have been synthesized by hydrolysis of chlorosilanes with water in the presence of bases [9, 10] or oxidation of hydrosilanes using stoichiometric oxidants [11-16]. However, the hydrolysis of chlorosilanes would produce siloxanes (Si-O-Si compound) [9, 10], causing low selectivity for the corresponding silanols, and stoichiometric reagents would produce a large amount of hazardous chemical wastes [11-16].

Recently, dehydrogenative coupling of hydrosilanes with water, that is, catalytic oxidation of hydrosilanes to silanols using water as a green oxidant has attracted much attention as a promising alternative to the traditional synthesis methods (Scheme 5-1). To date, various homogeneous and heterogeneous catalysts have been reported [17-23]. Mizuno *et al.* reported that TBA$_8$[Ag$_4$(γ-H$_2$SiW$_{16}$O$_{36}$)$_2$] promoted the reaction and showed high catalytic activity (TOF= 27000, TON = 15625) [21]. However, the developed Ag catalyst would yield a small amount of undesired siloxane as the by-product. Park *et al.* revealed that boehmite-supported Pd nanoparticles acted as effective heterogeneous catalysts for this reaction [20], whereas this Pd nanoparticle catalyst has suffered from low chemoselectivity, that is, alkenyl group of substrates were hydrogenated with *in-situ* generated H$_2$ species during the reaction.
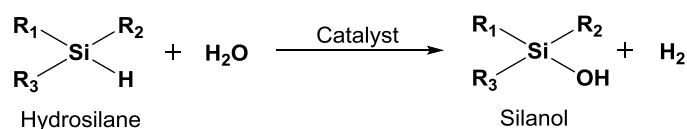
Scheme 5-1. Catalytic oxidation of hydrosilanes with water

K. Kaneda *et al.* first reported that Au nanoparticles are capable of promoting the aqueous oxidation of hydrosilanes to silanols [24]. The Au nanoparticle-catalyzed oxidation has since been explored by other researchers with respect to size and shape of the Au nanoparticles [25-30] and these developed catalysts show high activities for various hydrosilanes. For example, H. Duan *et al.* reported that poly(1-(4-vinylbenzyl)-3-methylimidazolium chloride)-branched SBA-15 (SBA-PIL)-supported Au catalyst effectively promoted the reaction of various less bulky hydrosilanes [29]. E. Doris *et al.* demonstrated that carbon nanotube-supported Au nanoparticles (AuCNTs) showed relatively high catalytic activity and excellent selectivity (TOF = 12000, TON = 72000) without by-production of siloxanes. However, the developed Au nanoparticle catalyst systems still suffer from low catalytic performance for bulky hydrosilanes, where poor yields of the corresponding silanols are often obtained [29] or high loading of Au nanoparticles is required to achieve high yields [25, 30]. Therefore, the development of Au nanoparticle catalyst systems with high catalytic activity for bulky hydrosilanes is still a challenging issue.

This chapter presents that molecular oxygen (O_2) is found to act not as a stoichiometric oxidizing reagent but as a non-consumed activator for Au nanoparticles, significantly boosting the catalytic activity of hydroxyapatite-supported Au nanoparticles in the dehydrogenative coupling of hydrosilanes with water. Diverse hydrosilanes including bulky hydrosilanes are transformed to the corresponding silanols in high yields with high efficiencies. Moreover, the developed catalyst is recoverable and reusable without the loss of its activity and selectivity.

2. Experiment section

2-1. General

All organic reagents were purified before use. $HAuCl_4 \cdot xH_2O$ was obtained from Mitsuwa Chemicals Co., Ltd., and HAP (Apatite HAP, monoclinic) was purchased from Wako Pure Chemical

Co., Ltd. GC-FID and GC-MS were performed on a Shimadzu GC-2014 instrument equipped with a OV-17 column (3 m) and a GCMS-QP2010 SE instrument equipped with an Inert Cap WAX-HT capillary column (30 m × 0.25 mm i.d., 0.25 μm), respectively. Gas phase analysis was done with an on-line quadrupole mass spectrometer (BELMass-S, BEL Japan, Inc.). ^{1}H and ^{13}C nuclear magnetic resonance (NMR) spectra were recorded on a JEOL JNM-ESC400 spectrometer and the chemical shifts are reported in ppm from TMS as a reference. Transmission electron microscopy (TEM) observations were carried out using a FEI Tecnai G2 20ST instrument operated at 200 kV.

2-2. Preparation of Au catalysts

Au catalysts were prepared according to previously reported method [24]. Support (1.0 g) was added to 50 mL of aqueous solution of $HAuCl_4$ (2 mM). Then, 0.2 mL of aqueous NH_3 (10%) was added and the resulting mixture was stirred at room temperature for 12 h. The obtained slurry was filtered, washed with deionized water, and then dried at room temperature *in vacuo*. Subsequently, the obtained yellow powder was added to 50 mL of an aqueous solution of KBH_4 (18 mM) and stirred at room temperature for 1 h to yield supported Au catalysts.

2-3. Characterization of Au/HAP

TEM confirmed that Au nanoparticles with a mean diameter of 3 nm were highly dispersed on the surface of HAP (Figure 5-1).
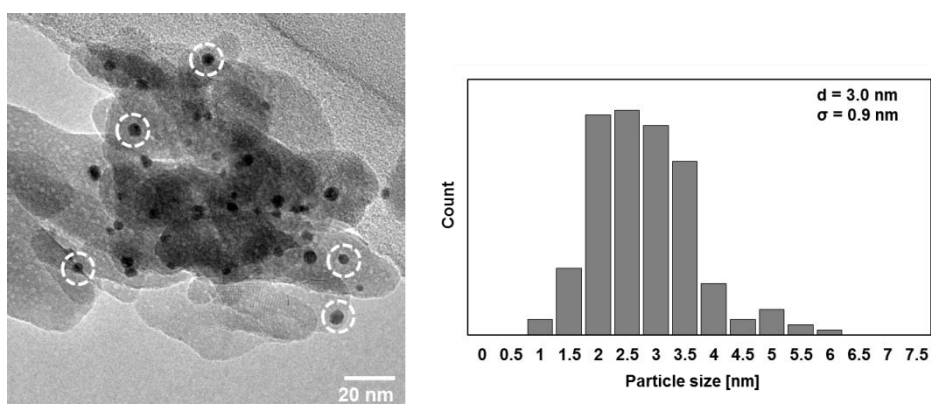

Figure 5-1. TEM image of Au/HAP and its size distribution histogram.

2-4. Typical reaction procedure

A typical reaction procedure for the aqueous oxidation of tri(iso-butyl)silane (**1**) to tri(iso-butyl)silanol (**2**) using Au/HAP was as follows. Au/HAP (0.005 g, Au: 0.0415 mol%) was placed in a reaction vessel, followed by the addition of acetone (4 mL), water (0.1 mL), and **1** (1 mmol). The reaction mixture was vigorously stirred at 30 °C under O_2 atmosphere for 7 min. Au/HAP was filtered and the yield was determined by GC analysis. The product was isolated by Kugelrohr distillation.

2-5. Measurement of H_2

The amount of H_2 generated during the reaction was measured by GC-TCD. The oxidation was carried out under standard reaction conditions in a closed vessel with on-line GC-TCD. After the reaction, the gas phase was subjected to GC-TCD for qualitative and quantitative analysis of H_2. Once the H_2 concentration in the headspace was determined, the quantity was simply multiplied by the total flask volume. GC conditions were as follows: GC with thermal conductivity detector (Shimadzu GC-8A); column: molecular sieves 13X (4.0 m); oven temperature: 40 °C; injection and detection temperature: 70 °C; carrier gas: Ar (100 kPa); current: 60 mA; retention time: H_2 (5.3 min).

2-6. Large-scale reaction

A large-scale reaction was performed under O_2 bubbling for 7 h. After the reaction, Au/HAP was filtered and the yield was determined by GC analysis. The product was isolated by Kugelrohr distillation.

2-7. Dehydrogenative coupling of 1 with water using Au/HAP under controlled introduction and removal of air

The dehydrogenative coupling reaction was carried out under standard reaction conditions in a closed vessel with on-line GC-TCD. Initially, Au/HAP was used in the reaction of **1** at 30 °C in air. After 10 min, the reaction vessel was frozen into liquid nitrogen, then the amount of H_2

generated during the reaction was measured by GC-TCD. Next, the reaction vessel was closed under

vacuum and then Ar was introduced into the reaction vessel. After the reaction mixture was thawed,

the reaction was re-started at 30 °C for 10 min. These handlings were repeated with switching of the

atmosphere to complete the coupling reaction.

2-8. Product identification

The products were characterized by GC, GC-MS, and NMR. Retention times (GC) and

chemical shifts (^{1}H and ^{13}C NMR) of the products were in agreement with those of authentic

samples or previously reported values.

Triisobutylsilanol: CAS registry No. [317374-14-4] (Table 5-1)

^{1}H NMR (400 MHz, CDCl$_3$): δ 1.84 (m, 3H), 1.31 (br s, 1H), 0.98 (d, J = 7.2 Hz, 18H), 0.62 (d, J =

6.8 Hz, 6H). ^{13}C NMR (100 MHz, CDCl$_3$): δ 27.4, 26.8, 26.4, 24.3. [1]

Triisopropylsilanol: CAS registry No. [17877-23-5] (Table 5-2, Entry 4)

^{1}H NMR (400 MHz, CDCl$_3$): δ 1.07 (m, 21H). ^{13}C NMR (100 MHz, CDCl$_3$): δ 17.7, 12.3.

Triphenylsilanol: CAS registry No. [791-31-1] (Table5- 2, Entry 5)

^{1}H NMR (400 MHz, CDCl$_3$): δ 7.58-7.71 (m, 6H), 7.33-7.51 (m, 9H), 2.50 (br s, 1H). ^{13}C NMR

(100 MHz, CDCl$_3$): δ 134.0, 130.1, 127.9.

_t_-Butyldiphenylsilanol: CAS registry No. [93547-88-7] (Table 5-2, Entry 6)

^{1}H NMR (400 MHz, CDCl$_3$): δ 7.68-7.73 (m, 2H), 7.33-7.43 (m, 3H), 1.06 (s, 9H). ^{13}C NMR (100

MHz, CDCl$_3$): δ 135.1, 134.7, 129.6, 127.7, 25.6, 19.0.

_t_-Butyldimethylsilanol: CAS registry No. [18173-64-3] (Table 5-2, Entry 7)

^{1}H NMR (400 MHz, CDCl$_3$): δ 0.93 (s, 9H), 0.11 (s, 6H). ^{13}C NMR (100 MHz, CDCl$_3$): δ 25.6, 18.0,

-3.6.

Dimethylphenylsilanol: CAS registry No. [5272-18-4] (Table 5-2, Entry 8)

^{1}H NMR (400 MHz, CDCl$_3$): δ 7.68-7.73 (m, 2H), 7.33-7.43 (m, 3H), 0.26 (s, 6H). ^{13}C NMR (100

MHz, CDCl$_3$): δ 135.1, 134.7, 129.6, 127.7, 19.0, -1.0.

Benzyldimethylsilane: CAS registry No. [56633-16-0] (Table 5-2, Entry 9)

^{1}H NMR (400 MHz, CDCl$_3$): δ 7.19-7.31 (m, 2H), 7.03-7.11 (m, 3H), 0.14 (s, 6H). ^{13}C NMR (100

MHz, CDCl$_3$): δ 139.7, 129.1, 128.8, 124.9, 28.7, 0.0.

Diphenylsilanediol: CAS registry No. [947-42-2] (Table 5-2, Entry 10)

^{1}H NMR (400 MHz, CDCl$_3$): δ 7.65-7.77 (m, 4H), 7.32-7.46 (m, 6H), 3.32 (s, 2H). ^{13}C NMR (100

MHz, CDCl$_3$): δ 137.6, 134.0, 129.2, 127.3.

Methylphenylsilanediol: CAS registry No. [3959-13-5] (Table 5-2, Entry 11)

^{1}H NMR (400 MHz, CDCl$_3$): δ 7.52-7.66 (m, 2H), 7.26-7.40 (m, 3H), 0.28 (s, 3H). ^{13}C NMR (100

MHz, CDCl$_3$): δ 136.0, 133.6, 130.2, 128.0, -1.7.

3. Results and Discussion

Toward an efficient heterogeneous Au nanoparticle catalyst system for the aqueous oxidation of hydrosilanes to silanols, atmospheric effect was investigated. The result is summarized in Table 5-1. In Ar atmosphere, the oxidation of tri(iso-butyl)silane (**1**) gave tri(iso-butyl)silanol (**2**) with 99% yield in 8 h together with the generation of equimolar amounts of H_2 (Table 5-1, Entry 1). It was notable that the catalytic activity of Au/HAP significantly increased under air atmosphere, and then the quantitative oxidation of **1** was completed within 10min (Table 5-1, Entry 2). To investigate the effect of air atmosphere in details, the oxidation was carried out under various atmospheric conditions such as O_2, CO_2, N_2, and H_2 (Table 5-1, Entries 3 and 6-8). Among the conditions tested, O_2 atmosphere was highly effective to afford **2** in quantitative yield (Table 5-1, Entry 3), while CO_2, N_2, and H_2 atmosphere did not influence the catalytic performance of Au/HAP, resulting in yields of **2** similar to that under Ar (Table 5-1, Entries 6-8 vs. 9). When comparing the catalytic activity of

Table 5-1. Aqueous oxidation of **1** using Au/HAP under various

$$^i\text{Bu}_3\text{SiH (}\mathbf{1}\text{)} + \text{H}_2\text{O} \xrightarrow{\text{Au/HAP}} {}^i\text{Bu}_3\text{SiOH (}\mathbf{2}\text{)} + \text{H}_2$$

Entry	Atmosphere	Time	Yield of **2** [%][b]
1	Ar	8 h	>99
2	air	10 min	>99
3	O_2	10 min	>99
4[c]	O_2	10 min	0
5[d]	O_2	10 min	0
6	CO_2	10 min	13
7	N_2	10 min	11
8	H_2	10 min	11
9	Ar	10 min	11
10[e]	O_2	7 min	>99
11[e]	Ar	7 min	0.5

[a]Reaction conditions: **1** (1 mmol), Au/HAP (0.05 g, Au: 0.4 mol%), water (10 eqv.), acetone (4 mL), 30 ^{o}C. [b]Determined by GC using an internal standard technique. [c]The use of HAP instead of Au/HAP. [d]In the absence of Au/HAP. [e]Au/HAP 0.005 g (Au: 0.04 mol%)

Au/HAP in O_2 with Ar atmosphere using the same reaction time with lower catalyst loading (0.04 mol%), the impact of O_2 was more pronounced. A quantitative yield of **2** was obtained in the presence of O_2, whereas Ar atmosphere gave **2** in 0.5% yield (Table 5-1, Entry 10 vs. 11), demonstrating an acceleration effect of 200 times the reaction rate by O_2 relative to Ar atmosphere. In addition, neither the use of HAP nor the absence of Au/HAP catalyzed the oxidation in O_2 atmosphere (Table 5-1, Entries 4 and 5). These results clearly showed the high efficiency of O_2, drastically enhancing the catalytic activity of Au nanoparticles.

Effects of solvents, supports and particle sizes of Au nanoparticles on the catalysis in the aqueous oxidation of **1** were investigated (Table 5-2). In the acetone solvent, the oxidation of **1** proceeded more smoothly than in other solvents such as acetonitrile, ethyl acetate, THF and water (Entry 1 vs. 2-5). Among the various supports tested, it was clear that HAP was the best support for this reaction (Entry 1 vs. 6-9). This prominent catalytic activity of Au/HAP may be due to the strong adsorption ability of HAP for hydrosilanes as mentioned in Chapter IV. The size effect of Au nanoparticles was also studied using Au/HAP having different Au particle sizes, confirming that

Table 5-2. Optimization of reaction conditions[a]

$${}^{i}Bu_3SiH\ (\textbf{1}) + H_2O \xrightarrow{\text{Au catalyst}} {}^{i}Bu_3SiOH\ (\textbf{2}) + H_2$$

Entry	Catalyst	d [nm]	Solvent	Yield of 2 [%][b]
1	Au/HAP	3.0	acetone	>99
2	Au/HAP	3.0	acetonitrile	71
3	Au/HAP	3.0	ethyl acetate	67
4	Au/HAP	3.0	THF	38
5	Au/HAP	3.0	water	34
6	Au/TiO$_2$	3.6	acetone	48
7	Au/SiO$_2$	3.6	acetone	41
8	Au/MgO	2.2	acetone	22
9	Au/Al$_2$O$_3$	3.1	acetone	20
10	Au/HAP	5.7	acetone	52
11	Au/HAP	6.5	acetone	43

[a]Reaction conditions: **1** (1 mmol), Au catalyst (Au: 0.04 mol%), water (10 eqv.), solvent (4 mL), 30 $^{\circ}$C, 10 min.
[b]Determined by GC using an internal standard technique.

smaller Au nanoparticles provided higher catalytic activities (Entry 1 vs. 10, 11).

The high efficiency of O_2 was also demonstrated in the aqueous oxidation of various silanes (Table 5-3). Typically, less-reactive bulky silanes were converted to the corresponding silanols in excellent yields with low catalyst loading (Entries 4-6). Furthermore, the Au/HAP-O_2 catalytic system was applicable to the gram-scale synthesis of silanol. For example, 6.97 g of dimethylphenylsilane was successfully transformed to dimethylphenylsilanol in 99% isolated yield

Table 5-3. Aqueous oxidation of various hydrosilanes using Au/HAP[a]

$$R_1R_2R_3SiH + H_2O \xrightarrow{\text{Au/HAP}} R_1R_2R_3SiOH + H_2$$

| Entry	Substrate	Product	Time [min]	Yield [%][b]
1	*i*-Bu⎯Si⎯H (*i*-Bu)	*i*-Bu⎯Si⎯OH (*i*-Bu)	7	>99
2[c]	*i*-Bu Si⎯H	*i*-Bu Si⎯OH	7	>99[e]
3[d]	*i*-Bu	*i*-Bu	7	>99[e]
4	*i*-Pr·Si⎯H (*i*-Pr, *i*-Pr)	*i*-Pr·Si⎯OH (*i*-Pr, *i*-Pr)	80	>99
5	Ph⎯Si⎯H (Ph, Ph)	Ph⎯Si⎯OH (Ph, Ph)	30	>99
6	*t*-Bu·Si⎯H (Ph, Ph)	*t*-Bu·Si⎯OH (Ph, Ph)	480	>99
7	*t*-Bu·Si⎯H (Me, Me)	*t*-Bu·Si⎯OH (Me, Me)	5	>99
8	Ph⎯Si⎯H (Me, Me)	Ph⎯Si⎯OH (Me, Me)	5	>99
9	Ph⁀Si⎯H (Me)	Ph⁀Si⎯OH (Me)	6	>99
10	Ph⎯Si⎯Ph (H, H)	Ph⎯Si⎯Ph (OH, OH)	20	>99
11	Me·Si·Ph (H, H)	Me·Si·Ph (OH, OH)	20	>99

[a]Reaction conditions: Au/HAP (0.0050 g, Au: 0.04 mol%), hydrosilane (1 mmol), water (10 eqv.), acetone (4 mL), 30 °C, O_2 (1 atm). [b]Isolated yields. [c]Reuse 1. [d]Reuse 2. [e]Determined by GC using an internal standard technique.

114

(7.77 g), where the turnover frequency (TOF) and turnover number (TON) reached 175900 and 1230000, respectively (Scheme 5-2). These values are 12 orders of magnitude greater than those in previously reported homogeneous and heterogeneous catalyst systems; for example, $TBA_8[Ag_4(\gamma-H_2SiW_{16}O_{36})_2]$ (TOF= 27000, TON = 15625) [21], Pd/C (20000, 99000) [20], Pd/AlO(OH) (20000, 99000) [22], and AuCNT nanohybrid (12000, 72000) [26].
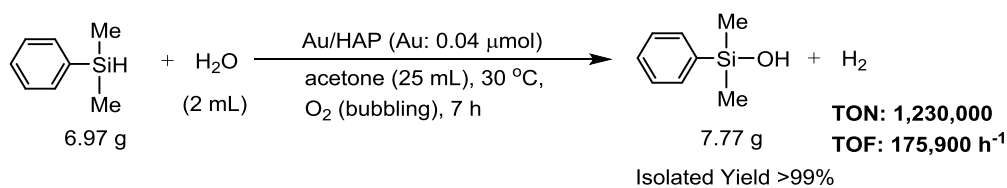
Scheme 5-2. Gram-scale oxidation using Au/HAP-O_2 catalytic system

After the reaction, Au/HAP was separable from the reaction mixture and reusable without loss of its activity or selectivity (Table 5-3, Entries 2 and 3). Inductively coupled plasma (ICPAES) analysis showed the absence of Au species in the filtrate, revealing that no leaching occurred during the reaction. Furthermore, the image of Au/HAP after the reuse showed that no aggregation of Au nanoparticles occurred and that the average diameters of the reused Au nanoparticles were similar to those of the fresh ones (Figure 5-2).

Figure 5-2. TEM image of Au/HAP after reuse and its size distribution histogram
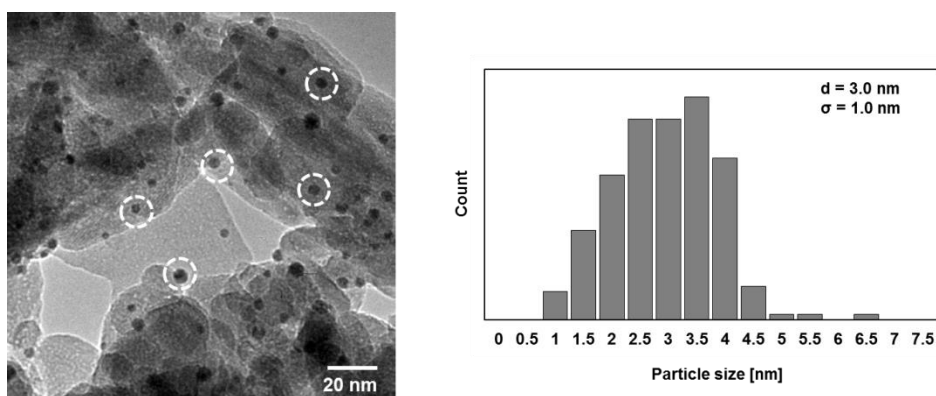
To investigate the role of O_2, the time courses of the Au/HAP-catalyzed oxidation of **1** with water and generation of H_2 were monitored by GC-TCD under controlled air or Ar atmosphere (Figure 5-3). By introducing air, the reaction rate was significantly increased compared to that under Ar atmosphere. Interestingly, this performance was repeatable during the oxidatoin, responding to the introduction and removal of air. This repeatable performance of Au/HAP is much different from Pd/C with surface oxygen adatoms in the oxidation of silanes reported in [20] and [31]; The catalytic activity of the oxygen-preadsorbed Pd/C catalyst under N_2 flow was similar to that in the presence of O_2, and zero-order dependency of O_2 on the reaction rate was shown. Moreover, it is notable that quantitative analysis of H_2 and O_2 revealed that equimolar amounts of H_2 to **2** were generated during the aerobic reaction conditions, while O_2 was not consumed. Furthermore, this repeatability indicated the reversible action of O_2 on Au nanoparticles, where molecularly adsorbed O_2 species on Au nanoparticles would increase the catalytic activity. Additionally, the use of isotopic $H_2^{18}O$ under air atmosphere gave ^{18}O-labeled **2** in 98% yield with 99% selectivity (Figure 5-4), supporting that the oxygen atoms incorporated in silanol products were derived not from air (O_2) but water. These phenomena suggest that the O_2 in air did not act as a stoichiometric oxidizing reagent but played a key role as a non-consumed activator enhancing the catalytic activity of Au/HAP as like a ligand.
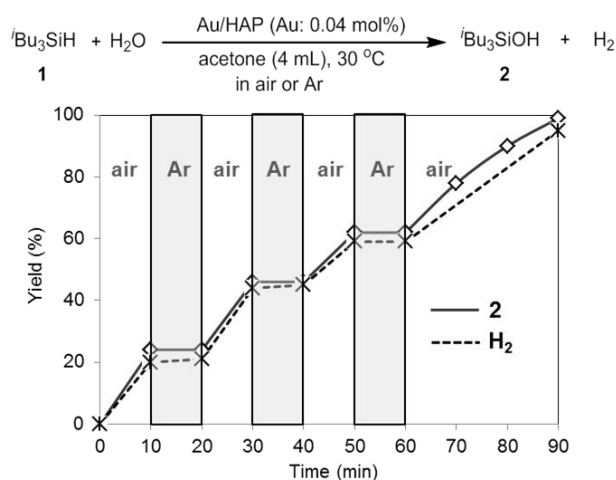

Figure 5-3. Time profile of the yield of **2** generation of H_2 under controlled air or Ar atmosphere

$$^iBu_3SiH + H_2{}^{18}O \xrightarrow[\text{acetone (4 mL), O}_2\text{ (1 atm), 30 }^\circ\text{C}]{\text{Au/HAP (Au:0.0415 mol\%)}} {}^iBu_3Si{}^{18}OH + H_2$$

Isolated yield 98%
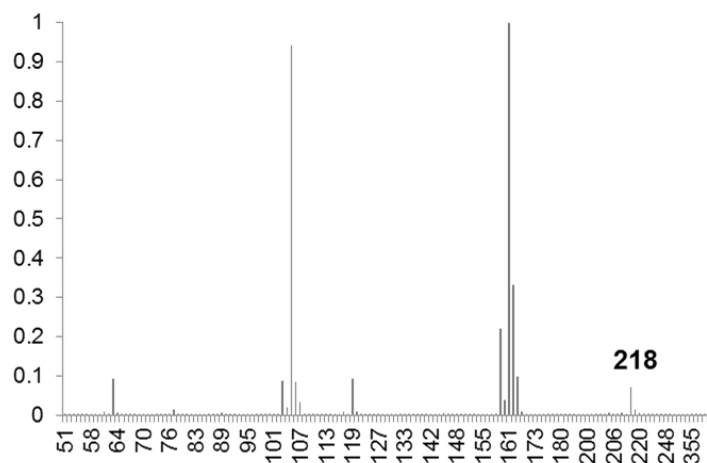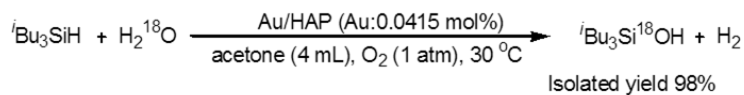
Figure 5-4. ^{18}O-labeling experiment

To understand the catalytic features of the Au/HAP-O_2 system, kinetic studies on the aqueous oxidation of dimethylphenylsilane using Au/HAP at 30 °C in air were performed. The initial production rate of dimethylphenylsilanol was proportional to the amount of dimethylphenylsilane (Figure 5-5), but independent of the concentration of water (Figure 5-6).

$$PhMe_2SiH + H_2O \xrightarrow[\text{acetone (4 mL), 30 }^\circ\text{C, 5 min}]{\text{Au/HAP (Au: 0.04 mol\%)}} PhMe_2SiOH + H_2$$

x mmol   0.1 mL

Figure 5-5. Dependency on the concentration of hydrosilanes

$PhMe_2SiH + H_2O \xrightarrow[\text{acetone (4 mL), 30 °C, 5 min}]{\text{Au/HAP (Au: 0.04 mol%)}} PhMe_2SiOH + H_2$

1 mmol   xx mL

Figure 5-6. Dependency on the concentration of water
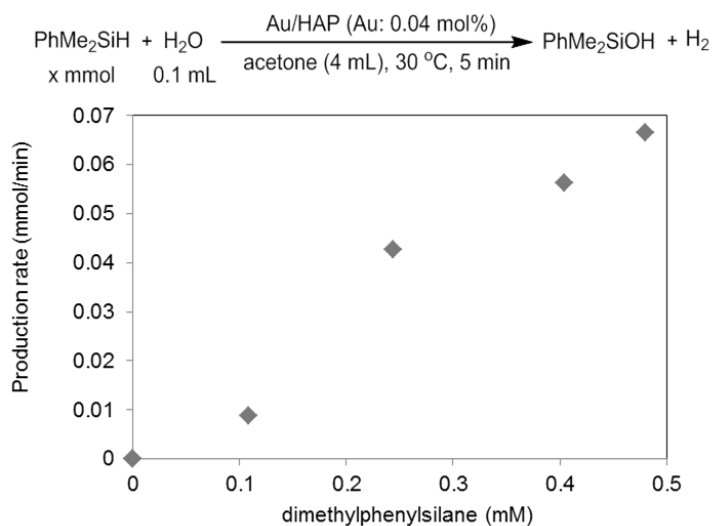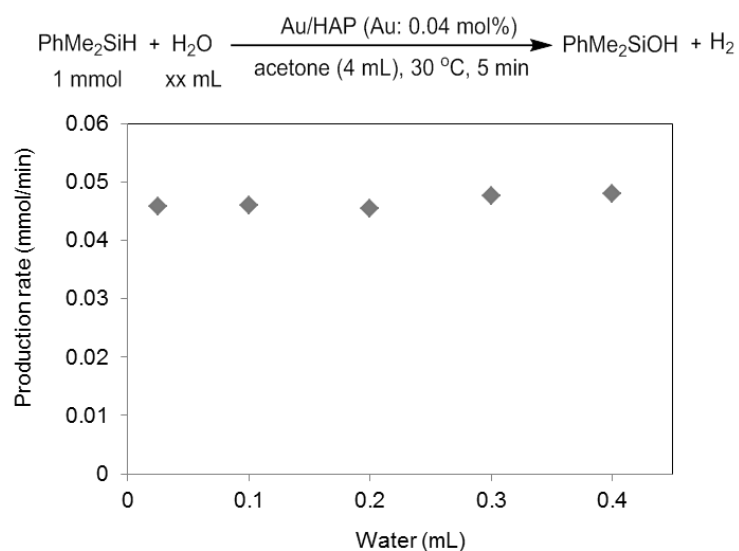
Next, a kinetic isotope effect was investigated in the aqueous oxidation of dimethylphenylsilane. When using D-labeled dimethylphenylsilane, the initial production rate of dimethylphenylsilanol was slow (k_H/k_D = 1.45) (Figure 5-7), suggesting that the rate-determining step was the activation of the Si-H bond by Au nanoparticles. The activation of the Si-H bond of hydrosilanes by Au nanoparticles was also confirmed by a Fourier transform infrared study [32]. They demonstrated that the peak attributed to the Si-H bond of **1** was shifted to the lower frequency side when **1** adsorbed on the Au surface. Furthermore, in the presence of O_2, this redshift became prominent. These results revealed that 1) the Si-H bond of **1** was activated by Au nanoparticles, and 2) O_2-adsorbed Au nanoparticles activated **1** more strongly.
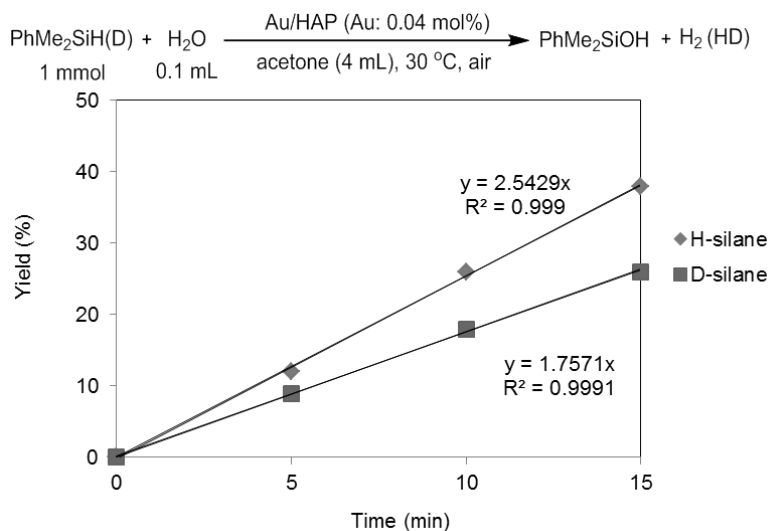
PhMe$_2$SiH(D) + H$_2$O $\xrightarrow[\text{acetone (4 mL), 30 °C, air}]{\text{Au/HAP (Au: 0.04 mol\%)}}$ PhMe$_2$SiOH + H$_2$ (HD)

1 mmol   0.1 mL

y = 2.5429x
R² = 0.999

y = 1.7571x
R² = 0.9991

◆ H-silane
■ D-silane

Yield (%)

Time (min)

Figure 5-7. Kinetic isotope effect

In a separate experiment, the aqueous oxidation of (R)-methyl-α-naphthylphenylsilane (ee = 80%) using Au/HAP gave (R)-methyl-α-naphthylphenylsilanol (ee = 80%) (Scheme 5-3), indicating that the configurational inversion of (R)-methyl-α-naphthylphenylsilane occurred at the silicon center. These results suggested that the reaction may occur through activation of the Si-H bond by Au nanoparticles, followed by the nucleophilic attack of a water molecule on the Si center from the backside of the Si on Au nanoparticles, giving the corresponding silanol together with the generation of H$_2$.

80% ee   80% ee
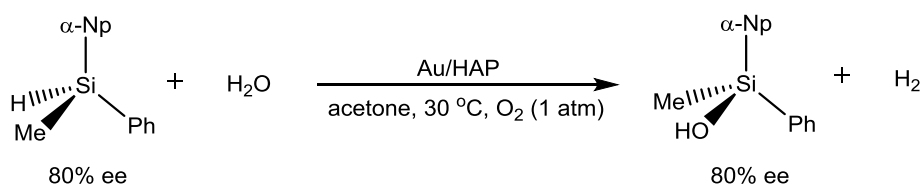
Scheme 5-3. Aqueous oxidation of an optically active hydrosilane

In consideration of O$_2$ reversibly acting on the Au nanoparticles as a non-consumed activator, adsorbed O$_2$ on Au nanoparticles may play an important role in the enhancement of Au/HAP activity. It is reported that O$_2$ adsorbed on Au clusters increases the electron deficiency of

the clusters through charge transfer from the Au clusters to O_2 [33]. From these results and previous report on the interaction between O_2 and Au, it can be said that O_2 would increase the electron deficiency of the Au nanoparticles through charge transfer from Au nanoparticles to O_2, enhancing the activity of Au nanoparticles for Si-H bond activation of hydrosilanes (Figure 5-8).
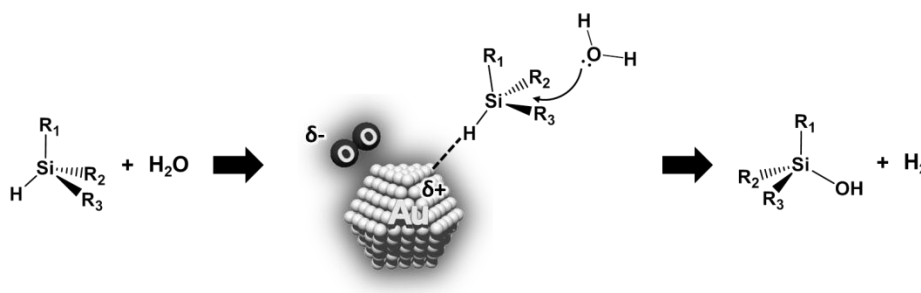

Figure 5-8. O_2-enhanced effect on Au nanoparticles for the oxidation of hydrosilanes

4. Conclusion

The author succeeded in the development of the Au/HAP-O_2 catalytic system for the highly efficient dehydrogenative coupling of hydrosilanes with water. Various silanes including less reactive bulky silanes could be converted to the corresponding silanols with low catalyst loading. The Au/HAP-O_2 catalyst system achieved excellent catalytic activity with a TON of over one million. In this catalytic system, O_2 acted not as a stoichiometric reagent but as a highly effective non-consumed activator for Au nanoparticles. The reversible action of O_2 on Au nanoparticles led to unique catalytic activity, spontaneously responding to the introduction and removal of air. This study reveals that O_2 is found to be a "*gas-ligand*" which significantly increases the catalytic activity of Au nanoparticles. This concept of atmospheric O_2 considered as a gas-ligand would be applicable to other metal nanoparticle-catalyzed molecular transformations under liquid-phase conditions.

5. References

[1] *Topics in Stereochemistry* (Eds: R. J. P. Corriu, C. Guérin, J. J. E. Moreau) John Wiley & Sons, New Jersey, **1984**, *15*, 43.

[2] *Advances in Inorganic Chemistry* (Eds: P. D. Lickiss) Academic Press, London, **1995**, *42*, 147.

[3] *The Chemistry of Organic Silicon Compounds* (Eds: Z. Rappoport, Y. Apeloig), John Wiley & Sons, New Jersey, **1998**, *2*, Chap. 29.

[4] *Silicon Reagents in Organic Synthesis* (Eds: E. W. Colvin), Academic Press, London, **1988**, 7.

[5] K. Hirabayashi, Y. Nishihara, A. Mori, T. Hiyama, *Tetrahedron Lett*. **1998**, *39*, 7893-896.

[6] K. Hirabayashi, J. Kawashima, Y. Nishihara, A. Mori, T. Hiyama, *Org. Lett*. **1999**, *1*, 299-302.

[7] S. E. Denmark, D. Wehrli, *Org. Lett*. **2000**, *2*, 565-568.

[8] K. Hirabayashi, A. Mori, J. Kawashima, M. Suguro, Y. Nishihara, T. Hiyama, *J. Org. Chem.* **2000**, *65*, 5342-5349.

[9] E. G. Rochow, W. F. Gilliam, *J. Am. Chem. Soc*. **1941**, *63*, 798-800.

[10] R. O. Sauer, *J. Am. Chem. Soc*. **1944**, *66*, 1707-1710.

[11] W. Adam, R. Mello, R. Curci, *Angew. Chem. Int. Ed.* **1990**, *29*, 890-891.

[12] L. H. Sommer, L. A. Ulland, G. A. Parker, *J. Am. Chem. Soc.* **1972**, *94*, 3469-3471.

[13] L. Spialter, L. Pazdernik, S. Bernstein, W. A. Swansiger, G. R. Buell, M. E. Freeburger, *J. Am. Chem. Soc.* **1971**, *93*, 5682-5686.

[14] P. D. Lickiss, R. Lucas, *J. Organomet. Chem*. **1996**, *521*, 229-234.

[15] S. M. Sieburth, W. Mu, *J. Org. Chem*. **1993**, *58*, 7584-7586.

[16] K. Hirabayashi, A. Mori, T. Hiyama, *Tetrahedron Lett.* **1997**, *38*, 461-464.

[17] K. Mori, M. Tano, T. Mizugaki, K. Ebitani, K. Kaneda, *New J. Chem.* **2002**, *26*, 1536-1538.

[18] E. Choi, C. Lee, Y. Na, S. Chang, *Org. Lett.* **2002**, *4*, 2369-2371.

[19] E. A. Ison, R. A. Corbin, M. M. Abu-Omar, *J. Am. Chem. Soc*. **2005**, *127*, 11938-11939.

[20] K. Shimizu, T. Kubo, A. Satsuma, *Chem. Eur. J.* **2012**, *18*, 2226-2229.

[21] Y. Kikukawa, Y. Kuroda, K. Yamaguchi, N. Mizuno, *Angew. Chem., Int. Ed*. **2012**, *51*, 2434-2437.

[22] M. Jeon, J. Han, J. Park, *ChemCatChem* **2012**, *4*, 521-524.

[23] M. Yu, H. Jing, X. Fu, *Inorg. Chem.* **2013**, *52*, 10741-10743.

[24] T.Mitsudome, A. Noujima, T. Mizugaki, K. Jitsukawa, K. Kaneda, *Chem. Commun*. **2009**, 5302-5304.

[25] N. Asao, Y. Ishikawa, N. Hatakeyama, Menggenbateer, Y. Yamamoto, M. Chen, W. Zhang, A. Inoue, *Angew. Chem. Int. Ed*. **2010**, *49*, 10093-10095.

[26] J. John, E. Gravel, A. Hagège, H. Li, T. Gacoin, E. Doris, *Angew. Chem., Int. Ed.* **2011**, *50*, 7533-536.

[27] W. Li, A. Wang, X. Yang, Y. Huang, T. Zhang, *Chem. Commun*. **2012**, *48*, 9183-9185.

[28] F. Mitschang, H. Schmalz, S. Agarwal, A. Greiner, *Angew. Chem., Int. Ed*. **2014**, *53*, 4972-4975.

[29] L. Ma, W. Leng, Y. Zhao, Y. Gao, H. Duan, *RSC Adv*. **2014**, *4*, 6807-6810.

[30] T. Liu, F. Yang, Y. Li, L. Ren, L. Zhang, K. Xu, X. Wang, C. Xu, J. Gao, *J. Mater. Chem. A* **2014**, *2*, 245-250.

[31] T. Kamachi, K. Shimizu, D. Yoshihiro, K. Igawa, K. Tomooka, K. Yoshizawa, *J. Phys. Chem. C* **2013**, *117*, 22967-2293.

[32] T. Mitsudome, Y. Yamamoto, A. Noujima, T. Mizugaki, K. Jitsukawa, K. Kaneda, *Chem. Eur. J.* **2013**, *19*, 14398-14402.

[33] H. Tsunoyama, N. Ichikuni, H. Sakurai, T. Tsukuda, *J. Am. Chem. Soc*. **2009**, *131*, 7086-7093.

Chapter VI.

Effective Hydrogen-Production through
Hydrolytic Oxidation of Hydrosilanes Catalyzed by Gold Nanoparticles

1. Introduction

Hydrogen (H_2) is one of the most promising energy carrier alternatives to fossil fuels. However, realizing a H_2-powered society is not so easy due mainly to problems related to the storage and transportation of H_2. To transport an adequate amount of H_2 gas for the utilization as the energy source, high capacity tank and large quantities of additional energy to pack the high pressure gas are indispensable. Furthermore, the resulting high-pressure gas tank are difficult to handle and potentially explosive. In this context, hydrogen storage materials such as metal hydrides and chemical hydrides attracted great attention for the convenient hydrogen transportation. Metal hydrides, such as $LiAlH_4$ and AlH_3, react violently when they contact water at ambient temperature, providing the rapid production of large amounts of pure H_2 [1-3]. However, these reactions are difficult to control and can result in an explosion. Chemical hydrides, such as ammonia-borane [4-6] and formic acid [7, 8], are leading candidates for new hydrogen storage materials because of their hydrogen content and highly efficient catalysts for producing H_2 from these molecules have been reported [9-23]. Laurenczy *et al*. revealed that the combination of $RuCl_3$ and water-soluble ligand, *meta*-trisulfonated triphenylphosphine, could act as a highly active catalyst for the decomposition of formic acid to generate H_2 and CO_2 under mild conditions [12]. This homogeneous system overcame catalyst deactivation induced by CO poisoning of metal actives sites through the suppression of CO by-production. Xu *et al*. demonstrated Pt nanoparticle catalyst showed higher activity for hydrolysis of ammonium borane than those of Pd, Ru, Au and Ag catalysts [15]. The Pt catalyst could generate H_2 gas even at room temperature along with the hydrolysis of ammonium borane. However, these catalysts often require anaerobic conditions [11, 12, 14, 15, 22] or heat energy especially in the case of formic acid decomposition [9, 10, 14]. In addition, these reactions can result in toxic ammonia salt and CO by-products, and the co-production of CO_2 gas from formic acid that requires a separation process using membranes to obtain pure H_2 gas, which limit their wide utilization for

124

producing H_2.

The preceding Chapter V revealed that hydroxylapatite-supported Au nanoparticles (Au/HAP) showed the highest activity for the oxidation of hydrosilanes among the previously reported catalysts and an equimolar amount of H_2 to that of silanols was generated during the oxidations [24]. From these results, the author conceived that the Au/HAP-catalyzed hydrolytic oxidation of silanes could be applied to an efficient H_2-production system at ambient temperature under aerobic conditions without additional energy input. Especially, polymethylhydrosiloxane ($Me_3Si(OSiMeH)_nOSiMe_3$, PMHS) and tetramethyldisiloxane ($Me_2SiHOSiHMe_2$, TMDS) would be the promising chemical hydrides leading to a cost-effective H_2-generation system. It is because they are by-products of the silicon industry [25, 26], thus, available and cheap. Additionally, the resulting silanols are useful as additives for silicon rubber [27, 28]. This chapter describes the development of an efficient controllable H_2-production system using hydrolytic oxidation of organosilanes with newly developed heterogeneous Au nanoparticle catalysts at ambient temperature under aerobic conditions. Furthermore, taking advantage of easy separable property of the heterogeneous Au catalyst, on-demand production of pure H_2 was attained by addition and removal of Au nanoparticle catalyst from the reaction mixture. In the case of hydrolytic silane-oxidation, the Au nanoparticle catalysts exhibited the highest turnover numbers and turnover frequencies of up to 3,333,000 and 77/sec, respectively. Moreover, the Au nanoparticle catalysts were reusable without loss of activity as demonstrated during recycling experiments.

2. Experimental section

2-1. General

The $HAuCl_4 \cdot xH_2O$ was obtained from Mitsuwa Chemicals Co., Ltd., and HAP (apatite HAP, monoclinic) was purchased from Wako Pure Chemical Co., Ltd. The GC-FID and GC-MS were performed on a Shimadzu GC-2014 instrument equipped with a Unisole-30T column and a

GCMS-QP2010 SE instrument equipped with an Inert Cap WAX-HT capillary column (30 m × 0.25 mm i.d., 0.25 μm. Gas-phase analysis was done with an on-line quadrupole mass spectrometer (BELMass-S, BEL Japan, Inc.). The ^{1}H and ^{13}C nuclear magnetic resonance (NMR) spectra were recorded on a JEOL JNM-ESC400 spectrometer and the chemical shifts reported in ppm from TMS as a reference. Transmission electron microscopy (TEM) observations were obtained using an FEI Tecnai G2 20ST instrument operated at 200 kV.

2-1. Preparation of catalysts

Au/HAP-NC (X wt%): Glutathione (1 mmol) was added to a methanol solution (50 mL) of HAuCl$_4$ (0.25 mmol) and stirred for 30 min at 273 K in air. Next, a methanol solution of KBH$_4$ (1.0 mmol) was added. After stirring 1 h at 273 K, the solid was collected by centrifugation and the precipitate re-dispersed in water (100 mL). Different amounts of HAP were added to the dispersion, followed by stirring for 4 h at r.t. The mixture then was filtered, washed with deionized water, and dried *in vacuo*. Finally, the obtained solid was calcined at 400 °C in air for 8 h to remove the glutathione coordinated to Au nanoparticles, giving Au/HAP-NC. The loading amount of Au X wt% is designated as Au/HAP-NC (X wt%).

Au/HAP: Supported gold nanoparticles were synthesized as follows [29]. The HAP (1.0 g) was soaked in 50 mL of an aqueous solution of HAuCl$_4$ (2 mM). After stirring for 2 min, 0.2 mL of aqueous NH$_3$ (10%) was added and the resulting mixture stirred at room temperature for 12 h in an air atmosphere. The obtained slurry was filtered, washed with deionized water, and then dried at room temperature *in vacuo*. Subsequently, the HAP solid containing Au ions was added to 50 mL of an aqueous solution of KBH$_4$ (18 mM) and stirred at room temperature for 1 h to yield Au/HAP as a purplish red powder.

2-3. Typical reaction procedure

A typical reaction procedure for oxidation of dimethylphenylsilane (**1**) to

dimethylphenylsilanol (**2**) using Au/HAP-NC (0.5 wt%) was as follows. The Au/HAP-NC (0.5 wt%) (0.01 g, Au: 0.05 mol%) was placed in a reaction vessel, followed by addition of DME (1 mL), water (0.2 mL), and **1** (1 mmol). The reaction mixture was stirred vigorously at 30 °C under an air atmosphere for 8 min. Then, the Au/HAP-NC (0.5 wt%) was filtered and the yield determined by GC analysis.

2-4. Large scale reaction

A large-scale reaction was performed under O_2 bubbling for 12 h. After the oxidation reaction, Au/HAP-NC was filtered and the yield determined by GC analysis. The product was isolated by Kugelrohr distillation.

2-5. Measurement of H_2

The amount of H_2 generated during the reaction was measured using the water displacement method. Qualitative analyses of generated gas were performed by GC-TCD. GC conditions were as follows: thermal conductivity detector (Shimadzu GC-8A); column: molecular sieves 13X (4.0 m); oven temperature: 40 °C; injection and detection temperature: 70 °C; carrier gas: Ar (100 kPa); current: 60 mA; retention time: H_2 (5.3 min).

2-5. Demonstration of on/off-switching of H_2 production by introduction and removal of Au/HAP-NC (0.5 wt%)

Demonstration of on/off-switching of H_2 production by introduction and removal of Au/HAP-NC (0.5 wt%). Reaction conditions: Au/HAP-NC (0.5 wt%) (1.0 g, Au: 0.025 mmol), TMDS (4.0 g), DME (20 mL), water (1.5 mL), air atmosphere.

2-6. Utilization of catalytic H2-generation system for portable fuel cell

Utilization of catalytic H_2-generation system for portable fuel cell. Module cell AF1FC_M was obtained from Aquafairy. Reaction conditions: Au/HAP-NC (0.5 wt%) (0.5 g, Au: 0.0125 mmol), TMDS (4.0 g), DME (20 mL), water (1.5 mL), air atmosphere.

2-7. Product identification

The products were characterized by GC, GC-MS, and NMR. Retention times (GC) and chemical shifts (^{1}H and ^{13}C NMR) of the products agreed with those of authentic samples or previously reported values.

Dimethylphenylsilanol: CAS registry No. [5272-18-4] (Table 1)

^{1}H NMR (400 MHz, CDCl$_3$): δ 7.54-7.62 (m, 2H), 7.32-7.36 (m, 3H), 0.39 ppm (s, 6H).

3. Results and Discussion

As was mentioned in Chapter V, the Au/HAP showed high catalytic activity at ambient temperature under aerobic conditions, producing pure H$_2$ during the reaction [24]. Thus, the author attempted to improve the catalytic activity of Au/HAP by decreasing the size of Au nanoparticles. The size-control synthesis of Au nanoparticles on HAP was performed using a modification of a previously reported method that used glutathione as a capping reagent for the Au nanoparticles [30-32]. Briefly, glutathione (1.0 mmol) was added to a methanol solution (50 mL) of HAuCl$_4$ (0.25 mmol) and stirred for 30 min at 273 K in air. Next, KBH$_4$ (1.0 mmol) was added to the solution. After stirring 1 h at 273K, the solid was collected by centrifugation and the precipitate was re-dispersed in water. Different amounts of HAP were added to this dispersion, followed by stirring for 4 h at r.t. The mixture was then filtered, washed with deionized water, and dried *in vacuo*. Finally, the solid obtained was calcined at 400 °C in air for 8 h to remove glutathione coordinated to Au nanoparticles, giving Au/HAP-NC. The loading amount of Au X wt% are designated as Au/HAP-NC (X wt%).

Representative images of Au/HAP-NC obtained by transmission electron microscopy (TEM) are depicted in Figure 6-1. Au nanoparticles in Au/HAP-NC (0.5 wt%), Au/HAP-NC (2 wt%), and Au/HAP-NC (3 wt%) had the mean diameters of 1.9 nm, 2.3 nm, and 3.1 nm, respectively, with

very narrow size-distributions (Figure 6-1, a-c), whereas Au/HAP prepared by the deposition–precipitation method showed a relatively broad size distribution (Figure 6-1, d). The lattice fringe had *d*-spacing attributed to d-spacing Au {111} (Figure 6-1, e). These results revealed that glutathione allowed the size-selective synthesis of small Au nanoparticles on HAP and that the size of Au nanoparticles could be controlled by the Au loading amounts. The absence of glutathione in Au/HAP-NC was confirmed by elemental analysis.
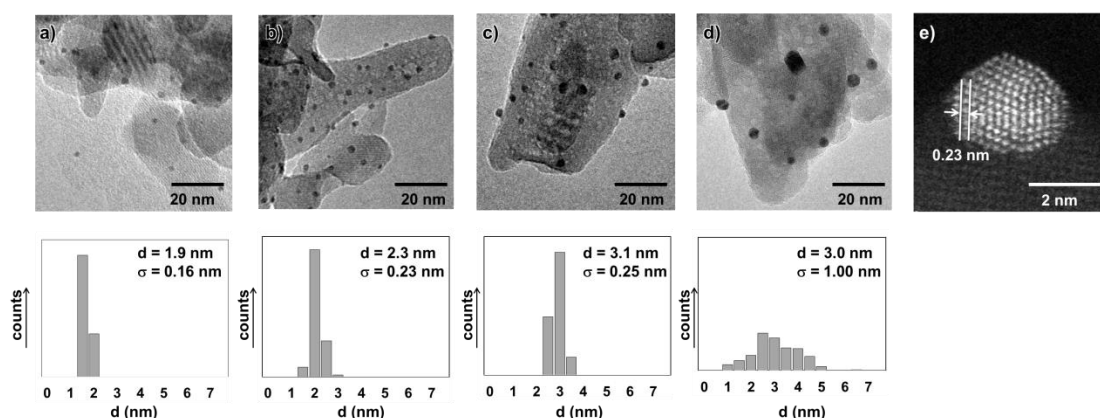

Figure 6-1. TEM images and corresponding histograms for a) Au/HAP-NC (0.5 wt%); b) Au/HAP-NC (2 wt%); c) Au/HAP-NC (3 wt%); d) Au/HAP. e) ADF-STEM image of Au/HAP-NC (0.5 wt%)

With the prepared Au/HAP-NC catalysts in hands, the hydrolytic oxidation of dimethylphenylsilane (**1**) as a model substrate was conducted in DME at ambient temperature in air (Table 6-1). Notably, Au/HAP-NC (0.5 wt%) efficiently promoted the oxidation, affording dimethylphenylsilanol (**2**) in 99% yield along with the generation of equimolar amounts of H_2 after 9 min (Entry 2). The catalytic activity of Au/HAP-NC increased as the size of the Au nanoparticles decreased (Entries 1, 4, and 5). The catalytic activity of Au/HAP-NC (0.5 wt%) was much greater than that of previously reported Au/HAP prepared by the deposition–precipitation method (Entry 6). Neither bulk Au (non-nanosized Au) nor HAP show any activity (Entries 7 and 8), indicating that the Au nanoparticles were the active species. In addition, Au/HAP-NC (0.5 wt%) worked well at

scale-up conditions with a lower catalyst loading (0.03 mmol%), giving a turnover number of 3,333,000 and turnover frequency of 77/sec (Scheme 6-1), both of which were much greater than values previously reported (Table 6-2) [33-43]. Furthermore, Au/HAP-NC (0.5 wt%) was reusable without any loss of its activity and selectivity (Entry 2 vs. 3). The TEM image of the used Au/HAP-NC (0.5 wt%) catalyst showed that the average diameter and size distribution of the Au nanoparticles were similar to those of Au/HAP-NC (0.5 wt%) before use and that no aggregation of Au nanoparticles occurred (Figure 6-2), proving high durability of Au/HAP-NC (0.5 wt%) against aggregation.

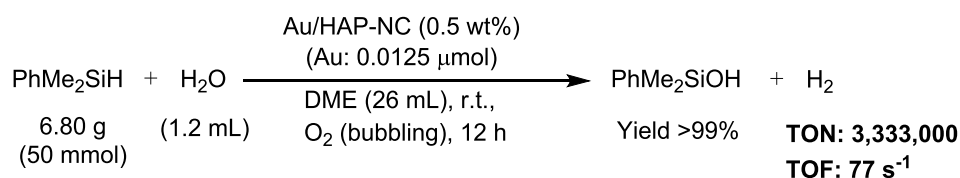**Table 6-1**. Aqueous oxidation of **1** using Au catalysts[a]

$$PhMe_2SiH + H_2O \xrightarrow[\text{air, r.t.}]{\text{Au catalyst}} PhMe_2SiOH + H_2$$

1 → **2**

Entry	Catalyst	d [nm]	Time [min]	Yield [%][b]
1	Au/HAP-NC (0.5 wt%)	1.9	5	83
2	Au/HAP-NC (0.5 wt%)	1.9	9	>99
3[c]	Au/HAP-NC (0.5 wt%)	1.9	9	>99
4	Au/HAP-NC (2 wt%)	2.3	5	49
5	Au/HAP-NC (3 wt%)	3.1	5	39
6	Au/HAP	3.0	5	33
7	Au bulk	-	5	trace
8	HAP	-	5	0

[a]Reaction conditions: **1** (1 mmol), Au catalyst (0.05 mol%), water (0.2 mL), DME (1 mL). [b]Determined by GC using internal standard technique. [c]Reuse.

Table 6-2. Comparison with previously reported catalysts

Catalyst	TON	TOF (sec^{-1})	Reference (Ref. X)
Au/HAP-NC (0.5 wt%)	3,333,000	77	This work
Au/HAP	1,230,000	49	author's previous work (24, Chapter V)
Pd/Al$_2$O$_3$	20,000	28	J. Park *et al. ChemCatChem* (38)
Pd/C	20,000	28	K. Shimizu *et al. Chem. Eur. J.* (37)
AuCNT nanohybrid	12,000	20	E. Doris *et al. Angew. Chem. Int. Ed.* (36)
Au$_{34}$Ag$_{28}$(PA)$_{34}$/Carbon	-	9 (32)[a]	N. Zheng *et al. J. Am. Chem. Soc.* (42)
Au/SiO$_2$	250	5[a]	T. Zhang et al. *Chem. Commun.* (40)
TBA$_8$[Ag$_4$(γ-H$_2$SiW$_{16}$O$_{32}$)$_2$]	27,000	4	N. Mizuno *et al. Angew. Chem. Int. Ed.* (41)

[a]Caliculated based on surface metal atoms.

$$\text{PhMe}_2\text{SiH} + \text{H}_2\text{O} \xrightarrow[\substack{\text{DME (26 mL), r.t.,}\\\text{O}_2\text{ (bubbling), 12 h}}]{\substack{\text{Au/HAP-NC (0.5 wt\%)}\\\text{(Au: 0.0125 }\mu\text{mol)}}} \text{PhMe}_2\text{SiOH} + \text{H}_2$$

6.80 g   (1.2 mL)   Yield >99%   **TON: 3,333,000**
(50 mmol)   **TOF: 77 s^{-1}**

Scheme 6-1. Scale-up oxidation of **1** using Au/HAP-NC (0.5 wt%)
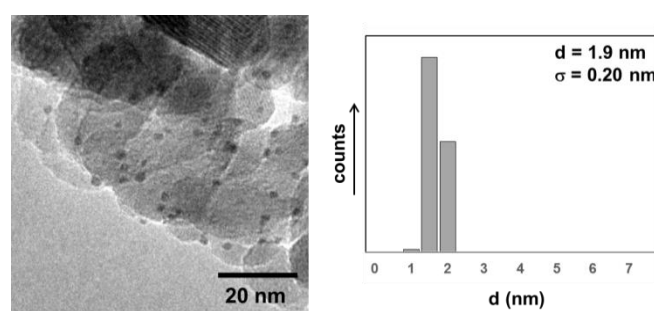
Figure 6-2. TEM image and size-distribution of the used Au/HAP-NC (0.5 wt%)

Next, the catalytic activity of Au/HAP-NC (0.5 wt%) for H_2-production through the hydrolytic oxidation of PMHS and TMDS was investigated (Figure 6-3). Upon addition of Au/HAP-NC (0.5 wt%) to the DME/water solution of PMHS or TMDS at ambient temperature in air, H_2 gas was efficiently generated with initial production rates of 9.8 and 18.9 mL/min, respectively. When Au/HAP-NC (0.5 wt%) was separated from the reaction mixture by filtration, the H_2 generation quickly stopped; re-addition of Au/HAP-NC (0.5 wt%) to the filtrate induced re-generation of H_2. This is the first report of an on/off-switchable H_2-production system using the hydrolytic oxidation of inexpensive organosilanes without the need for any additional energy input. The catalytic system of the on/off-switching of H_2-production was demonstrated in Figure 6-4; the generation and suppression of the H_2 bubble in response to the introduction and removal of Au/HAP-NC (0.5 wt%) could be observed. This on/off-switchable H_2-production system could be

applied to a portable hydrogen fuel cell. When the catalyst system (hydrogen generation part) was connected to the power generation part, including a Pt anode, electric power was generated that could be turned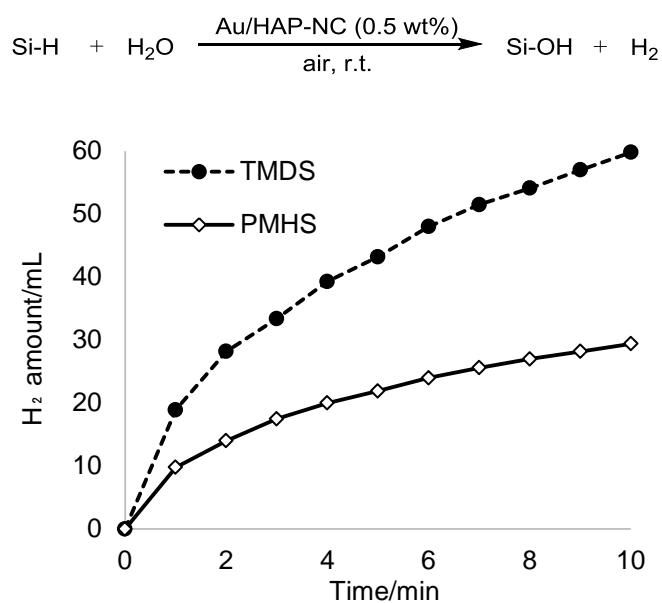 on and off at ambient temperature in air atmosphere (See http://www.nature.com/articles/srep37682, Supplementary Movie 2).

$$Si\text{-}H \ + \ H_2O \ \xrightarrow[\text{air, r.t.}]{\text{Au/HAP-NC (0.5 wt\%)}} \ Si\text{-}OH \ + \ H_2$$

Figure 6-3. Evolution of H_2 from TMDS or PMHS using Au/HAP-NC (0.5 wt%). Reaction conditions: Au/HAP-NC (0.5 wt%) (1.0 g, Au: 0.025 mmol), Si-H (10 mmol), DME (5 mL), water (0.6 mL), air.
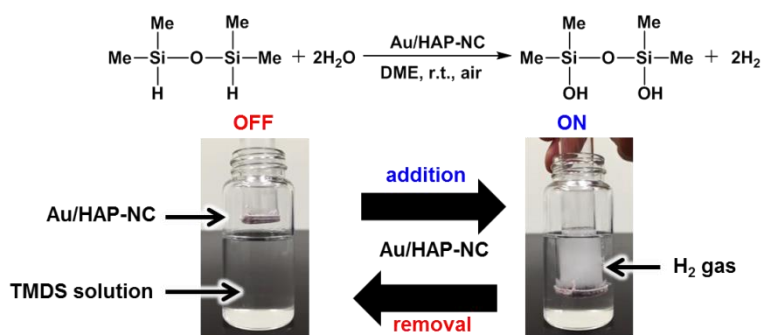
Figure 6-4. On-off switching of H_2 generation

4. Conclusion

This chapter demonstrated the development of highly efficient H_2-production system through a size-controllable synthesis of Au nanoparticles on HAP with very narrow size distribution. The Au/HAP-NC (0.5 wt%) catalyst with a mean diameter of 1.9 nm exhibited the great catalytic activity for hydrogen production through the hydrolytic oxidation of hydrosilanes. The high catalytic activity of Au/HAP-NC (0.5 wt%) was applied to H_2-production from inexpensive PMHS and TMDS as hydrogen storage materials at ambient temperature in air. The heterogeneous Au/HAP-NC (0.5 wt%) catalyst could be separated, enabling the on/off-switching of H_2-production by the introduction and removal of the catalyst. This catalytic system for on/off switchable H_2-production from organosilanes can contribute to the development of next-generation green sustainable hydrogen fuel cells with on-demand H_2-production

5. References

[1] N. Eigen, C. Kekker, M. Dornheim, T. Klassen, R. Bormann, *Scripta Materialia* **2007**, *56*, 847-851.

[2] H. Z. Wang, D. Y. C. Leung, M. K. H. Leung, M. A. Ni, *Renew. Sust. Energ. Rev.* **2009**, *13*, 845-853.

[3] X. Huang, T. Gao, X. Pan, D. Wei, C. Lv, L. Qin, Y. Huang, *J. Power Sources* **2013**, *229*, 133-140.

[4] B. Peng, J. Chen, *Energy Environ. Sci.* **2008**, *1*, 479-483.

[5] S. D. Rassat, C. L. Aardahl, T. Autrey, R. S. Smith, *Energy Fuels* **2010**, *24*, 2596-2606.

[6] A. Staubitz, A. P. M. Robertson, I. Manners, *Chem. Rev.* **2010**, *110*, 4079-4124.

[7] F. Joó, *ChemSusChem* **2008**, *1*, 805-808.

[8] A. K. Singh, S. Singh, A. Kumar, *Catal. Sci. Technol.* **2016**, *6*, 12-40.

[9] R. S. Coffey, *Chem. Commun. (London)* **1967**, 923-924.

[10] R. Williams, R. S. Crandall, A. Bloom, *Appl. Phys. Lett.* **1978**, *33*, 381.

[11] B. Loges, A. Boddien, H. Junge, M. Beller, *Angew. Chem. Int. Ed.* **2008**, *47*, 3962-3965.

[12] C. Fellay, P. J. Dyson, G. Laurenczy, *Angew. Chem. Int. Ed.* **2008**, *47, 3966-3968.

[13] K. Tedsress, T. Li, S. Jones, C. W. A. Chan, K. M. K. Yu, P. A. J. Bagot, E. A. Marquis, G. D. W. Smith, S. C. E. Tsang, *Nat. Nanotechnol.* **2011**, *6*, 302-307.

[14] K. Mori, H. Tanaka, M. Dojo, K. Yoshizawa, H. Yamashita, *Chem. Eur. J.* **2015**, *21*, 12085-12092.

[15] M. Chandra, Q. Xu, *J. Power Sources* **2006**, *156*, 190-194.

[16] J.-M. Yan, X.-B. Zhang, S. Han, H. Shinoyama, Q. Xu, *Angew. Chem. Int. Ed.* **2008**, *47*, 2287-2289.

[17] H.-L. Jiang, Q. Xu, *Catal. Today* **2011**, *170*, 56-63.

[18] U. Sanyal, U. B. Demirci, B. R. Jagirdar, P. Miele, *ChemSusChem* **2011**, *4*, 1731-1739.

[19] A. Aijaz, A. Karkamkar, Y. J. Choi, N. Tsumori, E. Rönnebro, T. Autrey, H. Shioyama, Q. Xu, *J. Am. Chem. Soc.* **2012**, *134*, 13926-13929.

[20] Z.-H. Lu, J. Li, A. Zhu, Q. Yao, W. Huang, R. Zhou, R. Zhou, X. Chen, *Int. J. Hydrog. Energy* **2013**, *38*, 5330-5337.

[21] Z.-H. Lu, Q. Yao, Z. Zhang, Y. Yang, X. Chen, *J. Nanomater.* **2014**, Article ID: 729029.

[22] H. Cheng, T. Kamegawa, K. Mori, H. Yamashita, *Angew. Chem. Int. Ed.* **2014**, *53*, 2910-2914.

[23] A. Nozaki, S. Kittima, Y. Tanibara, Y. Kuwahara, T. Ohmichi, T. Kamegawa, K. Mori, H. Yamashita, *Mater. Trans.* **2015**, *56*, 485-489.

[24] T. Urayama, T. Mitsudome, Z. Maeno, T. Mizugaki, K. Jitsukawa, K. Kaneda, *Chem. Lett.* **2015**, *44*, 1062-1064.

[25] N. J. Lawrence, M. D. Drew, M. Bushell, *J. Chem. Soc., Perkin Trans. 1*, **1991**, 3381-3391.

[26] E. Feghali, O. Jacquet, P. Thuéry, T. Cantat, *Catal. Sci. Technol.* **2014**, *4*, 2230-2234.

[27] M. Takahashi, Y. Yakeuchi (Shinetsu Chemical Co.), JPH08157726 (A), **1996**.

[28] T. Matsuda, T. Sakamoto, S. Sato, N. Koike, Y. Tarumi, T. Kimura, Y. Yamamoto, M. Arai (Shinetsu Chemical Co.), EP0745604, **1996**.

[29] T. Mitsudome, A. Noujima, T. Mizugaki, K. Jitsukawa, K. Kaneda, *Chem. Commun.* **2009**, 5302-5304.

[30] T. G. Schaaff, G. Knight, M. N. Shafigullin, R. F. Borkman, R. L. Whetten, *J. Phys. Chem. B* **1998**, *102*, 10643-10646.

[31] T. G. Schaaff, R. L. Whetten, *J. Phys. Chem. B* **2000**, *104*, 2630-2641.

[32] N. Negishi, K. Nobusada, T. Tsukuda, *J. Am. Chem. Soc.* **2005**, *127*, 5261-5270.

[33] K. Mori, M. Tano, T. Mizugaki, K. Ebitani, K. Kaneda, *New J. Chem.* **2002**, *26*, 1536-1538.

[34] E. Choi, C. Lee, Y. Na, S. Chang, *Org. Lett.* **2002**, *4*, 2369-2371.

[35] N. Asao, Y. Ishikawa, N. Hatakeyama, Menggenbateer, Y. Yamamoto, M. Chen, W. Zhang, A. Inoue, *Angew. Chem. Int. Ed.* **2010**, *49*, 10093-10095.

[36] J. John, E. Gravel, A. Hagège, H. Li, T. Gacoin, E. Doris, *Angew. Chem. Int. Ed.* **2011**, *50*, 7533-7536.

[37] K. Shimizu, T. Kubo, A. Satsuma, *Chem. Eur. J.* **2012**, *18*, 2226-2229.

[38] M. Jeon, J. Han, J. Park, *ChemCatChem*, **2012**, *4*, 521-524.

[39] Y. Kikukawa, Y. Kuroda, K. Yamaguchi, N. Mizuno, *Angew. Chem. Int. Ed.* **2012**, *51*, 2434-2437.

[40] W. Li, A. Wang, X. Yang, Y. Huang, T. Zhang, *Chem. Commun.* **2012**, *48*, 9183-9185.

[41] F. Mitschang, H. Schmalz, S. Agarwal, A. Greiner, *Angew. Chem. Int. Ed.* **2014**, *53*, 4972-4975.

[42] Y. Wang, X.-K. Wan, L. Ren, H. Su, G. Li, S. Maloa, S. Lin, Z. Tang, H. Hakkien, B. K. Teo, Q.-M. Wang, N. Zheng, *J. Am. Chem. Soc.* **2016**, *138*, 3278-3281.

[43] T. Mitsudome, S. Arita, H. Mori, T. Mizugaki, K. Jitsukawa, K. Kaneda, *Angew. Chem. Int. Ed.* **2008**, *47,* 7938-7940.

General Conclusions

This thesis deals with studies on the design and precise synthesis of supported metal nanoparticle catalysts for efficient hydrogenation and dehydrogenation reactions. This study discloses that the construction of core-shell nanocomposites, size-selective synthesis of metal nanoparticles and selection of suitable catalytic supports made metal nanoparticles possible to exhibit unprecedentedly unique catalysis for the target reactions.

In Chapter I, recent reports of metal nanoparticle catalysts under liquid-phase conditions for efficient fine chemical syntheses were reviewed. The four types of modification strategies for supported metal nanoparticle catalysts, that is, 1) electronic interaction with their support materials, 2) concerted effect with their support materials, 3) control of their morphology, 4) addition of other metals to form bimetal catalysts were also highlighted.

The author described in Chapter II the development of core-Pd/shell-Ag nanocomposite catalyst (Pd@Ag) for selective semihydrogenation of terminal and internal alkynes to the corresponding alkenes with high Z-selectivity. This unique catalysis of Pd@Ag derives from the cooperative action between core-Pd and shell-Ag. It is well known that Pd catalysts show high activity for the hydrogenation of alkynes, but promote the overhydrogenation of alkenes to alkanes. In contrast, Ag catalysts exhibit high alkene-selectivity while hydrogenation ability is very low. In this Pd@Ag catalyst, the inner Pd nanoparticles can act as the hydrogen supplier to the outer Ag layer, assisting the selective semihydrogenation of alkynes on the Ag surface. At the same time, the Ag shell can efficiently suppress the exposure of Pd nanoparticles, inhibiting the overhydrogenation of alkenes to alkanes. This complementary action of Pd and Ag can realize selective

semihydrogenation of alkynes under mild conditions.

In Chapter III, the author mentioned the development of a green route for the synthesis of core-shell nanoparticles in one-step under organic-free and pH-neutral condition. Simply mixing core and shell metal precursors in the presence of solid bases in water allowed for the facile fabrication of small CeO_2-covered Au and Ag nanoparticles in one-step. This is the first achievement of one-step syntheses of small core-shell nanoparticles without the use of surfactants, organic solvents, reductants, or toxic bases. Additionally, the synthesized CeO_2-covered Au nanoparticles acted as a highly efficient and reusable catalyst for chemoselective reduction reactions of epoxides, unsaturated aldehydes and alkynes while retaining C=C bonds. In this catalytic system, the high chemoselectivity was obtained from the cooperative action at the interface between core-Au and shell-CeO_2.

The next chapter represented the efficient dehydrogenative coupling of hydrosilanes with amines or amides using hydrpxyapatite-supported Au nanoparticle catalyst (Au/HAP). A wide range of silylamines and silylamides can be obtained in good to excellent yields, demonstrating the first example of an efficient heterogeneous catalyst for the synthesis of silylamides. Furthermore, the Au/HAP showed the practical applicability for the gram-scale synthesis of silylamines, where the turnover number reached 5180. This value is the best among reported catalysts. Moreover, Au/HAP was also recoverable by a simple filtration and reusable without any loss of its catalytic efficiency.

In Chapters V and VI, the author demonstrated acceralation effect of molecular oxygenson the aqueous oxidation of hydrosilanes to silanols catalyzed by Au nanoparticles. In this catalytic system, O_2 acted as a non-consumed activator for Au nanoparticles in the oxidation of hydrosilanes,

providing an acceleration effect of 200 times the reaction rate relative to Ar atmosphere. Furthermore, the author improved the catalytic activity through size-selective synthesis of Au nanoparticles, resulting in a turnover number of 3,333,000 and turnover frequency of 77/sec, both of which were much greater than values previously reported. Moreover, the improved Au catalyst was applied to the environmental-friendly H_2-generation system using inexpensive PMHS and TMDS as hydrogen storage materials without requiring additional energy. Additionally, taking advantages of easy separation of Au/HAP catalyst from reaction mixtures, the developed system enabled the on/off-switching of H_2-production by the introduction and removal of the catalyst.

In this thesis, the author described the rational and precise synthesis of metal nanoparticle catalysts. The developed nanomaterials acted as highly efficient heterogeneous catalysts for the hydrogenation and dehydrogenation reactions under mild reaction conditions. In addition to the advantages of conventional heterogeneous catalysts, they showed unique activity and selectivity for the target reactions. The author hopes that the methodology of the developed catalyst design makes a great contribution to green organic transformations.

Finally, further extension of unique catalysis based on the cooperative actions of precious metal nanoparticles and metal oxides for hydrogenation reactions was addressed as follows.

CO_2 reduction is one of the main themes of environmental conservation actions. In the field of fine chemical synthesis, the efficient utilization of CO_2 as a carbon source has attracted much attentions due to their abundance and cost-effectiveness. In this context, the synthesis of formamide derivates which are widely used as solvents, antioxidants in the rubber chemistry and intermediates in the pharmaceutical industry is the promising target. Synthesis of formamides using CO_2, that is,

formylation of amines using H_2 and CO_2 proceeds through the hydrogenation of CO_2 to the formic acid intermediates and the nucleophilic attack of amines on the intermediates to form formamides.

It is well known that oxygen defect sites of reducible oxides created at the interface between metal nanoparticles and metal oxides efficiently activate C=O bond of CO_2. Thus, the combination of metal nanoparticles and reducible oxides could be effective for this reaction. Additionally, as shown in Chapter III, Au nanoparticles can promote chemoselective hydrogenations through the efficient construction of interface sites. Therefore, it can be expected that reducible oxide-supported Au nanoparticles or Au-core/reducible oxide-shell nanoparticles would promote selective formylation of amines while retaining reducible functional groups such as alkenes, aldehydes and nitriles. This selective formylation of amine using CO_2 is a challenging task due to the thermodynamic stability of CO_2. Therefore, this proposed catalytic system will be a powerful tool for the efficient utilization of carbon dioxides as C1 reagents.

List of Publications

[1] Takato Mitsudome, <u>Teppei Urayama</u>, Zen Maeno, Tomoo Mizugaki, Koichiro Jitsukawa, Kiyotomi Kaneda

"Highly Efficient Dehydrogenative Coupling of Hydrosilanes with Amines or Amides Using Supported Gold Nanoparticles"

Chemistry -A European Journal **2015**, *21*, 3202-3205.

[2] <u>Teppei Urayama</u>, Takato Mitsudome, Zen Maeno, Tomoo Mizugaki, Koichiro Jitsukawa, Kiyotomi Kaneda

"O_2-enhanced Catalytic Activity of Gold Nanoparticles in Selective Oxidation of Hydrosilanes to Silanols"

Chemistry Letters **2015**, *44*, 1062-1064.

[3] Takato Mitsudome, <u>Teppei Urayama</u>, Kenji Yamazaki, Yosuke Maehara, Jun Yamasaki, Kazutoshi Gohara, Zen Maeno, Tomoo Mizugaki, Koichiro Jitsukawa, Kiyotomi Kaneda

"Design of Core-Pd/Shell-Ag Nanocomposite Catalyst for Selective Semihydrogenation of Alkynes"

ACS Catalysis **2016**, *6*, 666-670.

[4] <u>Teppei Urayama</u>, Takato Mitsudome, Zen Maeno, Tomoo Mizugaki, Koichiro Jitsukawa, Kiyotomi Kaneda

"Green, Multi-Gram One-Step Synthesis of Core–Shell Nanocomposites in Water and Their Catalytic Application to Chemoselective Hydrogenations"

Chemistry -A European Journal **2016**, *22*, 17962-17966.

[5] Takato Mitsudome, <u>Teppei Urayama</u>, Taizo Kiyohiro, Zen Maeno, Tomoo Mizugaki, Koichiro Jitsukawa, Kiyotomi Kaneda

"On-demand Hydrogen Production from Organosilanes at Ambient Temperature Using Heterogeneous Gold Catalysts"

Scientific Reports **2016**, *6*, Article Number: 37682.

International Meeting (Oral Presentation)

[1] <u>Teppei Urayama</u>, Takato Mitsudome, Zen Maeno, Tomoo Mizugaki, Koichiro Jitsukawa, Kiyotomi Kaneda

"Design of Core-Pd/Shell-Ag Nanocomposite Catalyst for Selective Semihydrogenation of Alkynes to Alkenes"

August, 2016, ACS 252nd National Meeting, Philadelphia (USA).

Acknowledgement